MATERIAL CHARACTERIZATION STUDIES

FOR

CARBURIZED QUENCHING PROCESS DESIGN

AND QUALITY ASSESSMENT

A MASTER'S THESIS

in

Metallurgical and Material Engineering

Atılım University

by

SEÇİL YILDIZ

OCTOBER 2017

MATERIAL CHARACTERIZATION STUDIES

FOR

CARBURIZED QUENCHING PROCESS DESIGN

AND QUALITY ASSESSMENT

A THESIS SUBMITTED TO

THE GRADUATE SCHOOL OF NATURAL AND APPLIED SCIENCES

OF

ATILIM UNIVERSITY

BY

SEÇİL YILDIZ

IN PARTIAL FULFILLMENT OF THE REQUIREMENTS FOR THE DEGREE OF

MASTER OF SCIENCE

IN

METALLURGICAL AND MATERIALS ENGINEERING

OCTOBER 2017

Approval of the Graduate School of Natural and Applied Sciences, Atılım University.

_____

Pof. Dr. Ali Kara

Director

I certify that this thesis satisfies all the requirements as a thesis for the degree of Master of Science.

_____

Prof. Dr. Naci Sevinç

Head of Department

This is to certify that we have read the thesis "MATERIAL CHARACTERIZATION STUDIES FOR CARBURIZED QUENCHING PROCESS DESIGN AND QUALITY ASSESSMENT" submitted by "Seçil YILDIZ" and that in our opinion it is fully adequate, in scope and quality, as a thesis for the degree of Master of Science.

_____	_____
Asst. Prof. Dr. Caner Şimşir	Asst. Prof. Dr.-Ing. Kemal Davut
Co-Supervisor	Supervisor

Examining Committee Members

Prof. Dr. Naci Sevinç	_____
Asst. Prof. Dr.-Ing. Kemal Davut	_____
Asst. Prof. Dr. Omer Music	_____

Date: 13.10.2017

I declare and guarantee that all data, knowledge and information in this document has been obtained, processed and presented in accordance with academic rules and ethical conduct. Based on these rules and conduct, I have fully cited and referenced all material and results that are not original to this work.

Seçil YILDIZ

ABSTRACT

MATERIAL CHARACTERIZATION STUDIES FOR CARBURIZED QUENCHING PROCESS DESIGN AND QUALITY ASSESSMENT

Yıldız, Seçil

M.S., Metallurgical and Materials Engineering Department

Supervisor: Asst. Prof Dr.-Ing. Kemal Davut

Co-Supervisor: Asst. Prof Dr. Caner Şimşir

October 2017, 113 pages

Carburized quenching is a surface hardening process applied to low and medium carbon steel parts to improve fatigue and wear resistance. Distortion, cracking, inadequate case depth and surface/core hardness are the most frequently encountered problems during this process. During the last two decades, computer simulations became popular to predict and avoid those problems instead of conventional analytical and trial-and-error approaches. Aside from troubleshooting, heat treatment simulations enable determination of optimal process parameters yielding the desired microstructure and residual stress distribution to improve the performance of the part.

Primary aim of this study is to complement computational materials engineering methods to develop a material data set for the carburized quenching simulation of DIN 22NiCrMo2-2 (SAE 8620H) steel. For that purpose, first, the raw material is characterized chemically and microstructurally to provide necessary input to computational techniques. Then, the kinetics of austenite growth, which has strong impact on phase transformations during succeeding quenching step, is investigated. Finally, critical temperatures and transformation kinetics are determined and presented in the form of TTT and CCT diagrams.

Raw material characterization results indicate that the billets are qualified for the process and the validation study as the billets are free of macro-segregation and exhibit a homogeneous and mildly banded equiaxed ferritic/pearlitic grain structure. Moreover, austenite grain growth study revealed that the grain growth in 22NiCrMo2-2 can be expressed by an ideal grain growth law. Finally, computationally and experimentally determined CCT diagrams are in a good agreement. The largest differences between computationally and experimentally determined TTT diagrams are observed in the bainitic transformation range which is more sensitive to hard to control factors such as local chemical composition and local prior austenite grain size.

Secondary aim of this study is to conduct microstructural investigations for the quality assessment and validation of computer simulations conducted in complementary studies within the scope of the same project. In one of those complementary studies, an experimental Design of Experiments (DoE) using the Taguchi method is conducted on steel shafts made of DIN 22NiCrMo2-2 and 16MnCr5 steels to minimize the variability of the industrial process. In the other study, the same DoE is investigated using computer simulations. This thesis complements those studies with determination of microstructure and hardness distributions. The experimental results indicate an agreement with the simulations results and the agreement can be improved with better characterization of bainite transformation kinetics including its dependence on stress, local grain size and chemical composition.

Keywords: Carburizing, Case Depth, Phase transformation, Austenite Grain Growth, CCT, TTT

ÖZ

SEMENTASYON VE TAKİP EDEN SU-VERME İŞLEMLERİNİN SÜREÇ TASARIMI VE KALİTE DEĞERLENDİRMESİNE YÖNELİK MALZEME KARAKTERİZASYON ÇALIŞMALARI

Yıldız, Seçil

Yüksek Lisans, Metalurji ve Malzeme Mühendisliği

Tez Yöneticisi: Yrd. Doç. Dr.-Ing. Kemal Davut

Ortak Tez Yöneticisi: Yrd. Doç. Dr. Caner Şimşir

Ekim 2017, 113 sayfa

Sementasyon ve su-verme ısıl işlemi; aşınma ve yorulma dayancı özelliklerini iyileştirmek için düşük karbonlu çelik parçalara uygulanan bir yüzey sertleştirme işlemidir. Çarpılma, çatlak, sertlik veya sertlik derinliğinde yetersizlik bu işleme bağlı olarak en sık karşılaşılan sorunlardır. Son yirmi yılda, bu sorunları tahmin etmek ve engellemek için, analitik ve deneme-yanılma gibi geleneksel yöntemler yerine bilgisayar simülasyonları daha popüler hale gelmiştir. Bilgisayar destekli ısıl işlem simülasyonları sorunları çözmenin dışında istenilen mikroyapı ve kalıntı gerilme dağılımını sağlayan en uygun proses parametrelerinin belirlenmesini ve bu sayede parça performansının artırılmasını sağlamaktadır.

Bu çalışmanın birinci amacı, DIN 22NiCrMo2-2 (SAE 8620H) çeliğine uygulanan sementasyon ve su-verme işlemlerinin simülasyonu için gerekli malzeme veri setinin geliştirilerek hesaplamalı malzeme mühendisliği yöntemlerini tamamlamaktır. Bu amaçla öncelikle, hesaplama tekniklerine gerekli girdiyi sağlamak için, kimyasal ve mikroyapısal olarak ham malzeme karakterizasyonu yapılmıştır. Ardından, su-verme aşamasında faz dönüşümleri üzerinde önemli derecede etkisi olan östenit büyüme

kinetiği araştırılmıştır. Son olarak, kritik sıcaklıklar ve dönüşüm kinetiği belirlenerek, TTT ve CCT diyagramları şeklinde sunulmuştur.

Ham malzeme karakterizasyon çalışmalarıyla kütüklerin makro segregasyon içermediği, eşeksenli ferritik/perlitik bantlaşmış ve homojen dağılımlı tane yapısına sahip olduğu ve bu nedenlerle proses ve doğrulama çalışmaları için uygun olduğu tespit edilmiştir. Ayrıca, deneysel ve hesaplamalı yöntemlerle belirlenen CCT diyagramlarının birbirleriyle uyumlu olduğu görülmektedir. Deneysel ve hesaplamalı yöntemlerle belirlenen TTT diyagramları arasındaki en büyük farklılık, yerel kimyasal kompozisyon ve yerel östenit tanesi boyutu gibi kontrol edilmesi zor olan faktörlere karşı daha hassas olan beynitik faz dönüşümünde gözlenmektedir.

Bu çalışmanın ikinci amacı, aynı proje kapsamında yürütülen tamamlayıcı bilgisayar simülasyonları çalışmalarının geçerliliğinin belirlenmesi ve sementasyon ısıl işleminin kalite değerlendirmesi için içyapı incelemeleri yapmaktır. Bahsi geçen tamamlayıcı çalışmaların birinde, endüstriyel prosesteki değişkenliği en aza indirgemek için DIN 22NiCrMo2-2 ve DIN 16MnCr5 çeliklerinden imal edilen miller üzerinde Taguchi metodu kullanılarak Deney Tasarımı (DoE) yapılarak endüstriyel koşullarda sementasyon deneyleri yapılmıştır. Diğer tamamlayıcı çalışmada ise, aynı Deney Tasarımı (DoE) bilgisayar simülasyonu çalışmalarıyla incelenmiştir. Bu tez çalışmasında ise, içyapı ve sertlik dağılımlarının belirlenmesiyle belirtilen diğer çalışmalar tamamlanmaktadır. Elde edilen sonuçlar bilgisayar simülasyonları ve deneysel sonuçların birbirine uyumlu olduğunu göstermektedir. Sonuçların uyumu beynit dönüşüm kinetiğinin gerilim, yerel tane boyutu ve yerel kimyasal kompozisyona bağlılığını da dahil eden daha iyi karakterizasyon çalışmalarıyla iyileştirilebilir.

Anahtar Kelimeler: Sementasyon, Sertlik Derinliği, Faz Dönüşümü, Östenit Tane Büyümesi, CCT, TTT

To my Family…

ACKNOWLEDGMENTS

First of all, I would like to express my deep appreciation and sincere to my supervisor Assist. Prof. Dr.-Ing. Kemal Davut for his support, knowledge, patience and counseling throughout the research. I also would like to express my sincere appreciation to co-supervisor Assist. Prof. Dr. Caner Şimşir for his encouragement, help, patience and support during research. This thesis would not be possible without their guidance, help and support.

This work has been funded bilaterally by Turkish Ministry of Science, Technology and Industry and ESTAS Camshaft & Chilled Cast through SANTEZ Program as a part of Project No. 0673.STZ.2014-01. I would like to gratitude to them for the financial support.

I would like to express my appreciation and thanks to Prof. Dr. Naci Sevinç, Assist. Prof. Dr. Omer Music for their contributions.

I want to extend my thanks to Zeynep Öztürk, Elif Evcil, Rasim Köksal Ertan, Yasin Demirkol, Yahya Tunç, Hava Hüyük, Hasan Yılmaz and Ozan Müştak for their help in experimental studies.

I would also like to thank Büşra Yazır for her significant support, help, knowledge and friendship.

I would like to thank my dear friends, Merve Köroğlu, Atike Büşra Köprülü, Gülşah Demir, Tuğçe Hacaloğlu and Ebru Arslan for their friendship, understanding and support.

Finally, I would like to my endless gratitude to my family, my mother Aysun Yıldız, my father Taner Yıldız and my sister Seda Yıldız Sırakaya for their limitless support, patience and trust.

TABLE OF CONTENTS

ABSTRACT v

ÖZ vii

ACKNOWLEDGMENTS x

TABLE OF CONTENTS xi

LIST OF TABLES xv

LIST OF FIGURES xvii

LIST OF ABBREVIATIONS AND SYMBOLS xxiv

CHAPTER 1 1

INTRODUCTION 1

1.1. Aim And Motivation of Study 3

CHAPTER 2 6

THEORY AND LITERATURE SURVEY 6

2.1. Theory of Carburizing 6

2.2. Carburizing Methods 7

2.2.1. Pack Carburizing 7

2.2.2. Liquid Carburizing 8

2.2.3. Gas Carburizing 8

2.2.3.1. Process Parameter of Gas Carburizing 8

2.2.4. Steel Grades For Carburizing 9

2.2.5. Advantage and Disadvantages in Comparison to Other Case Hardening Methods 10
2.3. Theory of Grain Growth 11
2.4. Theory of Phase Transformation 14
2.4.1. Factor Affecting Phase Transformation 15
2.4.1.1. Nucleation 15
2.4.1.2. Growth 16
2.4.1.3. Diffusion 16
2.4.2. Kinetics of Solid State Phase Transformation 18
2.4.2.1. Diffusional Phase Transformation 18
2.4.2.2. Displacive Phase Transformation 20
2.4.3. Parameters Affecting CCT And TTT Diagram 21
2.5. Parameters Affecting The Hardness and Case Depth 23
CHAPTER 3 27
CHARACTERIZATION OF RAW MATERIAL 27
3.1. Macro Chemical Analysis 27
3.2. Macro Segregation Analysis 27
3.3. Microstructural Characterization 29
3.3.1. Determination of Ferrite and Pearlite Percentage and Grain Size 31
3.3.2. Degree of Banding 35
3.3.3. Micro Segregation Analysis 38
3.4. DIN 22NiCrMo2-2 (SAE 8620H) Equilibrium Phase Diagram 41
3.5. Discussions 42
CHAPTER 4 45
DETERMINATION OF AUSTENITE GRAIN GROWTH KINETICS 45
4.1. Introduction 45

4.2. Experimental Procedure 46
4.3. Results of Grain Growth Kinetic Analysis 47
4.4. Discussions 53
CHAPTER 5 55
DETERMINATION OF PHASE TRANSFORMATION KINETICS 55
5.1. Introduction 55
5.2. Experimental Determination of CCT 56
5.3. Experimental Determination of Critical Temperatures (M_s, M_f, B_s, A_{c1} and A_{c3}) 65
5.4. Determination of Isothermal Diagram (TTT) From Inverse Analysis of CCT 70
5.5. Discussions 72
CHAPTER 6 75
CHARACTERIZATION STUDIES ON GAS CARBURIZED SHAFTS 75
6.1. Introduction 75
6.2. Test Procedure and Materials 76
6.3. Hardness, Carbon and Microstructure Analysis Results and Discussions 79
6.4. Case Depth Results 89
6.5. Comparison of Simulation and Experimental Results and Discussions 90
CHAPTER 7 95
CONCLUSION 95
REFERENCES 98
APPENDICES 105
A. Raw Material Characterization Results 105

B. Microstructure Results of Carburized Shafts..... 108

LIST OF TABLES

Table 1. Summary of required material properties for application to heat treatment simulations (plus sign indicates required parameters) [7] 5

Table 2. Chemical compositions of selected steels for carburizing [17] 10

Table 3. Relative benefits of five common surface-hardening processes [13] 11

Table 4. Chemical composition of DIN 22NiCrMo2-2 steel used in this study 27

Table 5. Calculations and definitions of aspect ratio, circularity, angle and grain size 33

Table 6. The mean values of the analyzes made for each of the 3 sections for the head, middle, end of the billet 33

Table 7. Parameters and formulas used to determine the banding degree 36

Table 8. Prior-austenite grain size etchants..... 47

Table 9. The comparison chemical composition (wt. %) of this study and E.Khzouz's study 49

Table 10. Average grain size values (AGS) and the standard deviation of AGS determined from metallographic examination of samples austenitized at different temperature and time combinations. 50

Table 11. K and D_o values, which are calculated using Eq 13 and the data tabulated at Table 10..... 51

Table 12.Q and K_0 values of DIN 22NiCrMo2-2 53

Table 13.The t8/5 times used to determine the CCT diagram 59

Table 14.Transformation kinetic parameters for the model..... 71

Table 15.Variable and fixed parameters and their values used in the Taguchi experiment 77

Table 16.Chemical composition of DIN 22NiCrMo2-2 steel and DIN 16MnCr5 steel 78

Table 17.3-factorial and 2-level Taguchi type test matrix 78

LIST OF FIGURES

Figure 1. Scheme of correlation of the hardening phenomena [4]..... 2

Figure 2. The Fe-C equilibrium diagram up to 6.67 wt% C. Solid lines indicate Fe-Fe_3C diagram; dashed lines indicate iron-graphite diagram [9]..... 6

Figure 3. Plot of total case depth versus carburizing time at four selected temperatures [13]..... 9

Figure 4. Schematic representation of grain growth via atomic diffusion [19]..... 12

Figure 5. Change in grain diameter versus the holding time at various temperatures, showing the grain growth kinetics in a brass sample [19]..... 13

Figure 6. Nucleation rate(N) versus temperature for both homogeneous and heterogeneous nucleation, degree of supercooling (ΔT) for each is also shown [19]..... 16

Figure 7. The change of volume percent and number density of transformed phase as a function of time, during a typical diffusional phase transformation [24]..... 19

Figure 8. Schematic representation of a typical TTT diagram (a), and the corresponding Avrami curves (b) [24]..... 20

Figure 9. CCT curves of AISI 1040 steel (%0.39C, %0.72 Mn, %0.23 Si) (a) and AISI 4340 steel (%0.41C, %0.87 Mn, %0.28 Si, %0.72 Cr, %0.20 Mo, % 1.83 Ni) (b) [31]..... 22

Figure 10. Carbon gradient in 25 mm diameter test bar (a) and the micro-hardness profile of 16 mm test bar (b) of 8620 steel after gas carburization at 925 °C [13]..... 23

Figure 11. Hardenability multiplying factors for carbon at various austenitizing conditions [34] 25

Figure 12. Radial hardness profiles for (a) 50 mm (2 in.) diameter cylindrical 1040 and 4140 steel specimens quenched in mildly agitated water, and (b) 50 and 75 mm (2 and 3 in.) diameter cylindrical specimens of 4140 steel quenched in mildly agitated oil [19] 26

Figure 13. a) Rolling direction of DIN 22NiCrMo2-2 billet b) Billet sample which is used for macro analysis 28

Figure 14. The surface of the DIN 22NiCrMo2-2 steel specimens after macro-etching 28

Figure 15. Metallographic investigated sections of DIN 22NiCrMo2-2 steel billet (note that the rolling direction of the photographed billet is its surface normal) 29

Figure 16. Optical micrographs taken at 50x magnification via optical microscope from the head, middle and end sections of the billet 30

Figure 17. Optical micrographs taken at 200x magnification via optical microscope from the head, middle and end sections of the billet 31

Figure 18. Histogram of ferritic and pearlitic microstructures 32

Figure 19. Ferrite and perlite grain size distributions of the head, middle, end of the billet for section 1 34

Figure 20. Microstructure of the head section of the billet shown at 50x magnification, the results of banding degree analysis (grading were made for pearlite with dark color) 37

Figure 21. Microstructure of the middle section of the billet shown at 50x magnification, the results of banding degree analysis (grading were made for pearlite with dark color) 37

Figure 22. Microstructure of the end section of the billet shown at 50x magnification, the results of banding degree analysis (grading were made for pearlite with dark color) 38

Figure 23. SEM micrograph of the banded structure of 22NiCrMo2-2 steel. The rectangle indicates the area, at which elemental mapping (via EDS) is performed... 38

Figure 24. The results of the EDS mapping performed on the area shown in Figure 23 for the 22NiCrMo2-2 steel. The secondary electron micrograph (top) of the region analyzed, and the distribution of Mn (bottom) is given. 40

Figure 25. Linear EDS analyzes made on the banded structure for DIN 22NiCrMo2-2 steel, C and Mn distributions (top), secondary electron image of the region where the linear analysis is performed (below). 40

Figure 26. %Carbon isopleth of DIN 22NiCrMo2-2 steel calculated with the Thermocalc® software, dashed line indicate the carbon percent of DIN 22NiCrMo2-2 initial composition..... 42

Figure 27. Geometry of the samples which were used to determine prior austenite grain size..... 46

Figure 28. Optical micrographs of the specimens taken at 200x under bright field illumination. 48

Figure 29. The PAGS values of the current study, compared to the reference study of E.Khzouz's; plotted as a function of austenization temperature..... 49

Figure 30. Trendlines of grain sizes and effective time..... 52

Figure 31. Trendline of lnK values and 1/T values..... 52

Figure 32. The calculated K and Do values of the current study compared to the E.Khzouz's study 53

Figure 33. (a) Chamber of Baehr-Thermoanalysis GmbH, DIL 805 A/D dilatometer and (b) induction coil used in DIL 805 A/D. 56

Figure 34. Technical drawing of the dilatometer test specimens used to determination of the CCT and also M_s and M_f temperatures..... 56

Figure 35. A typical dilatometric curve which represents the change in length as a function of temperature. 57

Figure 36. The temperature-time program of the CCT tests..... 58

Figure 37. Relative change in length vs. temperature curve for 400s t8/5 time CCT test 59

Figure 38. SEM micrographs of the samples taken at 5000x magnification. The corresponding t8/5 times are given in upper left corner of each micrograph 61

Figure 39. SEM micrographs of the samples taken at 5000x magnification. The corresponding t8/5 times are given in upper left corner of each micrograph 62

Figure 40. SEM micrographs of the samples taken at 5000x magnification. The corresponding t8/5 times are given in upper left corner of each micrograph 63

Figure 41. Comparison of CCT diagrams of DIN 22NiCrMo2-2(SAE 8620H) steel obtained experimentally and via JMatPro® software. Dashed lines refer as the cooling rate. (Composition: 0.21% C, 0.84% Mn, 0.33% Si, 0.53% Ni, 0.57% Cr, 0.24% Mo) 64

Figure 42. 8620 CCT diagram. Composition: 0.17% C, 0.82% Mn, 0.31% Si, 0.52% Ni, 0.50% Cr, 0.20% Mo. Austenitized at 925°C. Grain size: 9 [31] 65

Figure 43. Temperature program for sub-zero test 66

Figure 44. Change in length vs. temperature curve for sub-zero test, region 1 indicate the transformation of the austenite phase to the martensite phase. 67

Figure 45. Change in length vs. temperature curve which represent to martensitic transformation 68

Figure 46. Martensite fraction vs. temperature curves determined by experimentally and fitting of the Koistinen-Marburger equation 69

Figure 47. Change in length vs. temperature curve which represents to the austenite transformation 69

Figure 48. Comparison of TTT diagrams for the DIN 22NiCrMo2-2(SAE 8620H) steel 71

Figure 49. TTT diagram of 8620 steel; composition: 0.18 C, 0.79 Mn, 0.52 Ni, 0.56 Cr, 0.19 Mo. Austenitized at 899°C. Grain size: 9-10. A_{c3}: 825°C. A_{c1}: 745°C [31] 72

Figure 50. The surface hardening thermochemical heat treatment procedure made on cam shaft. 75

Figure 51. The regions, from which samples are extracted from shafts for metallographic and hardness tests. Sample codes are: number 1 is stepless, number 2 is stepped-Ø47.5, and number 3 is stepped-Ø70 shafts. 79

Figure 52. Hardness and %Carbon content graphs of the 1st (T910_%C0.9_Toil60_F1) and 5th (T910_%C0.9_Toil60_F2) sets of DIN 22NiCrMo2-2 steel with stepped and stepless shaft varying from surface to center. 80

Figure 53. Hardness and %Carbon content graphs of the 2nd (T910_%C1.1_Toil70_F1) and 6th (T910_%C1.1_Toil70_F2) sets of DIN 22NiCrMo2-2 steel with stepped and stepless shaft varying from surface to center. 80

Figure 54. Hardness and %Carbon content graphs of the 3rd (T930_%C0.9_Toil70_F1) and 7th (T930_%C0.9_Toil70_F2) sets of DIN 22NiCrMo2-2 steel with stepped and stepless shaft varying from surface to center. 81

Figure 55. Hardness and %Carbon content graphs of the 4th (T930_%C01.1_Toil60_F1) and 8th (T930_%C01.1_Toil60_F2) sets of DIN 22NiCrMo2-2 steel with stepped and stepless shaft varying from surface to center. 81

Figure 56. Comparison of surface and center hardness of DIN 22NiCrMo2-2 steel for stepless shaft. 83

Figure 57. Hardness distributions of the DIN 22NiCrMo2-2 and DIN 16MnCr5 steels for the 1st test set 84

Figure 58. Hardness distributions of the DIN 22NiCrMo2-2 and DIN 16MnCr5 steels for the 5st test set 84

Figure 59.Comparison of hardness distributions of the 1st (T910_%C0.9_Toil60_F1) and 3st (T930_%C0.9_Toil70_F1) test sets for the DIN 22NiCrMo2-2 86

Figure 60. Comparison of hardness distributions of the 2nd (T910_%C1.1_Toil70_F1) and 4th (T930_%C1.1_Toil60_F1) test sets for the DIN 22NiCrMo2-2 86

Figure 61. Optical micrographs of the 1st and 5th test sets of 22NiCrMo2-2 steel taken at 200x magnification, from shell and center regions for stepless and stepped shafts 87

Figure 62. Optical micrographs of the 1st and 5th test sets of 16MnCr5 steel taken at 200x magnification, from shell and center regions for stepless and stepped shaft. ... 88

Figure 63. Calculation of total case depth using a panoramic micrograph 89

Figure 64. Case Depth vs. Experimental Sets for Stepless and Stepped_Ø47.5 Shaft of DIN 22NiCrMo2-2 and DIN 16MnCr5 Steels 90

Figure 65. Comparison of hardness results of simulations and experiments on T930, % C1.1, Toil60, F1- F2 conditions for stepless shaft 91

Figure 66. Comparison of hardness results of simulations and experiments on T930, % C1.1, Toil60, F1- F2 conditions for stepped shaft 91

Figure 67. Comparison of experimental and simulation results in 1st, 2nd, 3rd and 4th test sets 92

Figure 68. Comparison of experimental and simulation results in 5th, 6th, 7th and 8th test sets 92

Figure A. 1. Ferrite and pearlite aspect ratio distributions of section 1 for the head, middle, end of the billet 105

Figure A. 2. Ferrite and pearlite angle distributions of section 1 for the head, middle, end of the billet 106

Figure A. 3. Ferrite and pearlite circularity distributions of section 1 for the head, middle, end of the billet 107

Figure A. 4. Optical micrographs of the 2nd and 6th test sets of 22NiCrMo2-2 steel taken at 200x magnification, from shell and center regions for stepless and stepped shaft. 108

Figure A. 5. Optical micrographs of the 2nd and 6th test sets of 16MnCr5 steel taken at 200x magnification, from shell and center regions for stepless and stepped shaft. 109

Figure A. 6. Optical micrographs of the 3rd and 7th test sets of 22NiCrMo2-2 steel taken at 200x magnification, from shell and center regions for stepless and stepped shaft. 110

Figure A. 7. Optical micrographs of the 3rd and 7th test sets of 16MnCr5 steel taken at 200x magnification, from shell and center regions for stepless and stepped shaft 111

Figure A. 8. Optical micrographs of the 4th and 8th test sets of 22NiCrMo2-2 steel taken at 200x magnification, from shell and center regions for stepless and stepped shaft. 112

Figure A. 9. Optical micrographs of the 4th and 8th test sets of 16MnCr5 steel taken at 200x magnification from, shell and center regions for stepless and stepped shaft. 113

LIST OF ABBREVIATIONS AND SYMBOLS

Abreviations

BCC	Body-Centered-Cubic
CCT	Continuous Cooling Transformation
CALPHAD	CAlculation of PHAse Diagrams
EDS	Energy Dispersive X-Ray Spectrometer
FCC	Face-Centered-Cubic
HV	Vickers Hardness
OES	Optical Emission Spectrometer
PAGS	Prior Austenite Grain Size
SEM	Scanning Electron Microscope
TTT	Time Temperature Transformation

Symbols

D	Average grain size
D_0	Initial grain size
K	Temperature-dependent parameter
t	Holding time
m	Grain growth exponent
R_{cr}	Critical Radius
A	Constant
r	Mean second phase particle radius
f	Volume fraction of second phase particles.
r^*	Critical radius

ΔG^*	Activation free energy
ΔG_v	Volume free energy
γ	The surface free energy
$S(\theta)$	Contact angle of a precipitate along as grain boundary
ΔT	Degree of supercooling
$\dot{G}$	Growth rate
Q	The activation energy
C	Pre-exponential
J	Diffusion flux
D	Diffusion coefficient
dc/dx	Concentration gradient
Cs	Constant concentration of the diffusing atom on the surface
C_0	Initial uniform concentration of the diffusing atoms in the material
x	Large distance
K	Diffusion rate
K_0	Temperature-independent pre-exponential (m^2/s)
R	Gas constant (8.31 J/mol-K or 8.62 eV/atom-K)
T	Absolute temperature (K)
$P(t)$	Amount of new phase transformed in time *t*, in Johnson-Mehl-Avrami equation
t	Time
t8/5	Characteristic time
k	Temperature sensitive constant
n	Numerical exponent
a	Adjustable parameter,
Ms	Martensitic start temperature

G	Grain size (per ASTM E112)
A_S	Asymptotic temperature (K)

CHAPTER 1

INTRODUCTION

Steels are produced with different mechanical properties according to their usage in the industry. The mechanical properties of the steels vary considerably depending on the applied heat treatments, microstructures, alloying elements in the chemical composition and grain sizes. Heat treatment is a concept that encompasses all of the heat-based processes for improving or changing the properties of metal materials. The heat treatment of a metal part involves the heating of the material between certain temperatures taking into account the phase diagram of that metal, keeping it at these temperatures, and then quenching to the ambient temperature at certain cooling rates.

Many heat treatments such as carburizing, normalization, tempering and austempering are applied to the steels and the properties of the materials are developed and produced in accordance with the intended purposes. Carburizing is a commonly applied surface hardening heat treatments in which carbon diffuses into the steel surface in order to obtain a hardened layer at a certain depth. The carburizing surface hardening process is applied in particular to provide high hardness, fatigue strength and wear resistance in the surfaces and high toughness in the inner parts.

Quality of carburizing heat treatment depend on heat treatment process conditions such as carburizing time, carburizing temperature, carbon potential of carburizing atmosphere, cooling rate, cooling (quenching) medium. The hardness and case depth measurements are important for the quality control of surface hardened steel parts and carburizing heat treatment process. Because case depth and surface hardness influence the structural differences, internal stresses, probability of cracking and also fatigue strength.

In addition, microstructure studies guide the carburizing process, which in turn helps to improve the performance of carburized steel products during the service [1]. The carburizing hard and resistant case which is formed by phase transformation at the surface can carry more compressive stress and the compressive residual stresses reduce the effect of applied tensile stress [1], [2]. During carburizing heat treatment, microstructure changes occur depending on chemical composition (i.e. alloying elements and carbon) and cooling rate. For the case of carburizing, the carbon concentration has a more profound effect. For these reasons, the prediction of the resulting properties of the work-piece after carburized-quenching depends on determination of the microstructure type and properties which are changed after heat treatment. Additionally, the heat treatments applied to the steels are related to the transformation of the austenite phase. Therefore to obtain the desired properties, the conditions of cooling of the heat treated part must be carefully selected. In general, this is accomplished using continuous cooling transformation (CCT) or isothermal transformation (IT) diagrams.

The inter-relation between mentioned temperature, phase transformations and mechanical phenomena is summarized briefly in Figure 1. The proportions of the carbon and other alloying elements in the steel and the applied heat treatment(s) influence the microstructure of steel, which in turn makes it possible to obtain better mechanical properties [3].

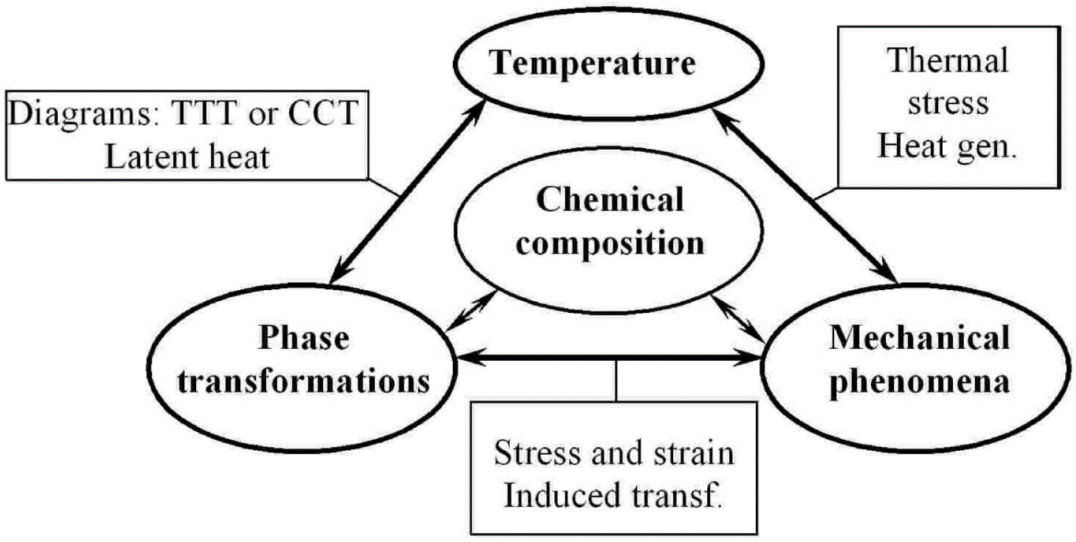

Figure 1. Scheme of correlation of the hardening phenomena [4]

1.1. Aim And Motivation of Study

The quality assessment of the carburizing heat treatment result is carried out with determination of surface hardness and case depth which vary depending on the heat treatment process parameters. And it is important that the carburizing process parameters which are effective on quality of carburizing treatment should be determined with little trial and error. For that purpose in recent years, carburizing and quenching simulation studies are carried out to reduce problems such as cracking, inadequate case depth and surface/core hardness. Also it is possible to increase the product performance by decreasing the distortion and optimizing the distribution of residual stresses using heat treatment simulations. At the same time, the heat treatment simulations save labor, cost and time.

The success of heat treatment simulations, as for any other simulation study, rely on the accuracy of input data. A brief summary of the material properties (i.e. input data) required for the simulation of carburizing and similar heat treatments is presented in Table 1. Moreover, ensuring the success of simulation studies requires verification via experimental studies.

For that purpose the present study has 2 main aims. First aim is obtain the DIN 22NiCrMo2-2 (SAE 8620H) materials data set for simulation studies also one of obtained properties are highlighted in Table 1. Through the determination of material inputs, an infrastructure will be created to simulate the process of carburizing and quenching for the DIN 22NiCrMo2-2 (SAE 8620H) material in the virtual environment with the heat treatment simulation software (SYSWELD®). In line with this aim, firstly information about carburizing heat treatment and different carburizing techniques were given in this study. Moreover, the underlying physical metallurgical principles including grain growth kinetics, phase transformation kinetics, and factors affecting hardness and case depth were explained. Those principles which were given in Chapter 2 are essential for understanding fundamentals of carburizing. Furthermore, material characterization studies, which are important effect in determine the quality of the carburizing heat treatment, have been made for the DIN 22NiCrMo2-2 steel. Also macro-chemical analysis, micro-chemical analysis, quantitative and qualitative metallographic analysis which were performed for characterization of the raw materials and the phase diagram which was determined in the Thermocalc® software

were represented in Chapter 3. Since the austenite grain size affects the transformation temperatures and times during quenching, austenite grain growth kinetics was studied to estimate the properties to be obtained after carburizing in Chapter 4. CCT and TTT diagrams of DIN 22NiCrMo2-2 steel were determined in Chapter 5 for the determination of phase transformations kinetics which are affect the mechanical properties of the material as a result of the carburizing quenching process.

At the same time, this study is a part of a larger scale project and this project purpose to solve problem of shafts which are expected to operate for a long time under severe conditions and are prone to wear and fatigue. Also in industrial using of the shafts which are subjected to carburizing, there are problems such as, cracking, inadequate microstructure, lack of desired hardness depths and excessive distortion. Since these properties are predominantly determined by the process conditions during carburizing, project aims at defining the effective process parameters and minimize the variability of carburized quenching process via computer simulations and industrial scale tests. For that purpose this project consist of 3 studies. First study include carburizing heat treatment studies which are performed on DIN 22NiCrMo2-2 and DIN 16MnCr5 steels with Design of Experiments (DoE) using the Taguchi method [5]. Second study include carburizing experiments were carried out using computer simulation with same DoE for the DIN 16MnCr5 steel [6]. As a last part of this project, this thesis study complements those studies. Consequently, second aim of this study is characterization of the shafts in order to investigation of carburizing quality assessment and evaluate the compatibility between experimental and simulation studies. So in line with this aim, in Chapter 6 of this study, the hardness distribution and microstructure of 22NiCrMo2-2 and 16MnCr5 steels were investigated. Finally, for the 16MnCr5 steel, the experimental carburizing heat treatment hardness and microstructure results are compared with the carburizing simulation results which were obtained via SYSWELD® software.

Table 1. Summary of required material properties for application to heat treatment simulations (plus sign indicates required parameters) [7]

MATERIAL PROPERTIES	HEAT TREATMENT PROCESSES					
	Heating	Hardening	Carburizing	Carbonitriding	Induction Hardening	Tempering
Density	+	+	+	+	+	+
Thermal Conductivity	+	+	+	+	+	+
Specific Heat Capacity	+	+	+	+	+	+
Transformation Enthalpy	+	+	+	+	+	+
Enthalpy	+	+	+	+	+	+
Young's Modulus	+	+	+	+	+	+
Poisson's Ratio	+	+	+	+	+	+
Thermal Expansion Coefficient	+	+	+	+	+	+
Transformation Strain	+	+	+	+	+	+
Thermal Strain	+	+	+	+	+	+
Flow Curve	-	+	+	+	+	-
Creep Curve	+	-	-	-	-	+
TRIP Constant	-	+	+	+	+	-
Transformation Parameters	+	+	+	+	+	+
Electrical Conductivity	-	-	-	-	+	-
Magnetic Permeability	-	-	-	-	+	-
Diffusion Coefficient	-	-	+	+	-	-
Henry Activity Coefficient	-	-	+	+	-	-
Wagner Interaction Constants	-	-	-	+	-	-
Solubility	-	-	+	+	-	-

CHAPTER 2

THEORY AND LITERATURE SURVEY

2.1. Theory of Carburizing

Carburizing is one of the methods of surface hardening, in which carbon is diffused on the surface of low carbon steel after heating the steel to austenite phase temperature in an environment containing high carbon potential. Typically 850-950ºC (in the austenite region) temperature is used and also this temperature is called carburizing temperature [8].

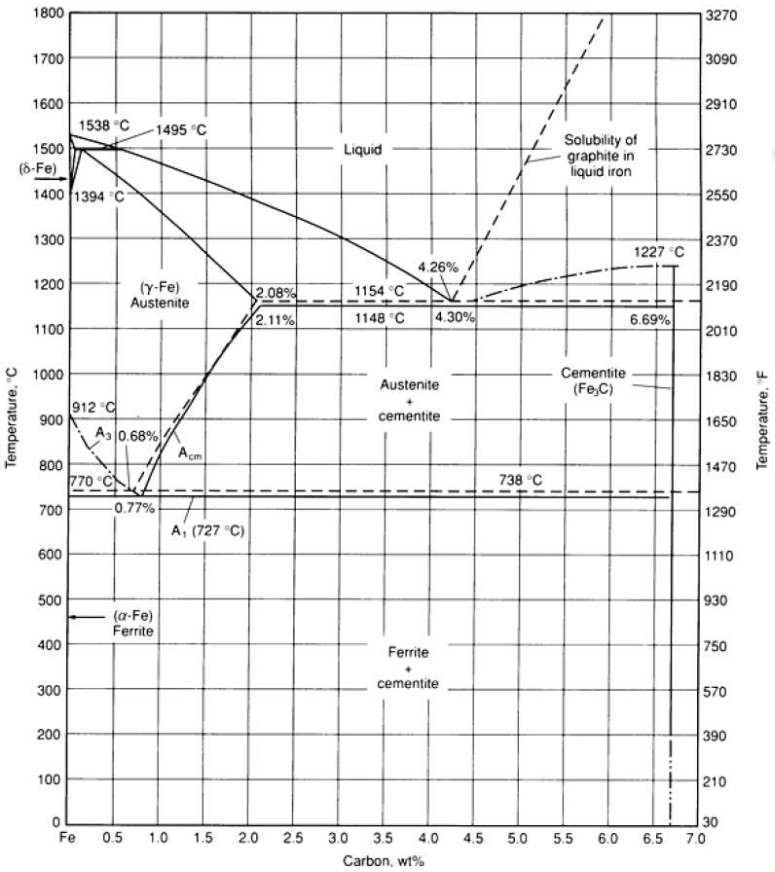

Figure 2. The Fe-C equilibrium diagram up to 6.67 wt% C. Solid lines indicate Fe-Fe_3C diagram; dashed lines indicate iron-graphite diagram [9].

It is necessary to heat up to the austenitic phase region, where the solubility of the carbon atoms of the parts is high since the solubility of carbon in the ferrite phase is very low. The maximum amount of carbon that can be solved in the austenite phase at the carburizing temperature can be found from the A_{cm} line in the Fe-C equilibrium diagram which is represented in Figure 2. In the Fe-C equilibrium diagram, it is seen that the highest carbon solubility in ferrite is 0.025% and the carbon solubility in austenite is about 2.0%. Due to the limited solubility of carbon atoms in the austenite, the carbon content of the carburizing steels must not exceed 0.8-1% to prevent from the carbides forming brittle martensite and residual austenite when the carbon content is too high [10], [11].

2.2. Carburizing Methods

Carburizing methods introduce carbon diffusion by using different atmospheres which are gas (atmospheric-gas, plasma, and vacuum carburizing), liquid (salt bath carburizing) or solid (pack carburizing). Also gas carburizing is widely used for large scale production because it can be accurately controlled and involves a minimum of special handling.

2.2.1. Pack Carburizing

Pack carburizing is a process in which carbon monoxide is removed from the solid coal dusts by the reactions that occur with the effect of temperature, and carburizing is carried out by diffusing atomic carbon, which is decomposed from carbon monoxide, into the steel surface. The formation of carbon monoxide can be accelerated through catalysts such as barium carbonate, potassium carbonate and sodium carbonate. The most important advantage of the pack carburizing method is that there is no need for the gas atmosphere to be prepared in advance. This method is often used in the carburizing of large parts. However, controlling the amount of carbon on the surface is difficult. Another disadvantage of using this method is that extra time is required every time for heating and cooling [12].

2.2.2. Liquid Carburizing

Liquids carburizing is carried out by immersing the pieces in molten cyanide baths (Na, CN, KCN, $NaCO_3$, NaCI), and the carbon source is the CO gas generated during the process. Salt baths are usually used in small and medium sized pieces. This process is more economical in parts with less depth of carburizing. The total time of the procedure is shorter than other carburizing methods. Because the salt material is completely wrapped, the carburizing is homogeneous and the material surface remain clean. The parts are less deformed because of they are swung in the bath with their own weight. However, the high costs of large carburizing depths, the toxicity of cyanide salts, the size of the pots in large parts and the difficulties in application are the disadvantages of the salt bath [13], [14].

2.2.3. Gas Carburizing

This is the most commonly used surface hardening method in recent years. With this method, good and reliable results can be obtained. Hydrocarbons such as methane (CH_4), ethane (C_2H_6), propane (C_3H_8) are used as carbon source for gas carburizing. The atomic carbon penetrates the steel surface which is at the austenite phase and forms a carbon-rich carburizing layer on the surface [15].The depth of carburizing depends on the duration of the steel part in the furnace. After the carburizing process is completed, the appropriate hardening method is selected depending on the steel grade used. This method is very convenient for situations where precise tolerable depth of carburizing is desired. Other advantages of gas carburizing are the ease of quick movement for direct quenching from the carburizing temperature, and the maintenance of a clean working environment.

2.2.3.1. Process Parameter of Gas Carburizing

Gas carburizing process variables are temperature, time and atmosphere composition. In the gas carburizing process, the amount of carbon in the furnace atmosphere must be greater than the amount of carbon in the part in order to provide carbon diffusion on the surface. Because the carbon potential difference between the atmosphere and the part is the driving force for the diffusion to take place. The carbon diffusion rate

also increases with increasing temperature. The carbon diffusion at 925ºC is 40% higher than the carbon diffusion at 870ºC. The most commonly used temperature for carburizing is 925ºC. This temperature provides rapid rate of carburizing, without disturbing the furnace equipment which is partly heat resistant. Carburizing temperature can be increased to 955ºC or 980ºC to achieve hardness depth in a shorter time. The effect of time and temperature on case depth is given in Figure 3. As time and temperature increase, the depth of hardness increases. As the temperature increases, the time for carburizing seems to decrease [13], [16].

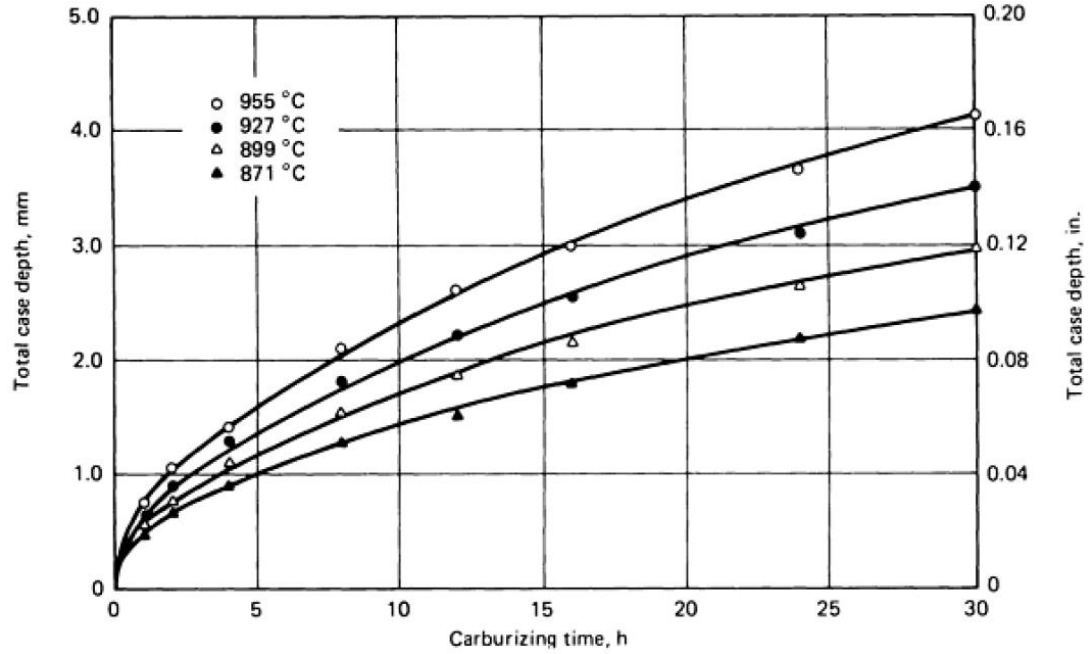

Figure 3. Plot of total case depth versus carburizing time at four selected temperatures [13]

2.2.4. Steel Grades For Carburizing

Case hardening steels, which are used in the manufacture of parts resistant to variable and impact stresses and have a hard and abrasion resistant surface and soft and tough core, are low carbon unalloyed or low carbon alloyed steels. Case hardening steels are used in the manufacture of parts such as gears, millers, roller bearings and cutting tools. Case hardening steels are cheaper than high carbon steels with tool steel that can give the same hardness on the surface. Also inner parts of case hardening steels can be

easily processed. Table 2 list the nominal chemical compositions of some of the commonly used grades.

Table 2. Chemical compositions of selected steels for carburizing [17]

	Steel (AISI-SAE No.)	C	Mn	Ni	Cr	Mo
Carbon Steels	**1018**	0.18	0.65	-	-	-
	1020	0.20	0.45	-	-	-
	1022	0.22	0.85	-	-	-
Low-alloy steels	**4118**	0.18	0.85	-	0.50	0.12
	4620	0.20	0.55	1.85	-	0.25
	4820	0.20	0.60	3.50	-	0.25
	5120	0.20	0.85	-	0.80	-
	8617	0.17	0.85	0.55	0.50	0.20
	8620	0.20	0.85	0.55	0.50	0.20
	8720	0.20	0.85	0.55	0.50	0.25

2.2.5. Advantage and Disadvantages in Comparison to Other Case Hardening Methods

The benefits of the most common methods of surface hardening are compared in Table 3. Flame and induction hardening are generally limited to certain families of steels, such as medium-carbon steels, medium-carbon alloy steels, some cast irons, and the lower-alloy tool steels. There is no size limit to parts that can be flame hardened, because only the portion of the part to be hardened need be heated. Flame hardening is generally used for very heavy cases (in the range of approximately 1.2 to 6 mm, or 0.6 to 0.25 in.); thin case depths are difficult to control because of the nature of the heating process. Transformation hardening introduces surface compressive residual stresses, which are beneficial for fatigue strength. However, in selective hardening, some residual tensile stress will exist in the region where the hardened zone meets the unhardened zone. Consequently, selective hardening by methods such as flame or induction heating should be applied away from geometric stress concentrations. Both

nitriding and carburizing provide good resistance to surface fatigue and are widely used for gears and cams [17], [18].

Table 3. Relative benefits of five common surface-hardening processes [13]

Process	Benefits
Carburizing	Hard, highly wear-resistant surface (medium case depths); excellent capacity for contact load; good bending fatigue strength; good resistance to seizure; excellent freedom from quench cracking; low-to-medium-cost steels required; high capital investment required
Carbonitriding	Hard, highly wear-resistant surface (shallow case depths); fair capacity for contact load; good bending fatigue strength; good resistance to seizure; good dimensional control possible; excellent freedom from quench cracking; low-cost steels usually satisfactory; medium capital investment required
Nitriding	Hard, highly wear-resistant surface (shallow case depths); fair capacity for contact load; good bending fatigue strength; excellent resistance to seizure; excellent dimensional control possible; good freedom from quench cracking (during pretreatment); medium-to-high-cost steels required; medium capital investment required
Induction hardening	Hard, highly wear-resistant surface (deep case depths); good capacity for contact load; good bending fatigue strength; fair resistance to seizure; fair dimensional control possible; fair freedom from quench cracking; low-cost steels usually satisfactory; medium capital investment required
Flame hardening	Hard, highly wear-resistant surface (deep case depths); good capacity for contact load; good bending fatigue strength; fair resistance to seizure; fair dimensional control possible; fair freedom from quench cracking; low-cost steels usually satisfactory; low capital investment required

2.3. Theory of Grain Growth

Grain growth is the increase in average grain size by the movement of grain boundaries in polycrystalline materials. The microstructure of the materials, especially the grain size, affects the mechanical properties of the materials. It is difficult to determine and control the grain size during the phase transformation of the material.

In the grain boundary region, which is a few atoms wide, there is a discontinuity or deviation in the atomic packing while the transition from the crystal orientation of one grain to the orientation of the other grains. The grain boundaries are regions with high energies because the atoms are bound to each other more irregularly at the grain boundaries (such as different bond angles and longer bond distances). The magnitude of this energy depends on the degree of the orientation difference and is greater for high angle grain boundaries. Also grain boundaries are the driving force in grain growth because these regions where the atoms are irregular packed and they have relatively high energies.

If the grain boundary area is reduced by grain growth, a lower total energy is obtained in the material. Grain growth requires the movement of grain boundaries, and the consumption of other grains will allow some grains to grow. For grain growth, atoms that are diffuse must pass the grain boundaries. For this reason, the growth of grain boundaries is related to the activation energy required to pass an atom through the grain boundary. The increase in grain boundary unit surface energy in fine grained materials makes the small grain unbalanced in the high temperature. In order to reduce this energy, grain growth occurs with relatively large grains consuming small grains. The growth of the grains takes place by the displacement of the grain boundaries and never occurs as a combination of the two grains. The movement of the grain boundaries is not constant and the direction may change. In addition, grain boundaries and atoms move in opposite directions as shown in Figure 4 [9].

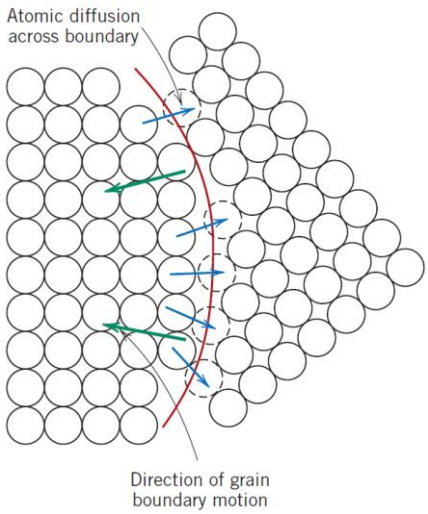

Figure 4. Schematic representation of grain growth via atomic diffusion [19]

The kinetics of grain growth are represented by following equation,

$$D^m - D_o^m = Kt \qquad \text{Eq. 1}$$

where D is the average grain size, D_o is the initial grain size ($D > D_o$), K is a temperature-dependent parameter which is increased with high temperature and low activation energy, t is holding time and m is grain growth exponent [20], [21].

The significant effect of heating rate on growth kinetics is seen in the Eq. 1. As the heating rate increases, the time which is required to austenite grow decreases. For this reason, the initial grain size grows as the heating rate slows down.

The effect of annealing time and temperature on grain size is shown in Figure 5. It is seen in Figure 5 that larger grain size is obtained with increasing temperature for the same annealing period. As the temperature increase, the curves are shifted to the larger grain size value in the vertical axis because the grain growth is faster as a results of the increasing diffusion rate.

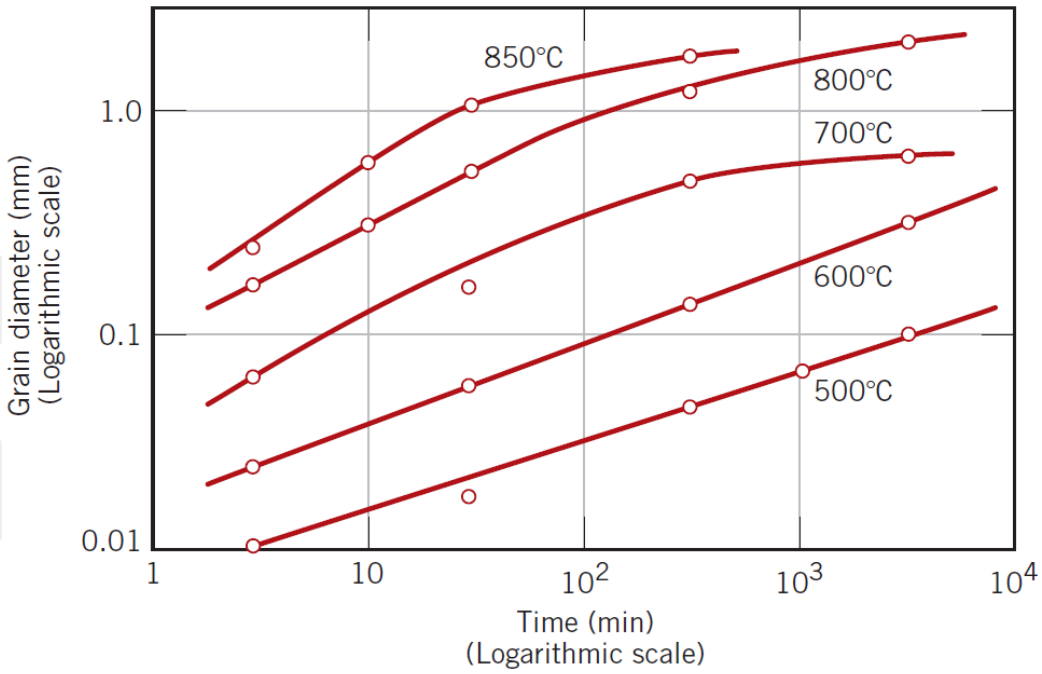

Figure 5. Change in grain diameter versus the holding time at various temperatures, showing the grain growth kinetics in a brass sample [19]

In many heat treatments where the metal is kept at high temperatures, which may cause excessive grain growth. Grain growth can be prevented by putting obstacles on grain boundaries also the second phase is used as an obstacle to the growth of the grain. The forces that prevent grain growth are called Zenner forces. The critical radius of R_{cr} is the radius at which the driving force is equal to the pinning force applied by the second phase particles to the grain boundaries. The limiting size for which grain growth can occur can be seen in the Zener Equation [22];

$$R_{cr} = \frac{A \times r}{f} \qquad \text{Eq. 2}$$

where A is a constant, r is the mean radius of second phase particles, and f is the volume fraction of second phase particles. The second phase particles, which may inhibit grain growth, also include very small oxide, sulfur, carbide or silicate particles. Zener pining can be observed at lower temperatures where the second phase particles are present, but particles may dissolve at elevated temperatures [23].

2.4. Theory of Phase Transformation

Phase transformations determine the room temperature microstructure, and so affects the mechanical properties, such as strength, hardness and ductility. Phase transformations occur with the formation of at least one new phase which differs from the initial phase in physical, chemical and microstructure. Phase transformations are generally formed as 3 different ways. One is simple diffusion-based transformations in which the chemical composition of the phases and phase number does not change (such as solidification of a pure metal, grain growth, recrystallization with allotropic transformation). Other is diffusion dependent transformations in which the phase number and chemical composition of the phases change (eutectoid transformation). Lastly phase transformation occur with diffusionless (displacive) transformations forming a metastable phase (martensite transformation).

2.4.1. Factor Affecting Phase Transformation

2.4.1.1. Nucleation

The first step of a phase transformation, the nucleation process, is transformation of small groups of atoms into a stable nuclei. At this nucleation stage, the nuclei or particles of the new phase, which consists of a few hundred atoms and have the ability to grow, will occur. If the nucleation is within the previous phase and the structure is uniformly distributed, it is called homogeneous nucleation. If the nucleation occurs around irregularities in the structure, such as surfaces, impurities, grain boundaries, and dislocations, this is called heterogeneous nucleation.

The equations for the critical radius (r^*) and the activation free energy (ΔG^*) for homogeneous nucleation of a particle are given in Eq. 3 and Eq. 4, respectively.

$$r^* = -\frac{2\gamma}{\Delta G_v} \quad \text{Eq. 3}$$

$$\Delta G^* = -\frac{16\pi\gamma^3}{3(\Delta G_v)^2} \quad \text{Eq. 4}$$

ΔG_v is volume free energy and γ is the surface free energy. ΔG^* for heterogeneous nucleation is related to ΔG^* for homogeneous nucleation by a structure factor S(θ);

$$\Delta G^*_{het} = -\Delta G^*_{hom} S(\theta) \quad \text{Eq. 5}$$

where S(θ) is the contact angle of a precipitate along as grain boundary [24].

The diagram given in Figure 6 shows that heterogeneous nucleation has a lower degree of supercooling (ΔT) than the homogeneous nucleation. Hence, heterogeneous nucleation is easier than homogeneous nucleation.

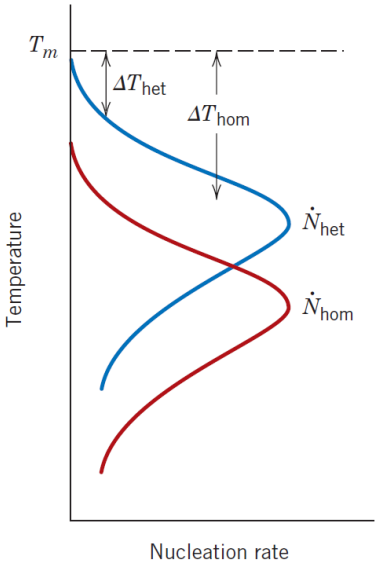

Figure 6. Nucleation rate($\dot{N}$) versus temperature for both homogeneous and heterogeneous nucleation, degree of supercooling (ΔT) for each is also shown [19]

2.4.1.2. Growth

In phase transformation, the growth phase begins when the nuclei (i.e the embryo) reaches a critical radius and becomes a stable nucleus. The growth of particles occurs as a result of atoms diffusion at long distances in several steps. This diffusion can take place at different steps during the transformation; in the main phase, passing through the phase boundary and in the core. Accordingly this, the growth rate ($\dot{G}$) is determined based on the rate of diffusion and the change in growth rate with temperature is defined as follows,

$$\dot{G} = Cexp\left(-\frac{Q}{kT}\right) \quad \text{Eq. 6}$$

where Q (the activation energy) and C (a pre-exponential) are independent of temperature and represent activation energy and material coefficient [19].

2.4.1.3. Diffusion

Most of the phase transformations in solid state depend on atomic motion. For this reason diffusion is the most basic concept to understand the morphology of the product phase(s) and also the kinetics of the transformations.

Fick's First Law, shown in Eq. 7 illustrates the diffusion flux for steady-state diffusion. Also Fick's Second Law illustrates how diffusion of atoms depends on time and distance in non-steady state conditions, as shown in Eq. 8.

$$J = -D\frac{d_c}{d_x} \quad \text{Eq. 7}$$

$$\frac{\partial_c}{\partial_x} = \frac{\partial}{\partial_x}\left(D\frac{\partial_c}{\partial_x}\right) \quad \text{Eq. 8}$$

In these equations, D is the diffusion coefficient with typical units cm^2/s and dc/dx is the concentration gradient [25]. Diffusion of carbon into steel takes place according to Eq. 9. The solution to this equation depends on the boundary conditions for a particular situation. One solution is

$$\frac{C_s - C_x}{C_s - C_0} = 1 - \text{erf}\left(\frac{x}{2\sqrt{Dt}}\right) \quad \text{Eq. 9}$$

where C_s is a constant concentration of the diffusing atoms at the surface of the material; C_0 is the initial uniform concentration of the diffusing atoms in the material; and C_x is the concentration of the diffusing atom at location x below the surface after time t. Eq. 9 actually shows the solution of the equation for the Fick's Second Law. Regarding this solution, it is possible to calculate the concentration of diffusing atoms in places which are close to the surface as a function of time and distance, provided that the diffusion coefficient D is constant and the concentration of the diffusing atom on the surface (C_s) and at large distance (x) within the material (C_0) remain unchanged. One of the consequences of the Fick's Second Law is that the same concentration profile can be obtained under different conditions, as long as the diffusion distance remains constant. This equation allows determining the process temperature and duration of specific heat treatments, most importantly the carburized-quenching treatment [26], [27].

The diffusion coefficient is determined mainly by the temperature, for a given material. The diffusion coefficient, which indicates the rate of atomic motion, is determined by the relation in the following equation:

$$D = D_o \exp(-Q_d/RT)$$ Eq. 10

where T is the absolute temperature (K), R is the gas constant (8.31 J/mol-K or 8.62 eV/atom-K), Q_d is the activation energy for diffusion (J/mol or eV/atom) and D_0 is a temperature-independent pre-exponential (m^2/s). As seen in this formula, the diffusion coefficient is a function of many variables, but the most important of these variables is temperature. As a general rule, the diffusion coefficient or diffusion rate doubles at every 20 °C rise in temperature. When the temperature rises, the energy provided for diffusing the atoms facilitates the exceeding of the activation energy barrier which is required for the diffusion of 1 mole of atoms. Also atoms move more easily to the new lattice site [26].

2.4.2. Kinetics of Solid State Phase Transformation

Solid state phase transformations can take place via 2 different mechanisms, (i) by diffusion of atoms (i.e. longer-range motion of atoms), (ii) by displasive motion of atoms which is smaller than the interatomic distance. The second mechanism is ideally without diffusion. Those transformation mechanisms have their distinctive kinetics and the following sub-sections will explain those kinetics.

2.4.2.1. Diffusional Phase Transformation

The development of phase transformation consists of two different stages, called nucleation and growth. The nucleus plays a role in the transformation until the critical transformation rate is reached at low temperatures. Growth governs the transformation until reaching the equilibrium state and after the equilibrium the coarsening takes place. The S –shaped transformation curve which is also known as Avrami curves and generated by the nucleation, growth and coarsening is presented in Figure 7 as the volume percent of transformed phase as a function of time. Also the number density of transformed phase as a function of time curve is presented in Figure 7.

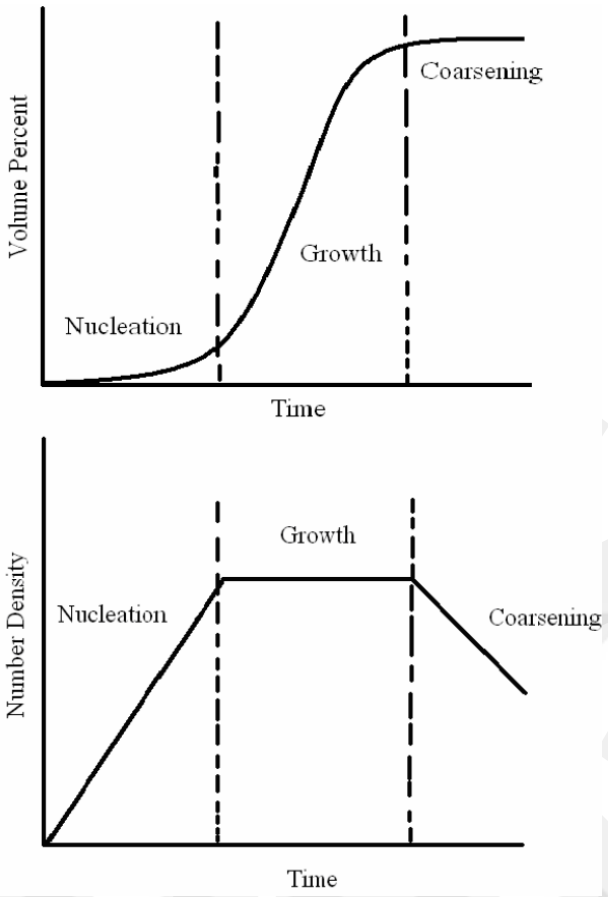

Figure 7. The change of volume percent and number density of transformed phase as a function of time, during a typical diffusional phase transformation [24]

The most frequently used isothermal model for diffusional phase transformations is described by Johnson, Mehl and Avrami and it is given in Eq. 11 :

$$P(t) = 1 - \exp(-kt^n) \qquad \text{Eq. 11}$$

where P(t) is the amount of new phase transformed, t is time, k is a temperature sensitive constant that depends on the nucleation and growth rates in min^{-1}, and n is a numerical exponent that is independent of temperature, provided there is no change in nucleation mechanism. The Avrami Equation (Eq. 11) is used to calculate a series of curves for each temperature, which are used to determine the TTT diagrams, as is presented in Figure 8 [24], [28].

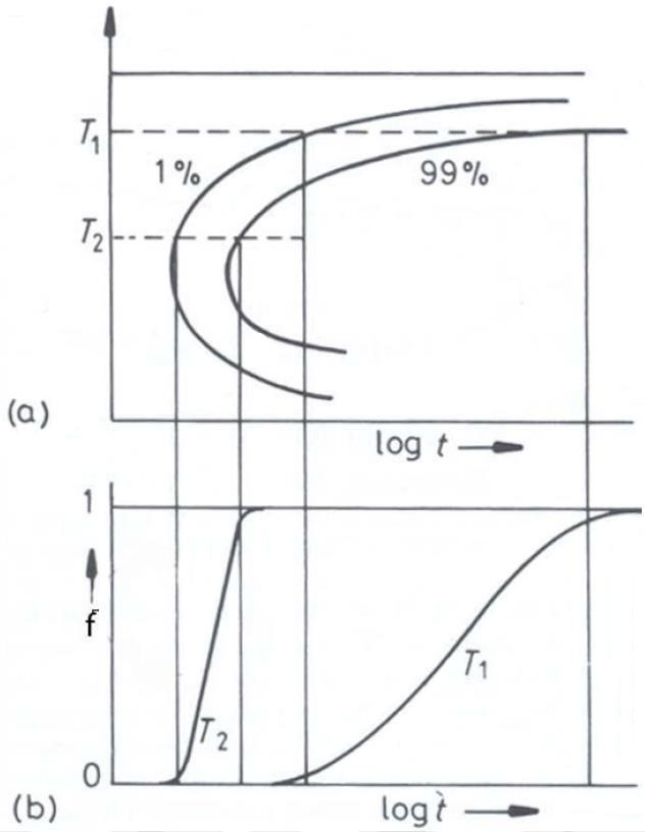

Figure 8. Schematic representation of a typical TTT diagram (a), and the corresponding Avrami curves (b) [24]

2.4.2.2. Displacive Phase Transformation

When austenite is cooled to temperatures below the A_1 temperature, the FCC (Face-Centered-Cubic) austenite immediately changes to BCC (Body-Centered-Cubic). The dissociation at these temperatures is due to the nucleation and growth of equilibrium phases. And the diffusion of these reactions requires a long time. At low temperatures, the reaction forces that cause the transformation of the FCC structure into the BCC become too large. And as a result, the phase transformation occurs before carbon diffusion begins. When the amount of carbon present is much higher than that which can be stored in solid solution, FCC lattice becomes tetragonal by distortion and this structure is called martensite. Koistinen and Marburger developed an equation for the diffusionless transformation from austenite to martensite, where the fraction of martensite, $P(t)$, is calculated as

$$P(t) = 1 - \exp\left(-\alpha(M_s - T)\right), \qquad for\ T < M_s \quad \text{Eq. 12}$$

where a is an adjustable parameter, M_s is the martensitic start temperature and T is the temperature in Kelvin [29].

2.4.3. Parameters Affecting CCT And TTT Diagram

TTT and CCT diagrams vary depending on the chemical composition and the grain size of the austenite. The growth of the austenite grains reduces the critical cooling rate by shifting the CCT and TTT diagrams to right (i.e. longer durations). As a result of this shift, formation of martensitic structure can be more easily realized. However, the coarse-grained austenite is not a highly preferred condition because it is necessary to increase the austenite temperature to obtain coarse grained structure. This can cause the steel to lose carbon (decarburization) or burn. For this reason, if it is desired to reduce the critical cooling rate to prevent impacts and cracking in steels, this is best achieved by adding alloying elements into the chemical composition of the steel.

In general, all alloying elements used in steels (except Co) lead to the formation of martensitic structures even at low cooling rates by shifting the CCT and TTT diagrams for a long time (slowing down of diffusion). Examples of these alloying elements are V, W, Mo, Cr, Mn, Si and Ni. Here, V has the strongest effect and Ni has the weakest effect on shifting of the CCT and TTT curves [30]. CCT diagram of 1040 and 4340 steel are compared as shown in Figure 9, it has been seen that the alloying elements cause the CCT diagrams of 4340 steel to shift the for a long time.

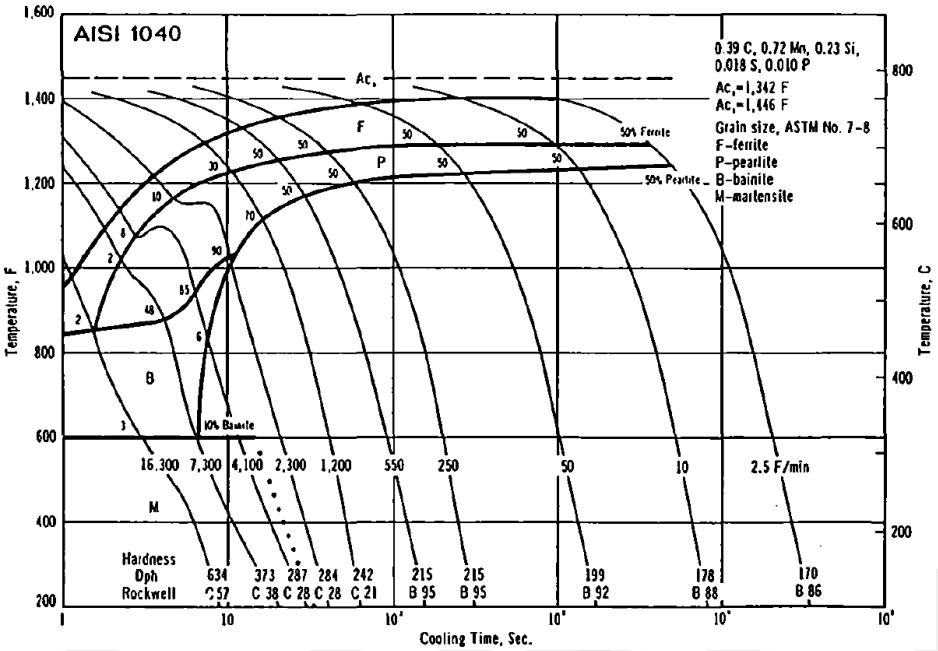

(a)

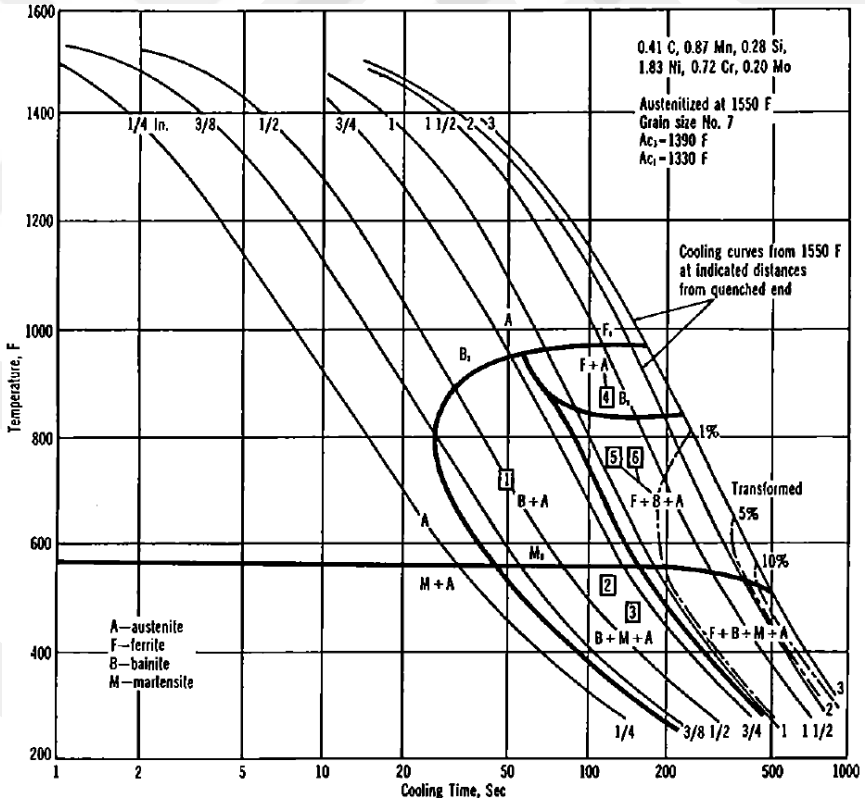

(b)

Figure 9. CCT curves of AISI 1040 steel (%0.39C, %0.72 Mn, %0.23 Si) (a) and AISI 4340 steel (%0.41C, %0.87 Mn, %0.28 Si, %0.72 Cr, %0.20 Mo, % 1.83 Ni) (b) [31]

2.5. Parameters Affecting The Hardness and Case Depth

The distance from the surface of the part to the point where the amount of carbon in the composition of the part cross section stabilizes the un-carburized condition is defined as the depth of carburizing. After carburizing, the amount of carbon is reduced from the surface to the core. Since the amount of carbon is different from the surface to the center, the hardness distribution after the hardening of the section perpendicular to the surface varies depending on the amount of carbon. Figure 10 shows, respectively, typical carbon and hardness gradients from test bars of gas-carburized SAE 8620 steel.

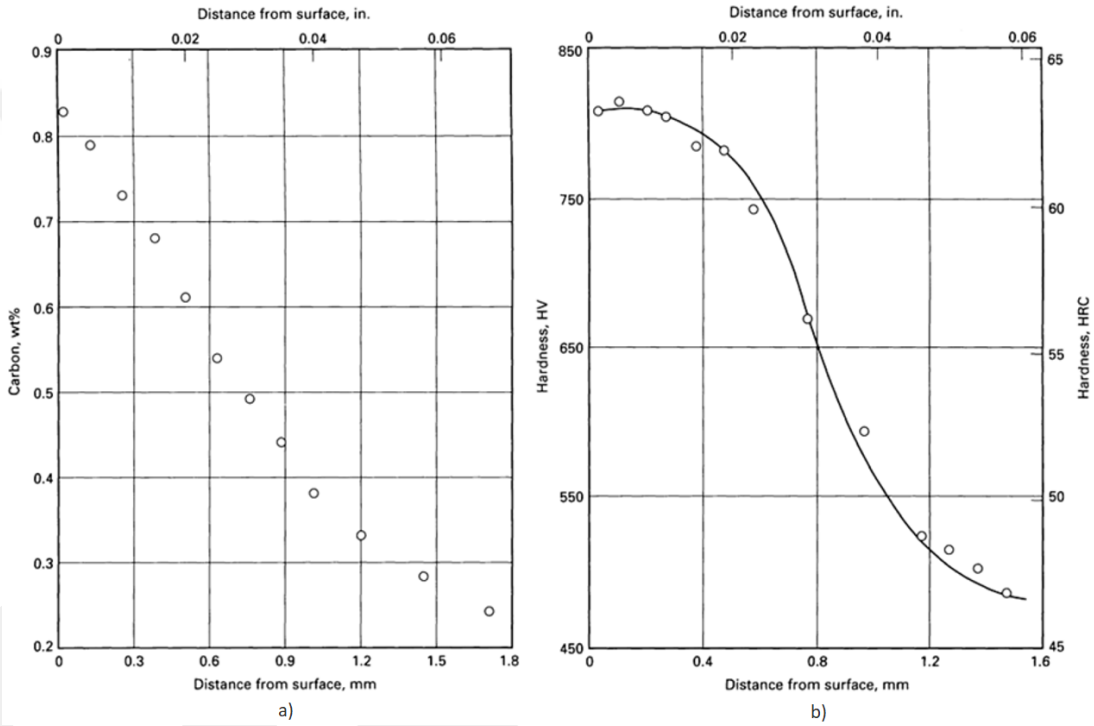

Figure 10. Carbon gradient in 25 mm diameter test bar (a) and the micro-hardness profile of 16 mm test bar (b) of 8620 steel after gas carburization at 925 °C [13].

Case depth is a generic term in order to describe the hardened case. The case depth can either be expressed as total case depth or effective case depth. If the cross-section perpendicular to the surface is polished and etched with an appropriate etchant, the carbon-diffused area appears darker than the region, to which carbon is not diffused into during carburizing. In general, the thickness of the color-changing region in metallographic examination is considered to be the total case depth. Effective case

depth is not identical to total case depth besides effective case depth is defined for a certain hardness value after carburizing. The effective case depth is defined as the vertical distance between hardened layer with 50 HRc and the surface. When carbon content is used, the effective case depth is defined in terms of carbon content is the perpendicular distance from the surface to where the carbon content reaches 0.4 wt.%. However, this value is somewhat arbitrary and threshold values of 0.5 wt.% and 0.8 wt.% carbon are also frequently used [32].

Factors affecting case depth can be listed as:

- ✓ hardenability,
- ✓ carburizing temperature and time,
- ✓ carbon potential of the carburizing environment,
- ✓ shape and size of the part,
- ✓ chemical composition of the steel,
- ✓ cooling rate during quenching.

Hardenability is the ability of the steel to harden by the formation of martensite on quenching and also hardenability determines the case depth obtained by quenching. A steel with a high hardenability has a high hardening depth. The austenite may transform to bainitic or pearlitic microstructures of lower hardness than martensite in carburizing steels with low hardenability. Austenite grain size and carbon potential affect hardenability so that effect case depth. The effect of the austenite temperature and the austenite grain size on the hardenability factor, which varies with the amount of carbon, appears in Figure 11. The areas required for ferrite and pearlite nucleation are reduced because of the decreasing grain boundary area per volume with increased austenite grain size. As a result, the hardenability increases with the slowing of ferrite and pearlite transformations [33].

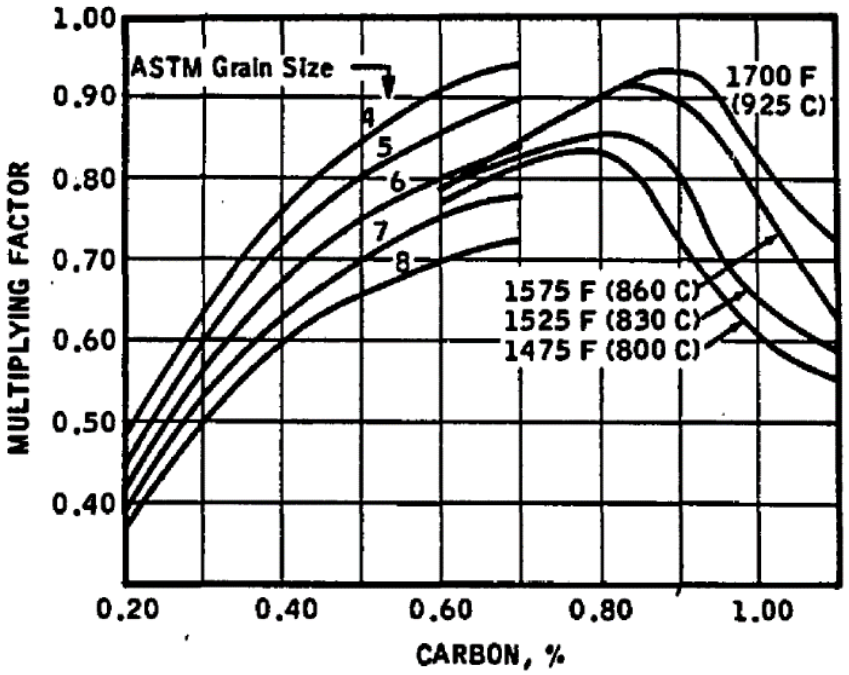

Figure 11. Hardenability multiplying factors for carbon at various austenitizing conditions [34]

In addition, specimen diameter also influences the hardness distribution, as demonstrated in Figure 12, which plots the hardness profiles for oil-quenched 4140 cylinders 50 and 75 mm (2 and 3 in.) in diameter. Since only the surface of the part during quenching is in contact with the quench medium, the ratio of the surface area to the mass is an important parameter affecting the cooling rate. The cooling rate of the part is directly proportional to the surface area/mass ratio. At the same time alloying elements, which slow down ferrite and pearlite reactions, increase the hardenability as shown in Figure 12.a.

Moreover, the temperature of the quenching medium affects the rate of cooling of the quenched part. In general, as the temperature of the quenching medium increases, the cooling rate of the quenched part decreases. If the cooling rate is slow, more time is provided for carbon diffusion besides it is possible to transformation of pearlite which is softer than martensite.

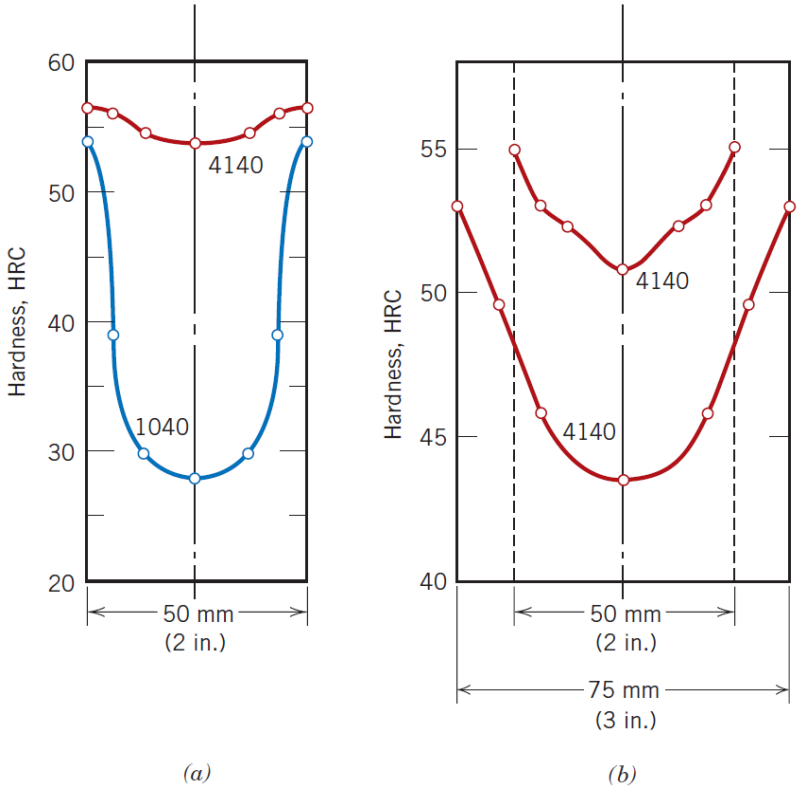

Figure 12. Radial hardness profiles for (a) 50 mm (2 in.) diameter cylindrical 1040 and 4140 steel specimens quenched in mildly agitated water, and (b) 50 and 75 mm (2 and 3 in.) diameter cylindrical specimens of 4140 steel quenched in mildly agitated oil [19]

CHAPTER 3

CHARACTERIZATION OF RAW MATERIAL

The basic information (chemical composition, initial microstructure, austenite grain size, homogeneity and related micro and macro segregation analysis) which are necessary to calculate the material properties can be determined by various measurements on the raw material. The data obtained from this experimental analysis will also be used in the theoretical analysis of the problem and in the determination of the assumptions to be made while creating the simulation templates.

3.1. Macro Chemical Analysis

Five specimens were removed for 5 different positions (including the beginning, middle and end of the billet) from the DIN 22NiCrMo2-2 billet 85 mm in diameter for macro chemical analysis. Measurements of macro chemical analysis were made via optical emission spectrometer (OBLF GS1000®). The average of the measurements was taken five times on the surface of each of the 5 samples. The average results of the measurement are given in Table 4.

Table 4. Chemical composition of DIN 22NiCrMo2-2 steel used in this study

Wt%	C	Mn	Cr	Ni	Mo	Si	P	S	Fe
Average	0.21	0.84	0.57	0.53	0.24	0.33	0.005	0.022	Bal.
Std.Dev.	±0.005	±0.011	±0.010	±0.018	±0.003	±0.018	±0.0002	±0.0007	

3.2. Macro Segregation Analysis

Cylindrical samples having a thickness about 8 – 10 mm were cut from the 85mm diameter DIN 22NiCrMo2-2 billet via Karmetal 400 KDG® band saw. Figure 13

shows the rolling direction on the part of billet, and the specimen of billet which was analyzed. The surface of the specimens were machined via the Great® Magnetic surface grinder for easy visualization of the segregation on macro-etching.

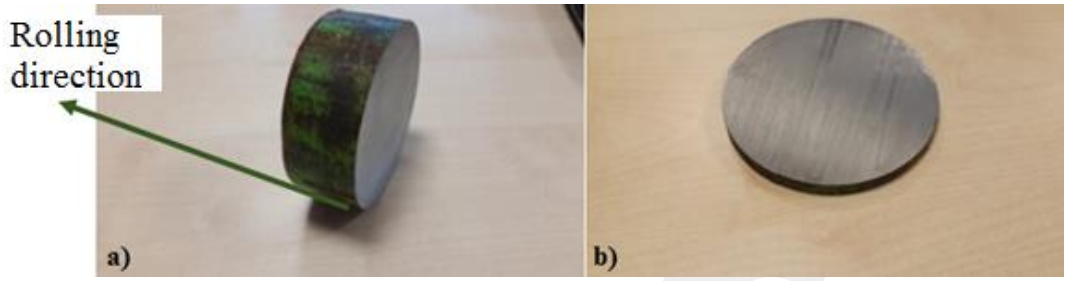

Figure 13. a) Rolling direction of DIN 22NiCrMo2-2 billet b) Billet sample which is used for macro analysis

Macro etching was performed according to ASTM E340-15 standard [35]. The etchant was composed of 40 ml HCl + 60 ml H_2O + 10 ml HNO_3 mixture. Then etchant was heated to 50-60°C just before etching the specimens. Lastly the surface of the samples were cleaned with alcohol and dried by blowing hot air.

The small differences between the two images in Figure 14 are due to the etching duration variations and also due to the lighting conditions during photographing them. Figure 14 represents that the specimens have a homogeneous structure. The low standard deviations in Table 4 (indicating the variations in the distribution of chemical elements) also confirms the homogeneity observed in Figure 14.

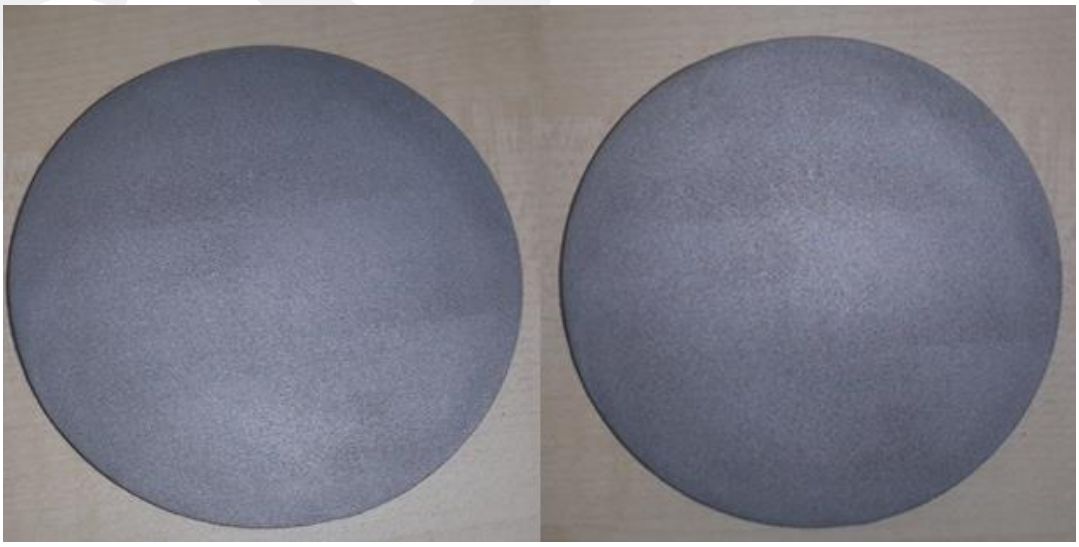

Figure 14. The surface of the DIN 22NiCrMo2-2 steel specimens after macro-etching

3.3. Microstructural Characterization

After ensuring the macro-chemical homogeneity, the microstructure of the specimens was characterized. For microstructure analysis, three different sections from the central, middle and surface regions of the DIN 22NiCrMo2-2 steel billet shown in Figure 15 were cut in a precision cutter (Struers Secotom-10).

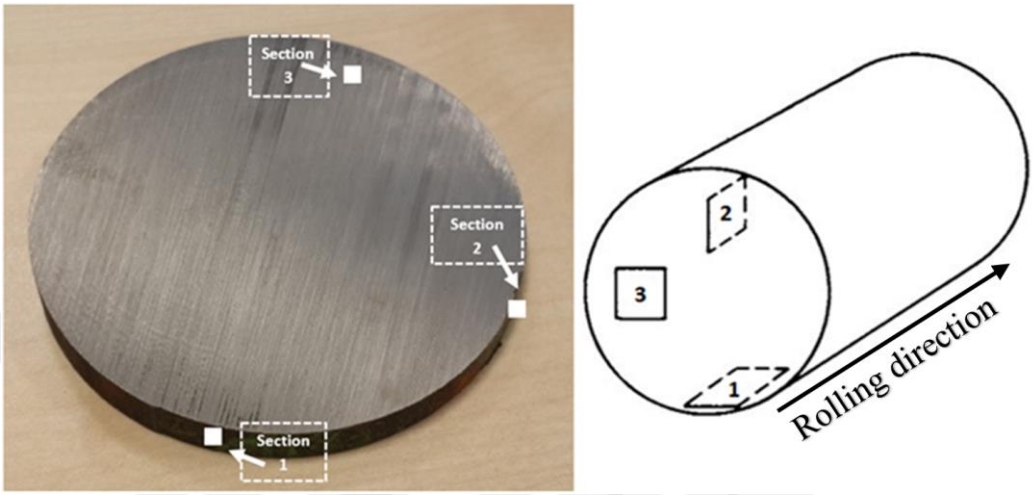

Figure 15. Metallographic investigated sections of DIN 22NiCrMo2-2 steel billet (note that the rolling direction of the photographed billet is its surface normal)

After cutting the following metallographic sample preparation procedures were applied:

- The samples were grinded with SiC papers in 6 steps (320-400-600-800-1000-1200 ANSI grit number)
- The sample surface was polished with diamond paste in 2 steps (3μm-1μm) and OPS (oxide polishing solution) using Presi Minitech 233® polishing machine
- Polished sample surfaces were etched with Nital (2 mL Nitric acid and 98 mL ethanol) and Picral (4 gr picric acid and 100 mL ethanol).

It should be noted that this prescribed metallographic sample preparation procedure is in accordance with the ASTM E3-11 standard [36]. After metallographic preparation, the microstructure of the specimens were examined in accordance with a Nikon Eclipse LV 150 optical microscope in bright field imaging mode [37]. Here, the procedures explained in ASTM E1122-96 standard were followed. For quantitative analyzes, 5 microstructure photographs were taken from randomly selected positions.

The banded structures were clearly visible in the Sections 1 and 2 as shown in Figure 16 in addition banding structure in those sections are parallel to the rolling direction. This banding structure occur because of the alloying element in steel. The C, Mn, S atoms in the segregated microstructure which are formed during the solidification are pushed toward the interdendritic region in front of or at the edge of the dendrites so that the atoms accumulate in the regions between the dendrites where the diffusion is low. Ferrite formation is observed in dendritic regions where the amount of manganese is poor since the manganese is a stabilizing element of austenite because of lowering Ar3 temperature. Consequently, pearlite formation in high carbon and manganese direction is observed in interdendritic regions which are rich in carbon content. Along with the deformation, ferrite and pearlite microstructures are progressing parallel to the direction of deformation [38]. Thus, parallel ferrite and pearlite bands / lines are observed in the microstructure.

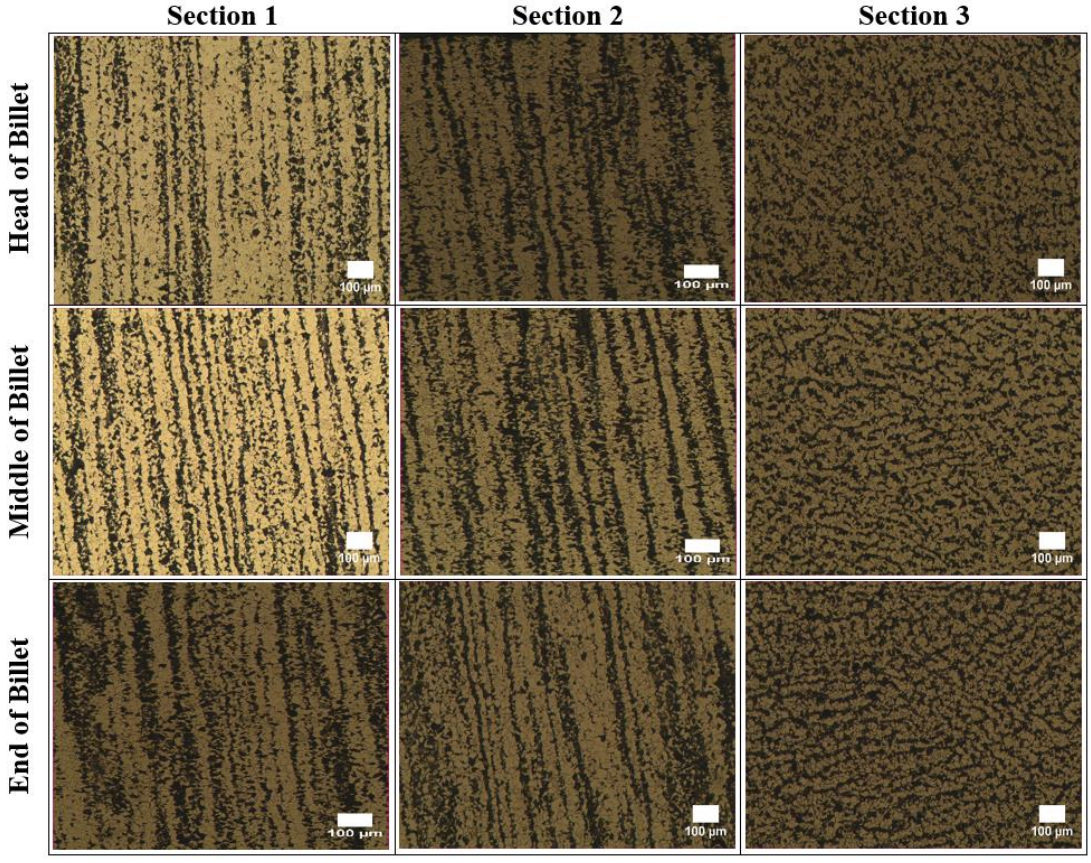

Figure 16. Optical micrographs taken at 50x magnification via optical microscope from the head, middle and end sections of the billet

Higher magnification micrographs reveal the details of the bands, which are composed of ferrite and pearlite, as shown in Figure 17. Ferrite appears light, pearlite appears dark (by aligning the cementite lamellar on the ferrite matrix) and the lamellar structure does not appear clearly because of the small interlamellar distance of pearlite and the resolution limit of the optical microscope. Since the structure consists of two distinctive regions which are ferrite and pearlite, quantitative (numerical) metallography measurements were performed on both of those regions separately.

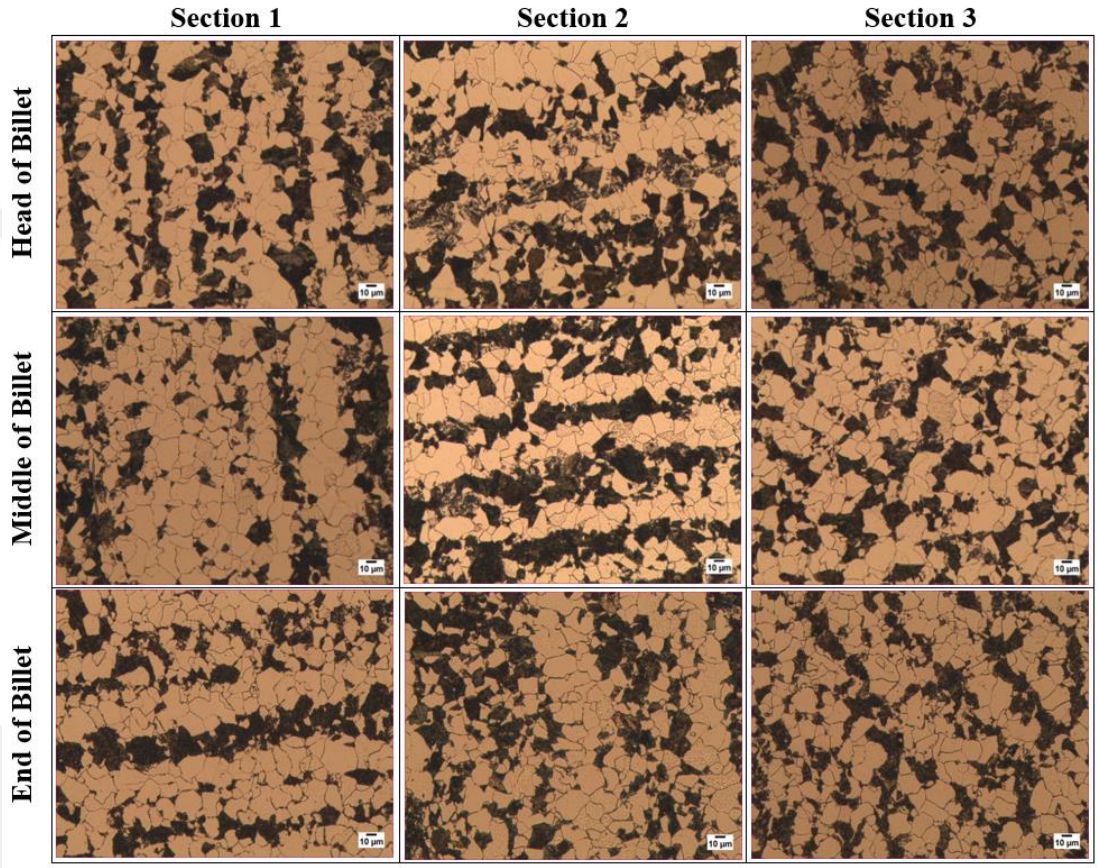

Figure 17. Optical micrographs taken at 200x magnification via optical microscope from the head, middle and end sections of the billet

3.3.1. Determination of Ferrite and Pearlite Percentage and Grain Size

Quantitative analyzes were performed on the photographs using ImageJ® [39] and Clemex Vision PE software solutions. The grain size and percentage of phase for the ferrite and perlite were calculated on the optical micrographs taken at 200x. Thresholding [40] was applied on the "histogram" to separate ferrite and pearlite from

the structure. Figure 18 shows the histogram of a typical ferrite-pearlite microstructure. Ferrite and pearlite form two distinct peaks; therefore using a threshold value between those peaks will enable us to distinguish those microstructural constituents.

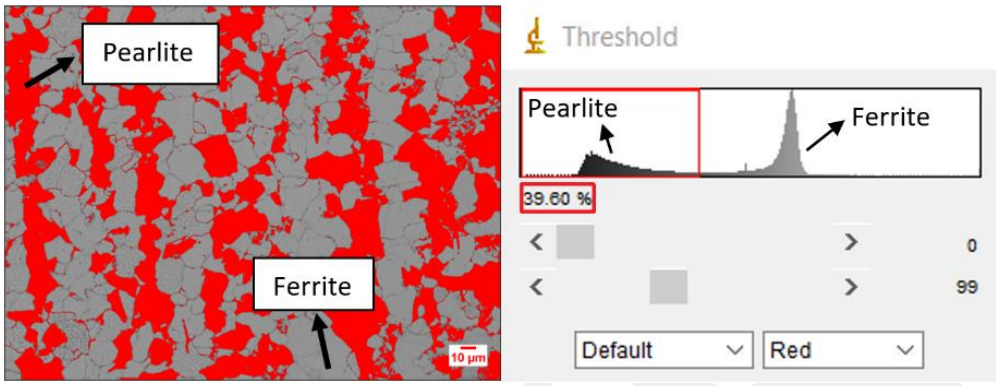

Figure 18. Histogram of ferritic and pearlitic microstructures

Ferrite and pearlite fractions are calculated via ImageJ® software for 5 different microstructure images taken from 3 different sections for head, middle, end of billet. When the general average of the fractions of ferrite and pearlite of the head, middle, end of billet is taken, it is found that there are 62 ± 5 percent ferrite and 38 ± 5 percent pearlite microstructures along the billet. Subsequently, ferrite and pearlite grains were separated using the "watershed" segmentation algorithm [41]. Then, the size (in terms of μm and ASTM G-number), roundness, aspect ratio, and angle of the grains were calculated. For calculating those values each delinated grain shape was defined by an ellipse. The shape of the ellipse is defined by two basic axes as known major and minor axis which are the primary and secondary axis of the best fitting ellipse. The aspect ratio, circularity, angle and grain size of ferrite and pearlite are determined according to calculation in Table 5 for each of the three sections (i.e. the head, middle and end of the billet). Grain size measurements were performed in accordance with the ASTM E112-13 standard [42]. The measurement results are given in Table 6 and the mean values of the circularity and aspect ratio of less than 1 and the angle value of less than 100 indicate that the ferrite and pearlite grains are in an elongated structure as shown in Figure 16. Ferrite and pearlite grain size distributions of the head, middle, end of the billet for section 1 which are parallel to the rolling direction are represented in Figure 19.

Table 5. Calculations and definitions of aspect ratio, circularity, angle and grain size

Aspect Ratio:	[Minor Axis] / [Major Axis]
Circularity:	$4\pi \times \frac{[\text{Area}]}{[Perimeter]^2}$ (Value 1 for the circle, 0 for an infinitely extending bar)
Angle:	The angle between the X-axis of the image and the major axis of the fitted ellipse
Grain size:	$G = -2.9542 + (3.3219log10 \times NA)$ NA is the number of grains per square millimeter at 1x magnification and G is the grain size (ASTM).

Table 6. The mean values of the analyzes made for each of the 3 sections for the head, middle, end of the billet

			Grain Size (Micron)	Grain Size (ASTM)	Aspect Ratio	Angle	Circularity
Head of Billet	Ferrite	Section 1	13.6	10.1	0.67	92.95	0.64
		Section 2	15.6	9.4	0.66	88.57	0.61
		Section 3	13.2	9.9	0.65	86.70	0.61
	Pearlite	Section 1	14.3	10.2	0.66	87.17	0.68
		Section 2	13.0	10.1	0.66	90.46	0.69
		Section 3	11.9	10.2	0.66	104.71	0.69
Middle of Billet	Ferrite	Section 1	13.7	10.1	0.63	92.07	0.63
		Section 2	12.6	10.6	0.62	89.70	0.61
		Section 3	13.7	10.1	0.65	89.65	0.63
	Pearlite	Section 1	12.9	10.0	0.65	94.02	0.66
		Section 2	12.1	10.3	0.62	89.96	0.67
		Section 3	11.3	10.7	0.66	90.14	0.69
End of Billet	Ferrite	Section 1	15.0	9.7	0.64	93.76	0.63
		Section 2	12.4	10.5	0.64	88.94	0.64
		Section 3	12.6	10.1	0.68	82.72	0.64
	Pearlite	Section 1	11.7	10.6	0.64	89.29	0.68
		Section 2	14.5	9.9	0.65	87.54	0.65
		Section 3	11.5	10.3	0.66	94.98	0.68
Average of Billet	Ferrite		13.6 ± 1.08	10.1 ±0.37	0.65 ± 0.017	89.45 ±3.384	0.63 ±0.012
	Pearlite		12.6 ±1.18	10.3 ±0.26	0.65 ±0.014	92.03 ±5.421	0.68 ±0.015

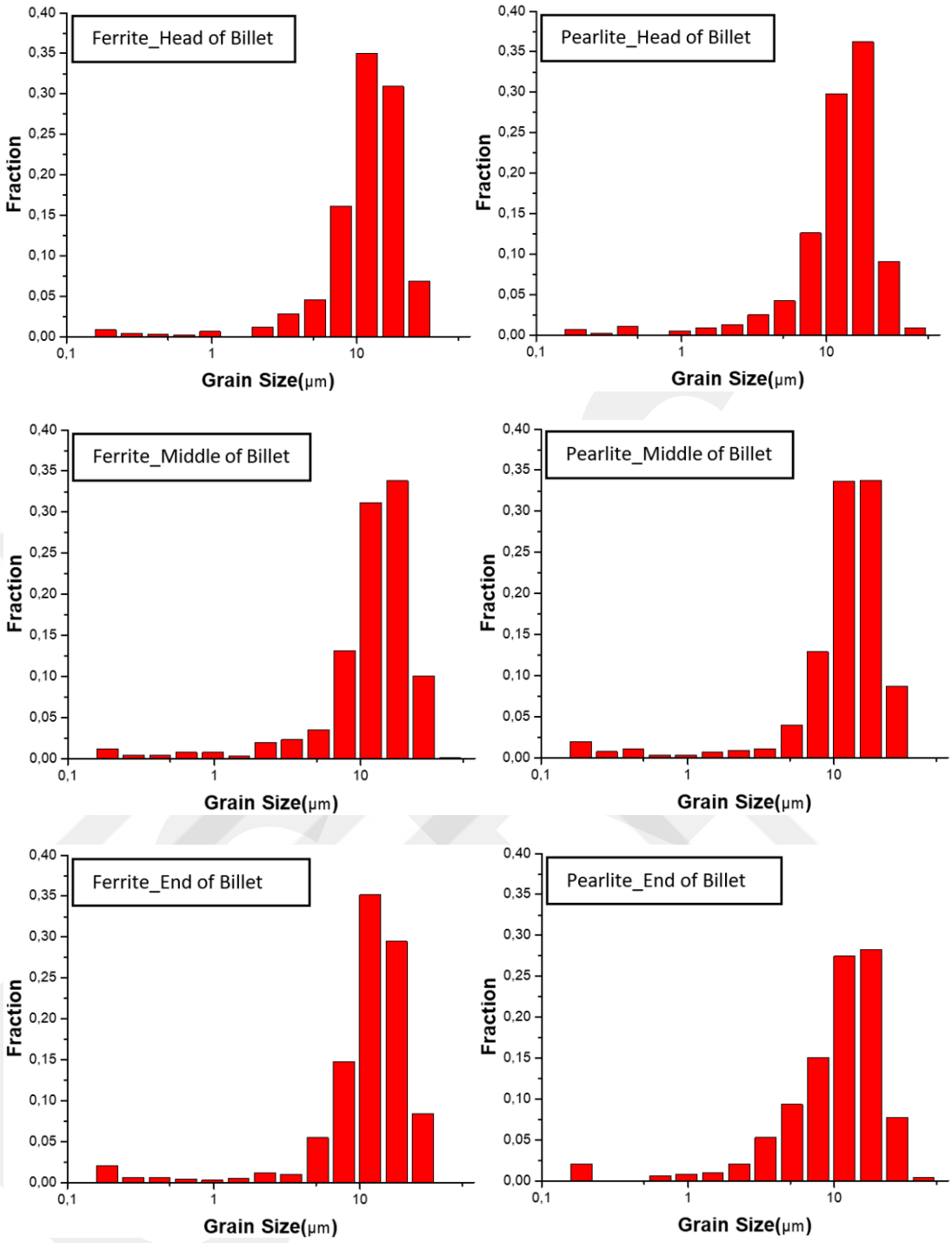

Figure 19. Ferrite and perlite grain size distributions of the head, middle, end of the billet for section 1

3.3.2. Degree of Banding

Segregation occurs during dendritic solidification of metal alloys also it can be explained as the separation of the liquid during solidification into regions with different element compositions. It is also called primary decomposition at the same time. This is because the alloying elements have different resolutions in liquid and solid. This concentration difference during solidification also affects ferrite and cementite transformation from the subsequent austenite. During the hot rolling followed by the primary deformation, the dissociated zones extend along the direction of deformation. Mn contents higher than 1 wt. % is considered to be highly susceptible to segregation also affects the temperature ranges in which ferrite and austenite are stable [43]. As a result, as shown in Figure 20, Figure 21 and Figure 22, the ferrite and pearlite zones in the hot-rolled cemented steels are segregated and extended in the rolling direction. This structure is also called "banded" structure.

The banded structure causes the anisotropy and also the mechanical properties in the width direction to be weakened. It can also affect the machinability and hardenability of the material. In order to prevent or reduce the banding, it is first necessary to avoid separation during solidification. But it is almost impossible to apply it on an industrial scale. However, the banding can be reduced by careful adjustment of hot rolling temperature, hot and cold rolling grade, ferrite and austenite stabilizing element compositions, and by using diffusion annealing and accelerated cooling practices. So the ASTM E1268 standard has been developed to determine the degree of banding [44]. The standard makes a rating index based on the principle that the elements of the banded structure in the vertical and horizontal ways in the direction of deformation are counted and proportion to each other. The symbols in the calculations and formulas made according to the standard are explained in Table 7.

Samples from the head, middle, and end of the billet produced from the DIN 22NiCrMo2-2 steel were taken for the calculation of the banding degree. And samples were prepared for metallographic examination with the help of procedures specified in ASTM E3-11 standard [36]. The samples were taken from sections parallel to the direction of the rolling. Since banding and orientation were best observed at magnifications below 200x, the bands were photographed at 50x magnification in an optical microscope, with light field illumination, aligned to extend along the rolling

direction of horizontal axial. Micrographs taken from at least 5 different regions chosen randomly for each part of the billet. The micrographs were evaluated with the help of Clemex Vision PE software and the formulas shown in Table 7, and the banding degree was determined by the parameters "anisotropy index (AI)" and "orientation grade (Ω_{12})". The AI value is 1 for a randomly oriented and non-tagging microstructure. As the degree of orientation increases and the bandgap increases, the AI value will be greater than 1. The orientation grade (Ω_{12}) will likewise be 0 for a completely random distribution and 1.0 for a fully directed structure.

Table 7. Parameters and formulas used to determine the banding degree

Symbol	Explanation	Formula
$N_{\perp}$	Number of feature interceptions with test lines perpendicular to the deformation direction	$N_{L\perp} = {}^{N_{\perp}}/_{L_t}$
$N_{\parallel}$	Number of feature interceptions with test lines parallel to the deformation direction.	$\bar{N}_{L\parallel} = {}^{N_{\parallel}}/_{L_t}$
L_t	True test line length in mm, that is, the test line length divided by *m*agnification	
$P_{\perp}$	Number of feature boundary intersections with test lines perpendicular to the deformation direction	$\bar{P}_{L\perp} = {}^{P_{\perp}}/_{L_t}$
$P_{\parallel}$	Number of feature boundary intersections with test lines parallel to the deformation direction	$\bar{P}_{L\parallel} = {}^{P_{\parallel}}/_{L_t}$
n	Number of measurement fields or number of micro indentation impressions	
$\bar{X}$	Mean values ($\bar{n}_{L\perp}, \bar{N}_{L\parallel}, \bar{P}_{L\perp}, \bar{P}_{L\parallel}$)	$\bar{N}_{L\perp} = {}^{\sum N_{L\perp}}/_{n}$
S	Estimate of standard deviation	
95 % CI	%95 confidence interval.	$\pm {}^{ts}/_{\sqrt{n}}$
% RA	% Relative accuracy	${}^{95\%\ CI}/_{\bar{X}} * 100$
$SB_{\perp}$	Mean center-to-center spacing of the bands	${}^{1}/_{\bar{N}_{L\perp}}$
V_V	Volume fraction of the banded phase (constituent)	V_V
$\lambda_{\perp}$	Mean edge-to-edge spacing of the bands, (mean free path / distance).	${}^{1 - V_V}/_{\bar{N}_{L\perp}}$
AI	Anisotropy index	$\frac{\bar{N}_{L\perp}}{\bar{N}_{L\parallel}} = \frac{\bar{P}_{L\perp}}{P_{L\parallel}}$
Ω_{12}	Degree of orientation of partially oriented linear structure elements on the two-dimensional plane-of-polish.	$\frac{\bar{N}_{L\perp} - \bar{N}_{L\parallel}}{\bar{N}_{L\perp} + 0.571\bar{N}_{L\parallel}}$

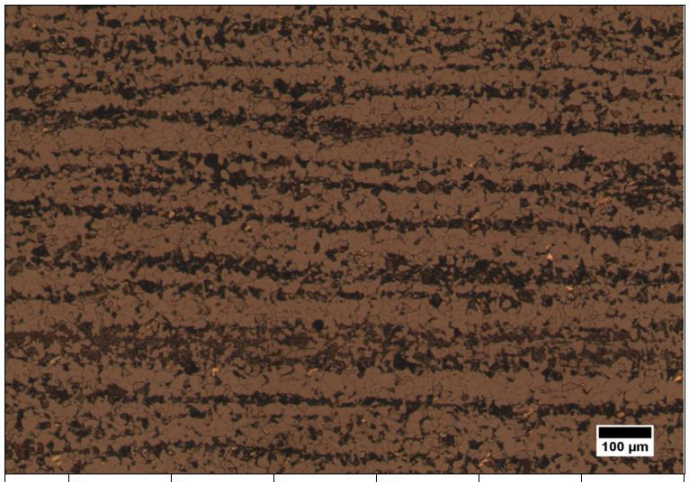

	$\bar{N}_{L\perp}$ (No./mm)	$\bar{N}_{L\parallel}$ (No./mm)	$\bar{P}_{L\perp}$ (No./mm)	$\bar{P}_{L\parallel}$ (No./mm)	AI	Ω_{12}
$\bar{X}$	18.06	21.34	36.14	42.66	1.18	0.103
s	0.986	0.796	1.943	1.540		
%95 CI	± 1.22	± 0.99	± 2.41	± 1.91		
RA %	6.8	4.6	6.7	4.5		
n	5					
	V_V = 39.2 % ± 4.2		$SB_\perp$ = 46.9 µm ± 1.7		$\lambda_\perp$ = 28.6 µm ± 2.8	

Figure 20. Microstructure of the head section of the billet shown at 50x magnification, the results of banding degree analysis (grading were made for pearlite with dark color)

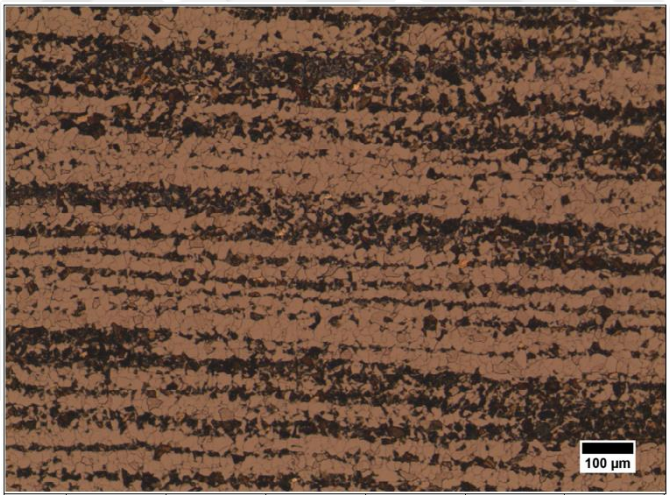

	$\bar{N}_{L\perp}$ (No./mm)	$\bar{N}_{L\parallel}$ (No./mm)	$\bar{P}_{L\perp}$ (No./mm)	$\bar{P}_{L\parallel}$ (No./mm)	AI	Ω_{12}
$\bar{X}$	15.06	18.74	30.20	36.04	1.24	0.133
s	0.723	0.541	1.449	3.114		
%95 CI	± 0.90	± 0.67	± 1.80	± 3.87		
RA %	5.96	3.6	5.95	10.7		
n	5					
	V_V = 40.4 % ± 4.1		$SB_\perp$ = 53.4 µm ± 1.5		$\lambda_\perp$ = 31.9 µm ± 2.8	

Figure 21. Microstructure of the middle section of the billet shown at 50x magnification, the results of banding degree analysis (grading were made for pearlite with dark color)

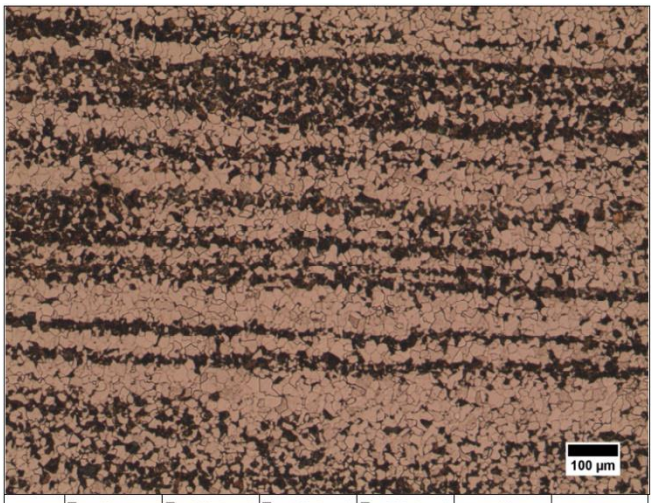

	$\bar{N}_{L\perp}$ (No./mm)	$\bar{N}_{L\parallel}$ (No./mm)	$\bar{P}_{L\perp}$ (No./mm)	$\bar{P}_{L\parallel}$ (No./mm)	AI	Ω_{ZZ}
$\bar{X}$	17.8	20.18	35.58	40.38	1.14	0.082
s	0.655	0.349	1.308	0.729		
%95 CI	± 0.81	± 0.43	± 1.62	± 0.91		
RA %	4.6	2.1	4.6	2.2		
n	5					
	V_V = 49.8 % ± 5.0		$SB_\perp$ = 49.5 µm ± 0.9		$\lambda_\perp$ = 24.8 µm ± 2.3	

Figure 22. Microstructure of the end section of the billet shown at 50x magnification, the results of banding degree analysis (grading were made for pearlite with dark color)

3.3.3. Micro Segregation Analysis

In the previous section 3.3.2, it has been shown that the DIN 22NiCrMo2-2 steel shows a banded structure. Figure 23 shows the SEM micrograph of the banded structure, taken with secondary electron detector.

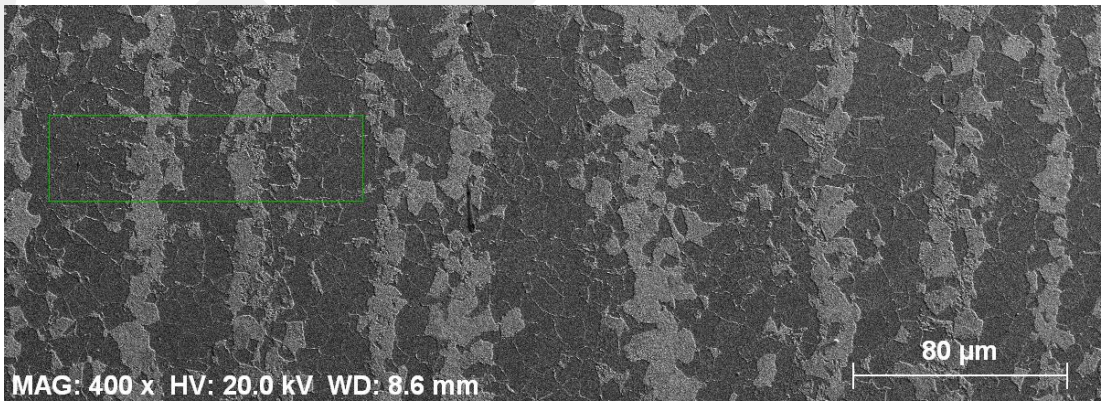

Figure 23. SEM micrograph of the banded structure of 22NiCrMo2-2 steel. The rectangle indicates the area, at which elemental mapping (via EDS) is performed.

The banded structures are composed of ferrite and perlite regions elongated along the rolling direction. Moreover, those bands can also be dissimilar along the rolling direction. The mechanism which is causing the formation of banded structures is the formation of micro-segregation during solidification.

Microsegregation can be defined as the composition differences between the initial solids and the subsequent solids, since there is not enough time to complete the diffusion in the formed solids in nonequilibrium solidification. Typical cooling rates which are achieved in steel production are too rapid to allow the diffusion in the solids. For this reason, compositional differences occur between the first solidified regions and the last solidified regions. This composition is called micro-segregation because these compositional differences are in average grain size. During rolling processes which are applied to a microsegregated steel, the zones with different chemical composition extend along the rolling direction. When a hot rolled steel in the austenitic zone is cooled to room temperature, the austenite transform into ferrite and pearlite.

Inhomogeneous distribution of the austenite stabilizing elements such as Mn (micro-segregation) also affects austenite transformation. The areas where the austenite stabilizing elements are intense are later transformed. Particularly in medium and low carbon steels, firstly ferrite forms in region where there are few austenite stabilizing elements and the remaining regions become completely pearlite afterwards. In summary, the main reason for the formation of ferrite-pearlite bands is microsegregation of elements such as Mn during solidification. Micro-segregation is a phenomenon in which alloying elements are not homogeneously distributed in the structure after solidification and subsequent rolling. In order to be able to detect this, it is necessary to find the distributions of these elements in micro-level (average grain size and lower level) in the structure. In order to find out this distribution, an energy dispersive X-ray spectrometer (EDS), which is connected to the scanning electron microscope (SEM), was used. This system can quantitatively determine the elemental composition along a line (linear analysis) or can perform area analysis (mapping). Figure 24 shows the results of EDS-mapping and Figure 25 the linear EDS results.

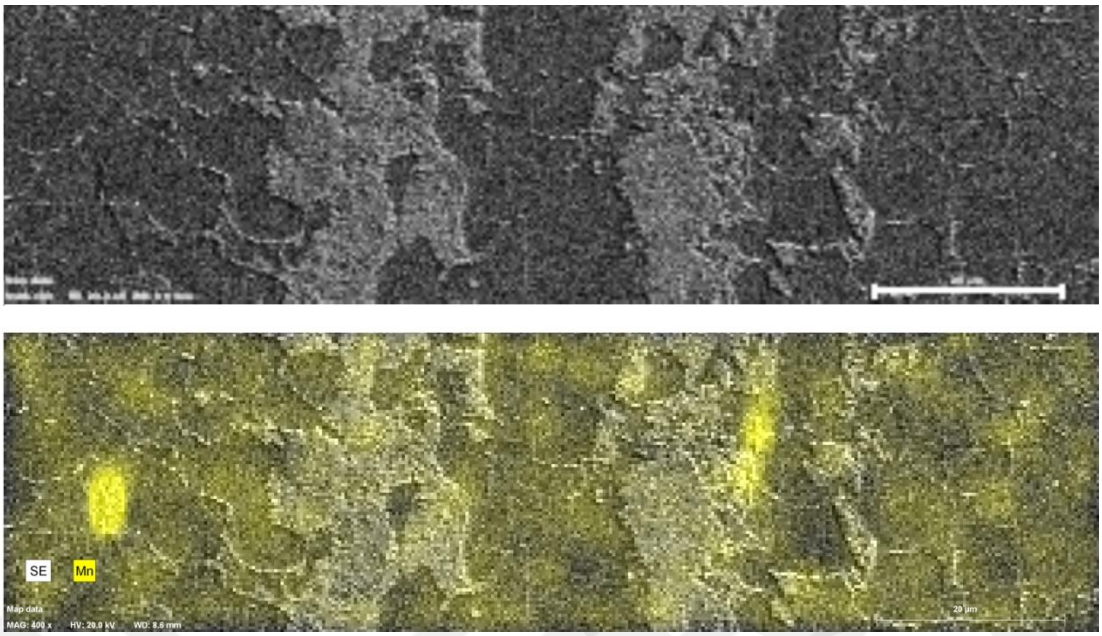

Figure 24. The results of the EDS mapping performed on the area shown in Figure 23 for the 22NiCrMo2-2 steel. The secondary electron micrograph (top) of the region analyzed, and the distribution of Mn (bottom) is given.

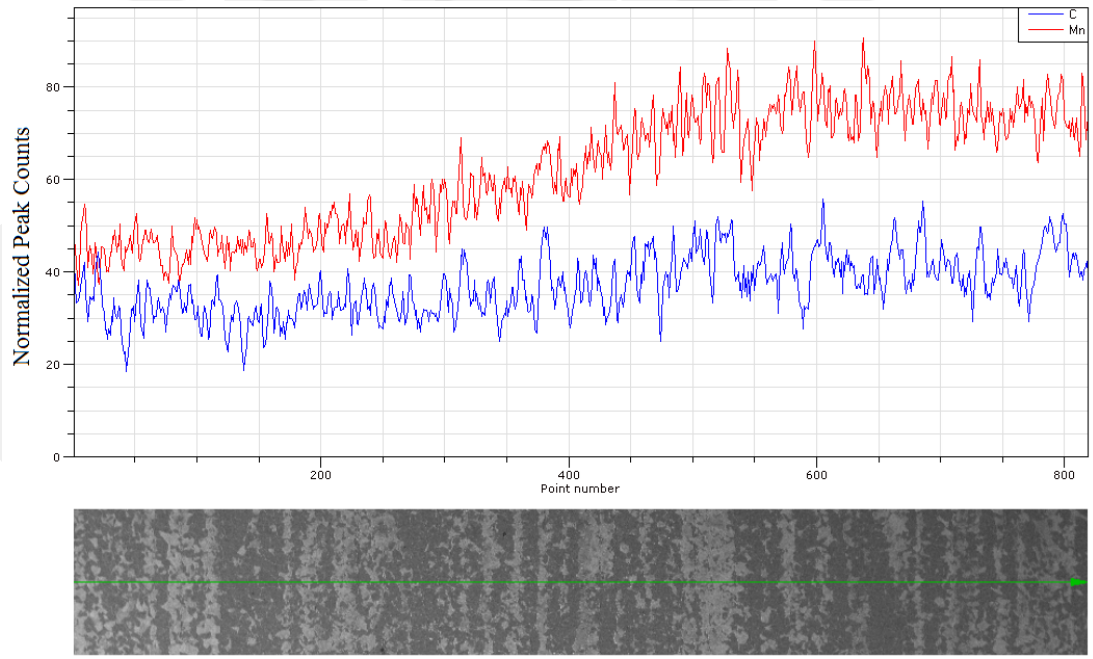

Figure 25. Linear EDS analyzes made on the banded structure for DIN 22NiCrMo2-2 steel, C and Mn distributions (top), secondary electron image of the region where the linear analysis is performed (below).

The results clearly show in Figure 25 that there is difference between the bands in terms of the C and Mn elements. SEM images showed higher C in the pearlite regions that appeared light in color, and higher Mn in regions where the bands start. The results are consistent with the prescribed mechanism in the literature [45], [46].

3.4. DIN 22NiCrMo2-2 (SAE 8620H) Equilibrium Phase Diagram

The carburizing process involves holding the steel at the austenitic region for longer durations (> 12 hours). Therefore, this part of the carburized-quenching process can be considered to be performed at near-equilibrium conditions. Equilibrium phase diagrams indicate the composition of the phases and also the transformation temperatures. In this regard, the equilibrium phase diagram of DIN 22NiCrMo2-2 steel is essential for the process design of carburizing heat treatment.

CALPHAD (Calculation of Phase Diagram) methods calculate phase equilibria in the complex multicomponent alloys that are used regularly by industry [47]. The phase diagram for the DIN 22NiCrMo2-2 steel, calculated using the CALPHAD method in the Thermocalc® software, is given in Figure 26. With this diagram it is understood that the 1.1% C composition in the carburizing process will be the limit because it is possible that pre-eutectoid cementite precipitation can occur on grain boundaries over this composition. Pre-eutectoid cementite precipitated at the grain boundaries affects the workability and toughness of the material in the negative direction and leads to grain brittleness [10]. For this reason, it has been decided that the carbon potential of the carburizing process should not exceed this value. It was also found that the eutectoid composition came to 0.6 wt.% C composition instead of 0.8 wt.% C due to alloy elements. Therefore, it is decided that the maximum carbon ratio should be 0.6 wt.% in the step where reduce the amount of carbon before quenching.

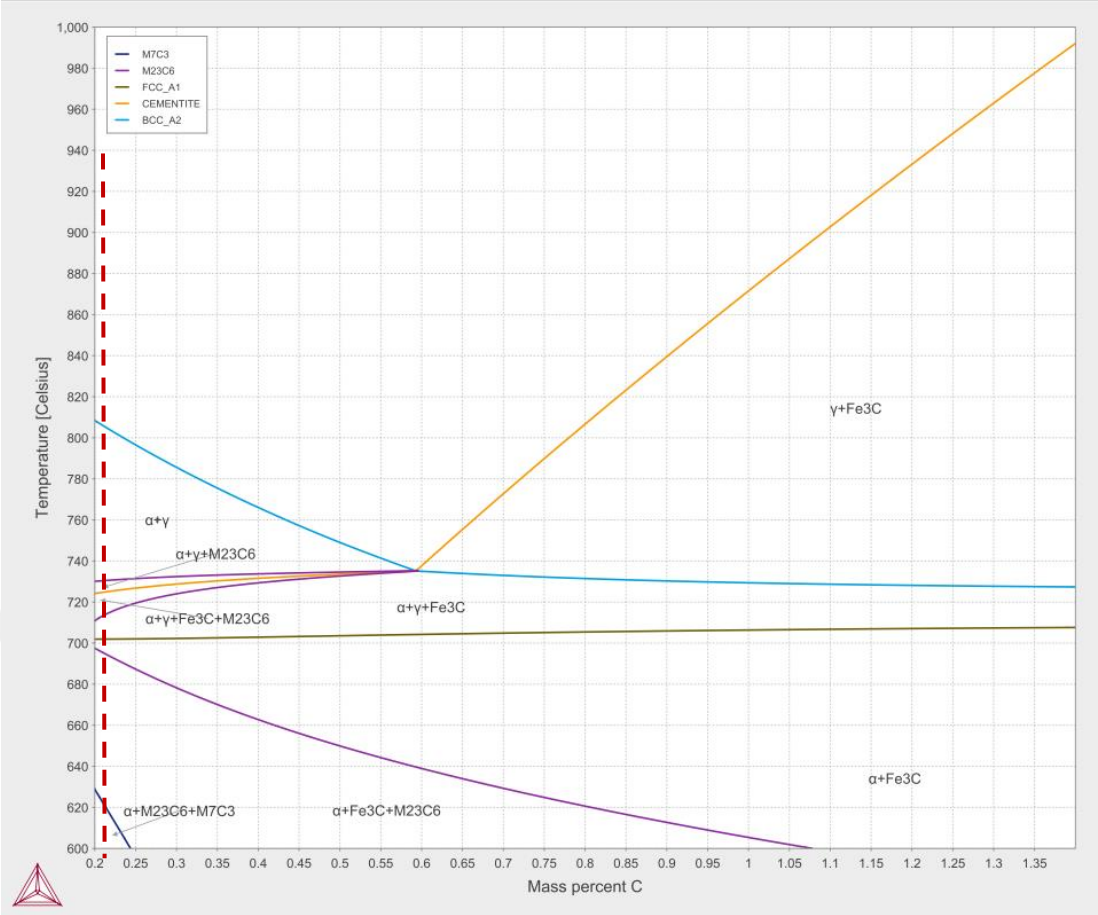

Figure 26. %Carbon isopleth of DIN 22NiCrMo2-2 steel calculated with the Thermocalc® software, dashed line indicate the carbon percent of DIN 22NiCrMo2-2 initial composition.

3.5. Discussions

In this chapter, the results of macro and microstructural characterization of the DIN 22NiCrMo2-2 steel has been shown. The amount of alloying elements in the chemical composition of the DIN 22NiCrMo2-2 steel was determined with macro chemical analysis, which is the first and an important step of material characterization. It has been found that DIN 22NiCrMo2-2 steel has C, Mn, Cr, Si, Ni and Mo elements which affect microstructure and phase transformation. As a result of the chemical and macro segregation analysis, it has been determined that the DIN 22NiCrMo2-2 steel has homogeneous structure and not having significant macro-segregation. It is seen that the alloying elements in the chemical composition, especially Mn, create micro-segregation and banded microstructure. Chemical and microstructural heterogeneity

as well as banded microstructures are known to affect the heat treatment response. Chemical segregation significantly influence phase-transformation behavior during heat treatment. Therefore alloying elements segregation affect the hardenability [48]. Also the banding microstructure which occur because of the microsegregation and results the anisotropic extension cause the distortion after heat treatment [7], [49]. For that reason, microsegregation and banded structure have been studied. The anisotropy index (AI) was calculated as 1.19 on the samples taken from the head, middle, and end of the billet of the DIN 22NiCrMo2-2. As it is seen in Figure 20 -Figure 22, it is understood that the effect of banding degree in the DIN 22NiCrMo2-2 microstructure is not very high according to ASTM E1268 [44].

The microstructure of the DIN 22NiCrMo2-2 steel consist of ferrite and perlite as can be seen in Figure 16 and Figure 17, and the size, angle, aspect ratio and circularity of the ferrite and perlite grains were investigated. When the mean values in Table 6 are compared with the standard deviation values, it is seen that the standard deviation values are under 10% of the average values. This indicates that there is a homogeneous distribution along the billet, and the graphs in Figure 19 also show this. Besides the initial grain size of the DIN 22NiCrMo2-2 steel was determined as 10.2 ± 0.31 ASTM.

In the literature investigations, it is seen that the phase proportion in the initial microstructure affect the mechanical properties of the material. The diffusion distance between the cementite and the ferrite lamellar in the pearlite structure is shorter than the diffusion distance of the equiaxed ferrite grains. For this reason, austenite transformation of perlite is faster than ferrite. So, the fraction of ferrite and perlite in the microstructure of the raw material has a large effect on the volume change in the austenitic line, thus can affect the distortion in a hardened part [29]. As a result of the comparison of this study with literature, it has been determined that the fraction of pearlite and ferrite phase in the initial microstructure of the DIN 22NiCrMo2-2 steel is not as effective as to cause distortion.

Furthermore, prior to carburizing heat treatment, the phase diagram of the DIN 22NiCrMo2-2 steel was calculated for the determination of secondary phases that may occur in the material and the maximum amount of carbon that may be present in the chemical composition were found as 1.1 wt. %.

When the macro and micro structure of the DIN 22NiCrMo2-2 were examined with the characterization studies, the preliminary information was obtained for the experimental and simulation studies also it was concluded that the material was suitable for the carburizing process. After the characterization of the raw material, the austenite grain growth kinetics, which is known to have an effect on the material properties, was investigated in order to be entered as an input data to the heat treatment simulation and calculation of CCT, TTT diagrams.

CHAPTER 4

DETERMINATION OF AUSTENITE GRAIN GROWTH KINETICS

4.1. Introduction

Carburizing treatments involve longer holding time at higher temperatures (i.e. in the austenite region), which can produce a range of different prior-austenite grain sizes (PAGS) depending on the growth behavior. Moreover, the presence of inter-metallics and carbides can pin-down the grain growth of prior austenite. This pinning effect on austenite grain growth was studied in micro-alloyed steels [50], [51]. The PAGS of any steel has a considerable influence on hardenability, kinetics of phase transformations, final phase fraction and hence on final mechanical properties [52], [53].

Since the high-temperature austenite structure is transformed during subsequent cooling steps, controlling the formation of desired austenitic structure during carburizing treatment is difficult and particularly important. The objective of this chapter is to predict the PAGS of DIN 22NiCrMo2-2 steel during carburizing treatment by determining the parameters of the ideal grain growth model from the results of metallographic examinations. The input parameters of the model will only be the austenitization time and temperature which are the most important heat treatment variables that determine the austenite grain structure. This physically based model could then be used in heat-treatment simulation of carburized quenching for further process development and optimization.

4.2. Experimental Procedure

DIN 22NiCrMo2-2 steel samples whose composition is given in Table 4 was used to determine the growth kinetics of austenite grains. The exact geometry of the samples is given in Figure 27 also the section indicated by number 1 indicates the section, from which metallographic analyses were performed.

In order to produce a range of various different prior austenite grain sizes the specimens were heated to 3 different temperatures, (850, 900, 925°C) at a rate of 1°C/s followed by isothermal holding for 3 different durations (15 min., 8 hour, 24 hour), and lastly quenching to room temperature at the rate of 350°C/s to ensure transformation to martensite. Those heat treatment cycles for all 9 specimens were conducted using Gleeble®–3800 thermo-mechanical simulator.

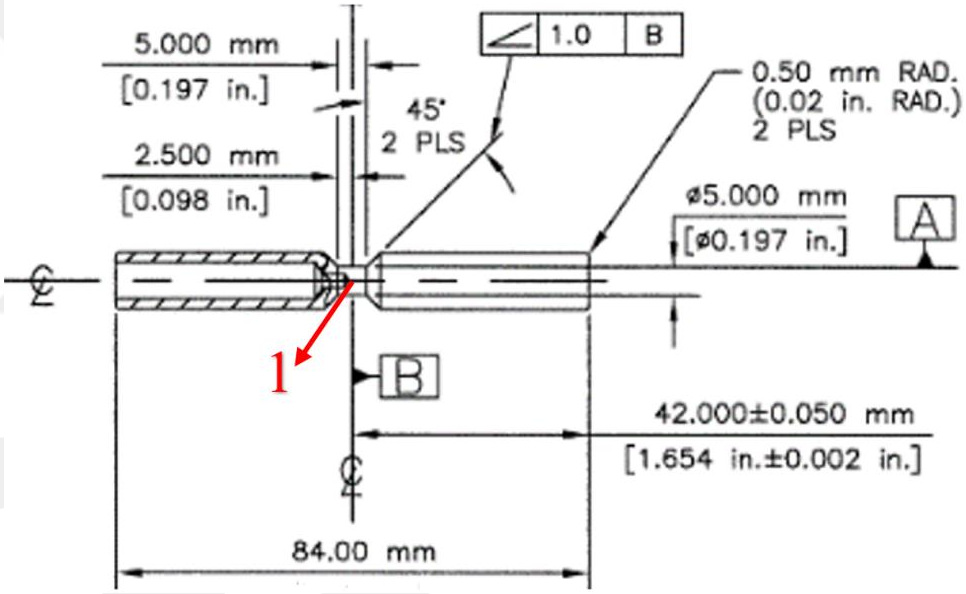

Figure 27. Geometry of the samples which were used to determine prior austenite grain size.

The prior austenite grain size of the heat-treated specimens was determined via metallographic examination. Metallographic specimen preparation started by mechanical grinding using SiC grinding papers followed by mechanical polishing using 9, 3 and 1 µm diamond paste followed by 0.05 µm-diameter colloidal silica particles. The most common etchants used to reveal the prior austenite grains are listed in Table 8. For the present DIN 22NiCrMo2-2 steel, the prior austenite grains were

revealed most clearly via Krahe and Desnoues's etch which is indicated in Table 8. The polished specimens were etched for 10-15 seconds by dipping them into the etching solution kept at 80°C. Micrographs of the specimens were taken by Nikon LV150N optical microscope, using bright field illumination. Prior austenite grain size was measured by Heyn Intercept method in accordance with the ASTM E112 standard [42]. The length of the intercepts used were 180 mm horizontally and 130 mm vertically. Grain boundary and intercept intersections were counted on 5 randomly selected fields per specimen. This measurement grid produced 50 to 150 intersections per micrograph, thus ensuring accuracy of the measurements.

Table 8. Prior-austenite grain size etchants

Vilella's etch.[54]	100 mL ethanol, 1 g picric acid, 5 mL HC1
Schrader's modification of Vilella's etch[55]	80 mL ethanol, 1 g picric acid, 10 mL HC1,10 mL HNO3
Bechet and Beaujard's etch [56]	Sat. aq. picric acid plus small amount of a wetting agent
Krahe and Desnoues's etch[57]	10 g picric acid, 20 drops HC1, 20 drops Teepol (wetting agent), 1000 mL water
Popova and Malashenko's etch [55]	34 g sodium bisulfite, 100 mL water

4.3. Results of Grain Growth Kinetic Analysis

Figure 28 shows optical micrographs of all specimens, in a tabulated manner with respect to austenitization time and temperature. The etchant does not react uniformly with the specimen surface, which can be identified from the burnt dark areas on some minor regions. Some specimens are non-uniformly etched, the dark regions are over-etched. However, the prior austenite grain structures are revealed clearly in all specimens. The figure shows that the PAGS increase as austenitization temperature

(T_γ) or time increases. As expected, the austenitization temperature, T_γ, influences the coarsening of the prior austenite structure much more effective than the austenitization time.

Figure 29 shows the change of average PAGS value, which has been calculated for each specimen from the optical micrographs, as a function of T_γ. The figure also shows the PAGS findings of a reference study, namely the study of E.Khzouz's [23] for comparison. The comparison chemical composition of the steel used in this reference study and DIN 22NiCrMo2-2 steel is tabulated in Table 9 as well. The change in PAGS values, specifically in the 900°C – 925°C range is very small, in fact smaller than the standard deviation in the measurements. For the reference study, the austenitization time does not influence the PAGS value at T_γ= 850°C. On the other hand, the PAGS values show exponential growth, most clearly observed for the samples austenitized for 9 h, in the reference study of E. Khzouz [23].

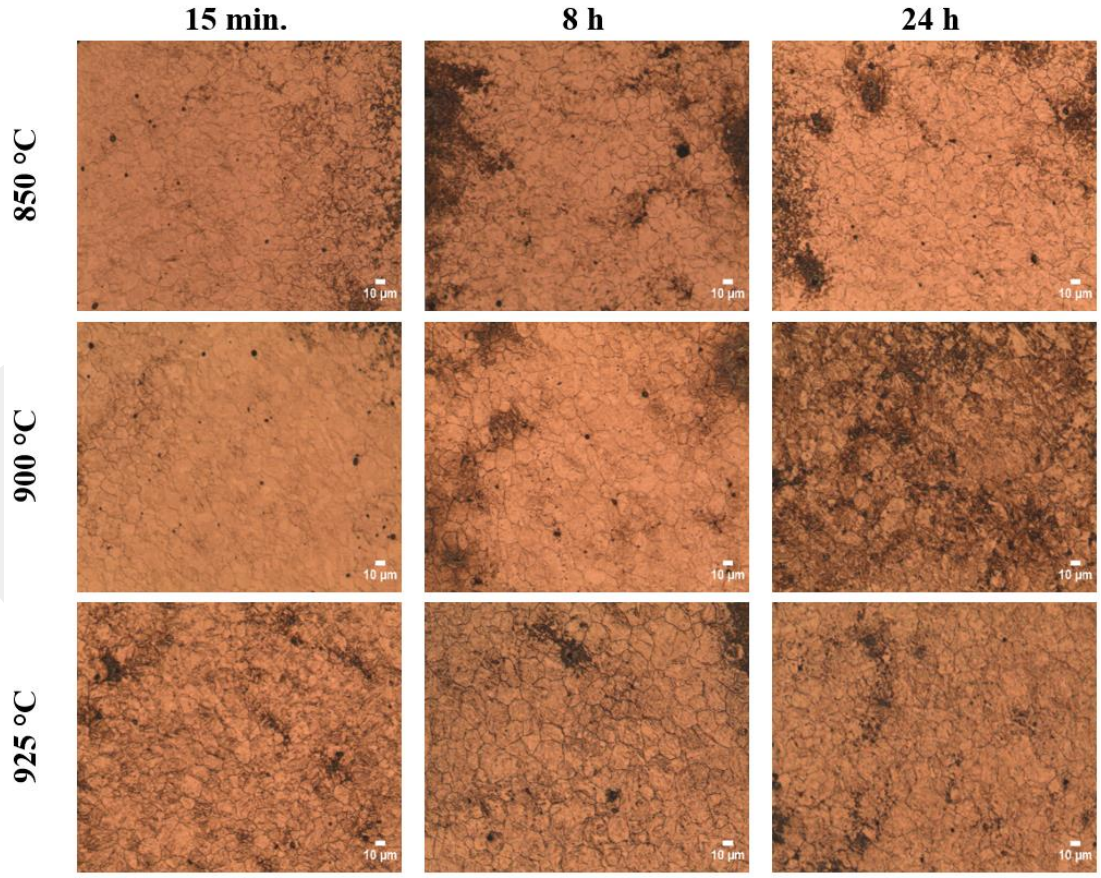

Figure 28. Optical micrographs of the specimens taken at 200x under bright field illumination.

Table 9. The comparison chemical composition (wt. %) of this study and E.Khzouz's study

DIN 22NiCrMo2-2	Fe	C	Cr	Mn	Mo	Ni	P	S	Si
Present Study	Bal.	0.21	0.56	0.84	0.24	0.53	0.005	0.02	0.33
E.Khzouz's Study[5]	Bal.	0.21	0.56	0.81	0.15	0.45	0.006	0.01	0.24

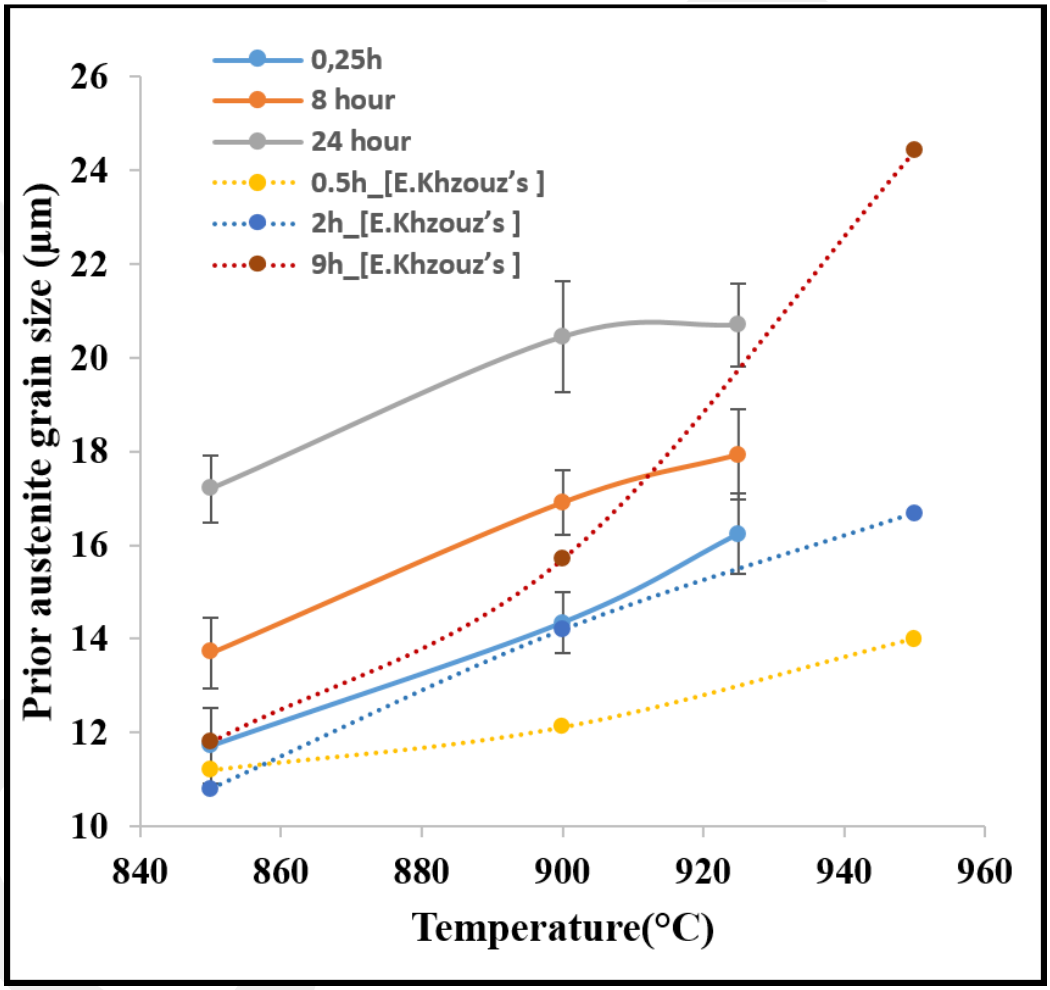

Figure 29. The PAGS values of the current study, compared to the reference study of E.Khzouz's; plotted as a function of austenization temperature

Table 10. Average grain size values (AGS) and the standard deviation of AGS determined from metallographic examination of samples austenitized at different temperature and time combinations.

T (°C)	Time (hr)	AGS (μm)	AGS(ASTM-G)
850	0.25	11.7 ± 0.8	9.9 ± 0.2
	8	13.7 ± 0.7	9.4 ± 0.2
	24	17.2 ± 0.7	8.8 ± 0.1
900	0.25	14.4 ± 0.6	9.3 ± 0.1
	8	16.9 ± 0.7	8.8 ± 0.1
	24	20.4 ± 1.2	8.3 ± 0.2
925	0.25	16.2 ± 0.9	8.9 ± 0.2
	8	17.9 ± 0.9	8.7 ± 0.2
	24	20.7 ± 0.9	8.2 ± 0.1

The PAGS values of the present study, which are obtained from the prescribed quantitative metallographic study, are tabulated in Table 10. Note that the standard deviation values are small, in fact the relative accuracy for all the measurements are well below 10%. This indicates the higher precision in PAGS measurements, in accordance with the ASTM E-112 standard [42]. Those experimentally determined PAGS values are then used to construct a physically based grain growth model.

The grain growth in crystalline materials can be explained by the "General Grain Growth Law", which is shown in Eq. 13. Experimentally determined m values, which is described in Eq. 1, are in the range of 2 to 5. In a pure system which has no defects or precipitates to pin the growth of a grain, m is 2 [58], [59]. Since the optical micrographs does not show potential pinning sites, the m value was taken as 2.

$$D^2 - D_o^2 = Kt \qquad \text{Eq. 13}$$

Grain growth is a thermally activated, temperature dependent process, therefore the relationship between K and temperature can be represented by the following Arrhenius formula [21], [58]:

$$K = K_o \exp(-Q/RT) \quad \text{Eq. 14}$$

where K_0 is the pre-exponential term, Q is the activation energy for grain growth, R is the gas constant and T is the temperature (in Kelvin).

Linear regression analysis was performed using Eq. 13 and the experimental data tabulated in Table 10. Also in Figure 30, K and D_o values for 850ºC, 900ºC and 925ºC were calculated using linear least squares method from trendline of grain size and effective times. K values were calculated from slope of trendline and D_o values were calculated from intercept of trendline, and also the values were represented in Table 11. Besides, the calculated K and D_o values of the current study compared to reference study [23] in Figure 32. The results indicated that the D_o values agree quite well, whereas K value of the current study is considerably low for 850ºC, about an order of magnitude. In addition, same least squares method was performed in Figure 31 using the Eq. 14 and the K values tabulated in Table 11. K_o and Q values are represented in Table 12.

Table 11. K and D_o values, which are calculated using Eq 13 and the data tabulated at Table 10

DIN 22NiCrMo2-2		
Temperature (°C)	**K (mm²/min)**	**D_o (mm)**
850	1.09E-07	1.15E-02
900	1.43E-07	1.44E-02
925	1.15E-07	1.62E-02

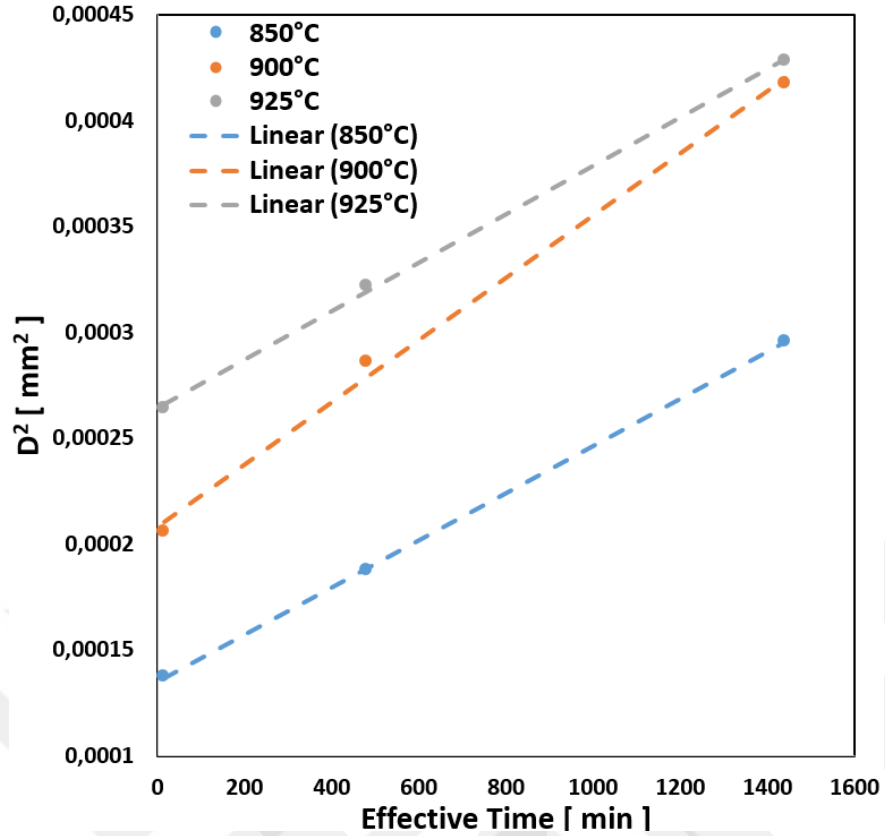

Figure 30. Trendlines of grain sizes and effective time

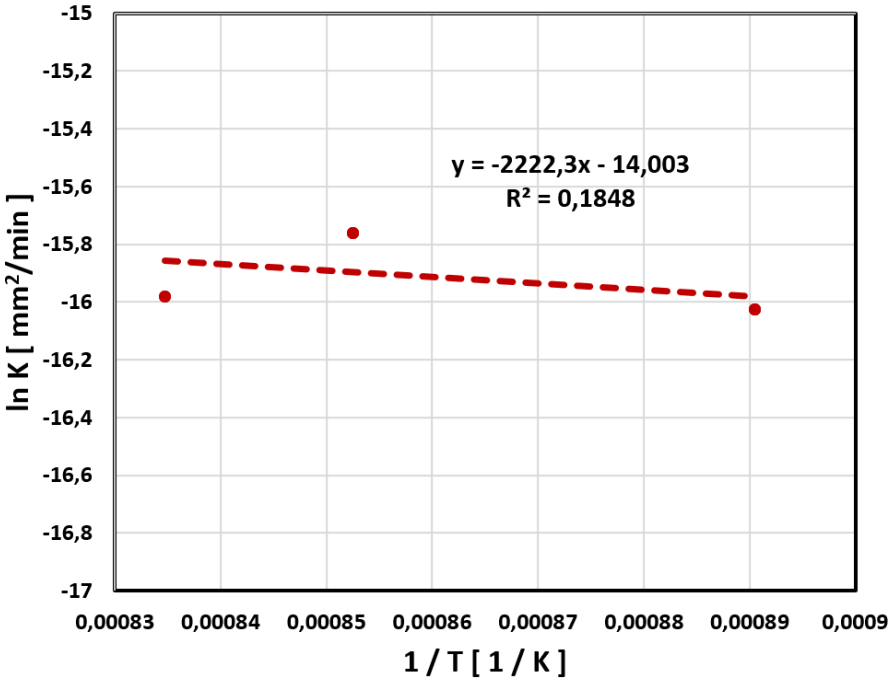

Figure 31. Trendline of lnK values and 1/T values

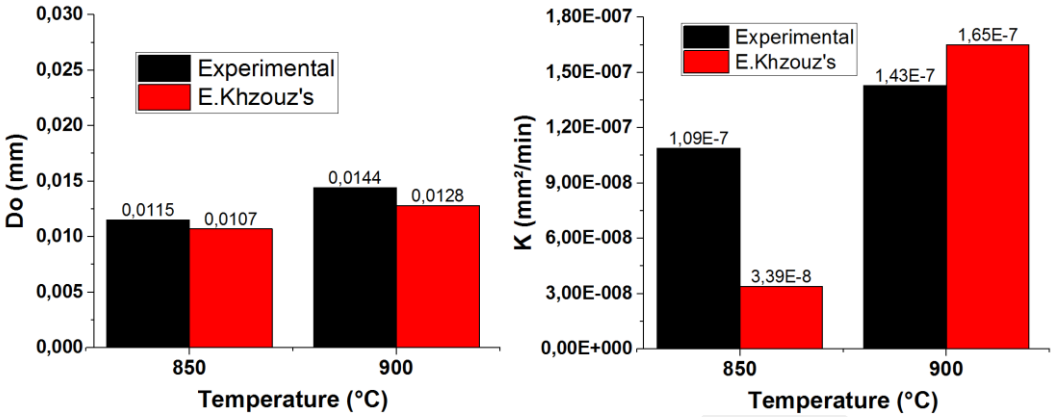

Figure 32. The calculated K and Do values of the current study compared to the E.Khzouz's study

Table 12.Q and K_0 values of DIN 22NiCrMo2-2

DIN 22NiCrMo2-2	
Q (J/mol)	**K_0** (mm^2/min)
18.476	8.29E-07

4.4. Discussions

In this chapter, the austenite grain growth kinetics of DIN 22NiCrMo2-2 steel was determined from a quantitative metallographic study. Moreover, those results were used to construct a grain growth model. And, ideal grain growth law and Arrhenius formula were used for determination of austenite grain growth kinetic parameters.

Besides, the grain growth kinetics studies for the DIN 22NiCrMo2-2 steel were compared with literature, it has been determined that the kinetic parameters are different from obtained in this studies. This difference can be attributed to the chemical composition differences of the samples, as tabulated in Table 9. Specifically, the Mo content of the present steel is higher than the reference study [23] . Mo has been reported to form fine carbides such as Mo_2C, which can pin the grain boundaries, inhibit grain growth and therefore lower the K value [60].

For the metallographic determination of PAGS, a wetting agent was used in Krahe and Desnoues's etch. However, PAGS could not be detected in some experiments because

the etching process is not homogeneous on the whole surface due to the chemical structure of the wetting agent. Furthermore, as described in Chapter 3, the homogeneity of the microstructure of the DIN 22NiCrMo2-2 steel caused the grain boundaries not to appear clearly. So, the low temperature range at which the PAGS can be calculated in this study may cause the grain growth kinetics parameters to differ from the parameters obtained in the literature study.

At the same time, the prior austenite grain size found in the literature for the DIN 22NiCrMo2-2 steel is in the range of 8.5 to 10.5 ASTM [9]. Also this is in agreement with the PAGS results of this study.

PAGS is an important parameter affecting phase transformation kinetics. For this reason, PAGS is required as input data to determine the CCT and TTT diagrams by computational methods. For the present steel, the PAGS has values in the range of 8.9-10.1 for 850 - 900 °C and 0.25 - 8 hours austenitization conditions. Austenite grain size were used for calculation of CCT and TTT diagrams in the following chapter.

CHAPTER 5

DETERMINATION OF PHASE TRANSFORMATION KINETICS

5.1. Introduction

The austenite is transformed into different phases depending on the cooling rate during quenching after carburizing. The final microstructure of the steel at room temperature influences the mechanical properties. For this reason, it is important to know the transformation kinetics to determine the properties after heat treatment. Critical temperatures (M_s, M_f, B_s, A_{c1} and A_{c3}) and transformation kinetics were determined and presented in the form of CCT (Continuous Cooling Transformation) and TTT (Isothermal Transformation Diagram) diagrams.

In the present study, CCT diagrams were determined by measuring some specific volume change during continuous cooling by dilatometric method. This method is supplemented by metallography measurement. And TTT diagram was calculated from experimentally determined CCT diagram using inverse analysis method in Forge® software.

Moreover, TTT and CCT diagrams were calculated via JMatPro® software. CCT and TTT diagrams were calculated under the same conditions as the experimental method and the austenitizing temperature is used as 880 °C and the austenitizing time is used as 1 hour. The PAGS of the DIN 22NiCrMo2-2 steel in accordance with the presented studies in Chapter 4 was entered as 9 (ASTM grain size number) for determination of the CCT and TTT diagrams by a computational methods.

5.2. Experimental Determination of CCT

A dilatometer device (DIL-805 A/D Baehr-Thermoanalysis GmbH) which is shown in Figure 33, was used to experimentally determine the CCT diagram of the DIN 22NiCrMo2-2 steel.

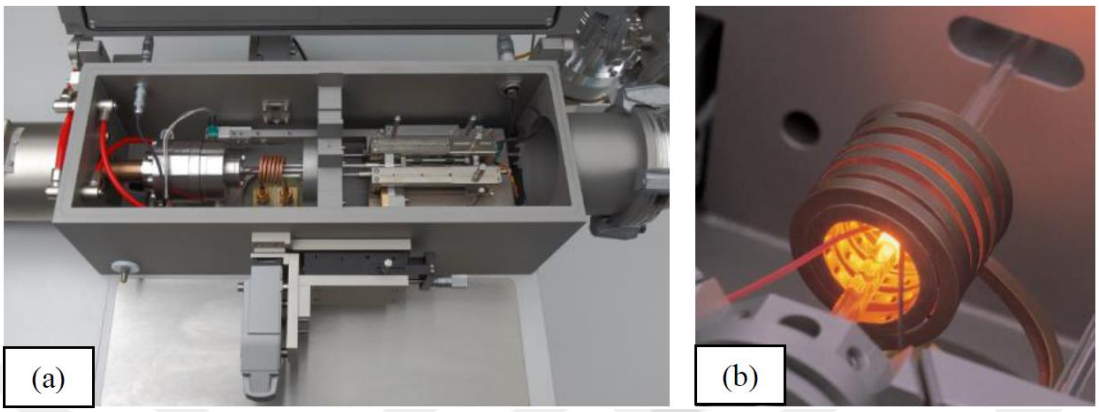

Figure 33. (a) Chamber of Baehr-Thermoanalysis GmbH, DIL 805 A/D dilatometer and (b) induction coil used in DIL 805 A/D.

The technical drawing of the test samples for dilatometric analysis is shown in Figure 34. The test samples have 4 mm outer diameter, 10 mm height, and 2 mm wall thickness. The inner hole of the cylinder is 2 mm.

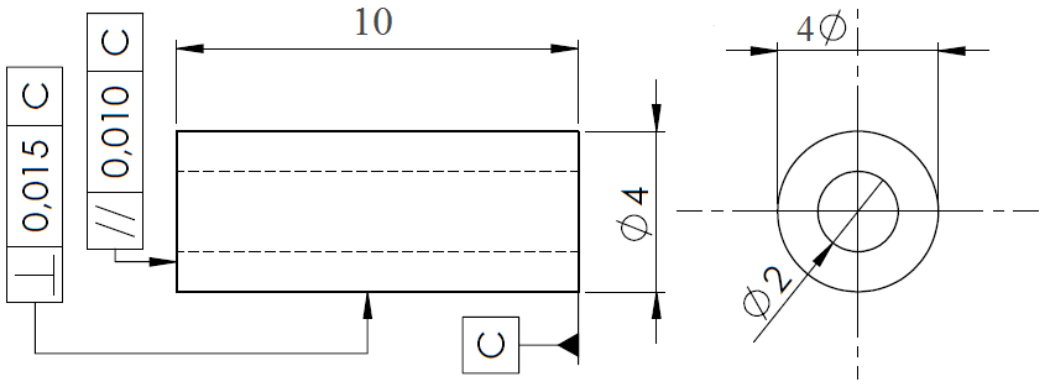

Figure 34. Technical drawing of the dilatometer test specimens used to determination of the CCT and also M_s and M_f temperatures

The dilatometer measures the expansion of the sample in length direction, during heating and/or cooling. For carburized steels heating above A_3 temperature causes formation of austenite. During cooling, this austenite transforms into other phase(s) or phase mixtures. A change in sample length (actually volumetric expansion) is also

associated with those transformations. The reason for this change is the atomic packing factor of the austenite and other phases in the crystal lattice structures. The atomic packing factor of the austenite phase is 74%, which is the highest factor, since the face-centered cubic (FCC) structure is (together with the hexagonal closed packed structure) the most densely packed structure. As the austenite phase transforms into other phases with lower atomic packing density, volume expansion occurs. This expansion was seen in the area indicated by number 4 in Figure 35. A typical dilatometric curve is shown in Figure 35. The curve shows the change in sample length as a function of temperature. The curve contains 4 distinct sections. Section 1 represent the heating to the austenitizing temperature also the linear thermal expansion coefficient of the room temperature phases can be extracted from the slope of the curve in this section. In the section 2, the length of the sample is reduced; because of the formation of austenite. Since austenite has a denser atomic structure the sample length reduces. The sample is cooled rapidly after austenitization, and this is represented in section 3. The rate of cooling at this section can also be denoted as $t_{8/5}$, which is the duration during which temperature of the sample decreases from 800 to 500 °C. Section 4 shows the transformation of austenite into other phases (such as ferrite, pearlite, bainite and martensite) during continuous cooling.

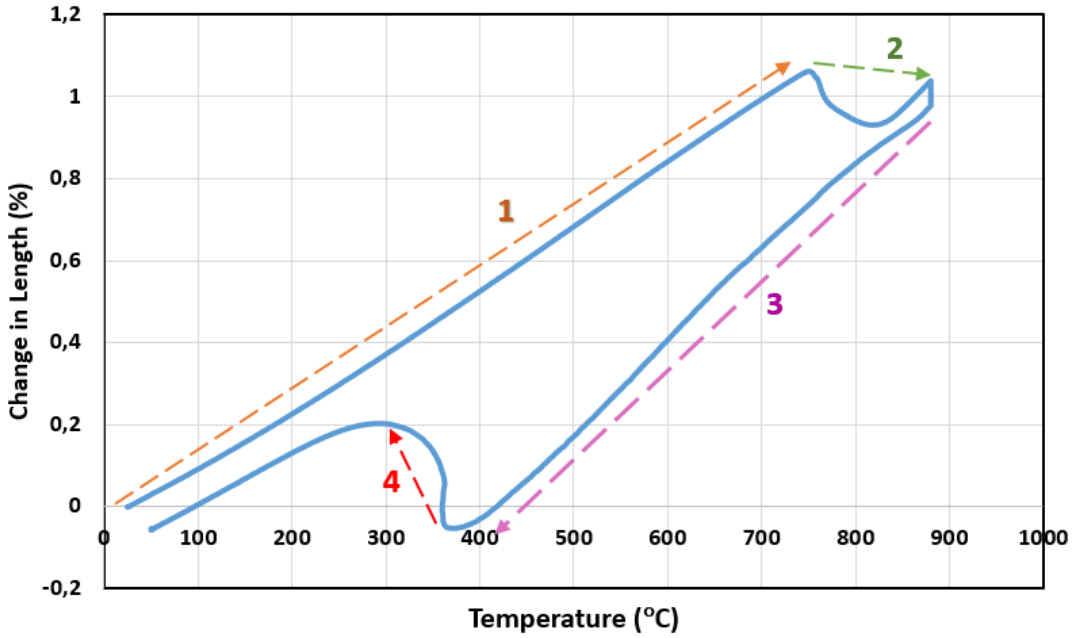

Figure 35. A typical dilatometric curve which represents the change in length as a function of temperature.

The dilatometer applies a pre-programmed heat treatment cycle including heating, holding at austenitizing temperature and continuous cooling steps as shown in Figure 36. When the % carbon isopleth of DIN 22NiCrMo2-2 steel was examined in Figure 26, it was determined that the temperature at which the initial microstructure is completely transformed to the austenite phase was 880 °C. So, in the present case the samples were heated to austenite temperature 880°C with a heating rate of 1°C/s using nitrogen gas and held at this temperature for 1 hour. The program t8/5 times (time to cool down from 800°C to 500°C) were used to indicate the cooling rates in the continuous cooling step. 17 different $t_{8/5}$ times, that were used to determine the CCT diagram, are indicated in Table 13. All of the dilatometer experiments were performed in 2 repetitions.

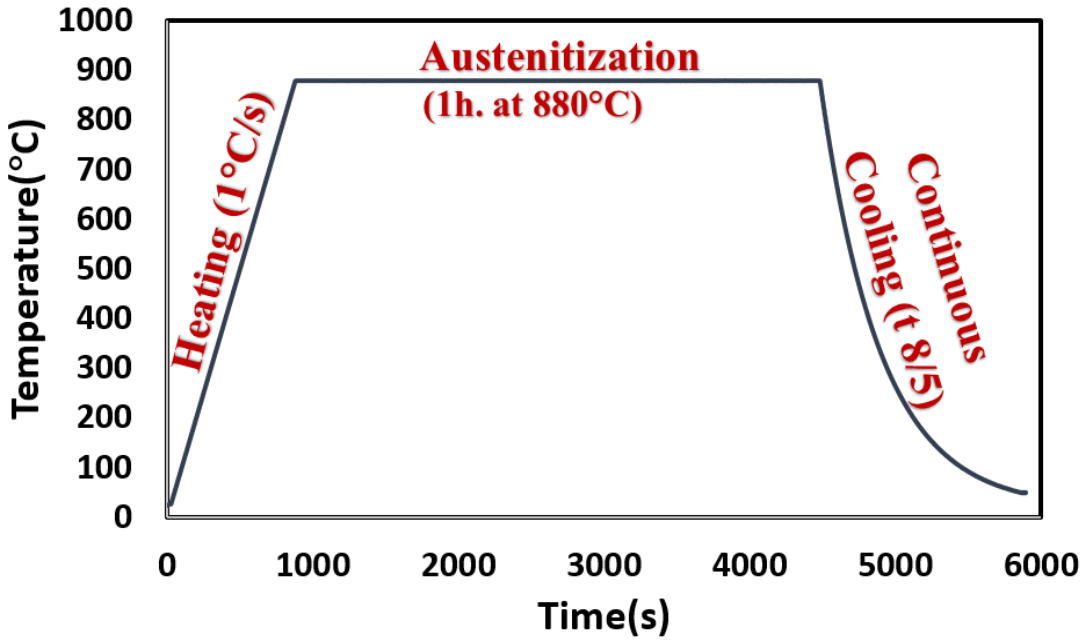

Figure 36. The temperature-time program of the CCT tests

The transformation start and finish temperatures of the phases were obtained by using the slope of the relative change in length vs. temperature curve as shown in Figure 37. The CCT test which was performed for 400 s t8/5 time was represented as an example in Figure 37. Phase transformation temperatures was determined using offset lines which are intersect the experimental curve [61]. In this figure, 1 and 2 number points indicate the start and finish temperatures of the ferritic transformation while 3 and 4 number points indicate the start and finish temperatures of the pearlitic transformation.

Table 13.The t8/5 times used to determine the CCT diagram

Sample Code	t8/5 times	Transformation Phases
No 1	2s	Bainite + Martensite
No 2	3s	Bainite + Martensite
No 3	4s	Bainite + Martensite
No 4	10s	Bainite + Martensite
No 5	15s	Bainite + Martensite
No 6	20s	Bainite + Martensite
No 8	30s	Ferrite + Bainite
No 9	60s	Ferrite + Bainite
No 10	100s	Ferrite + Bainite
No 11	200s	Ferrite + Bainite
No 12	300s	Ferrite + Bainite
No 13	400s	Ferrite + Pearlite
No 14	600s	Ferrite + Pearlite
No 15	1000s	Ferrite + Pearlite
No 16	2000s	Ferrite + Pearlite
No 17	3000s	Ferrite + Pearlite

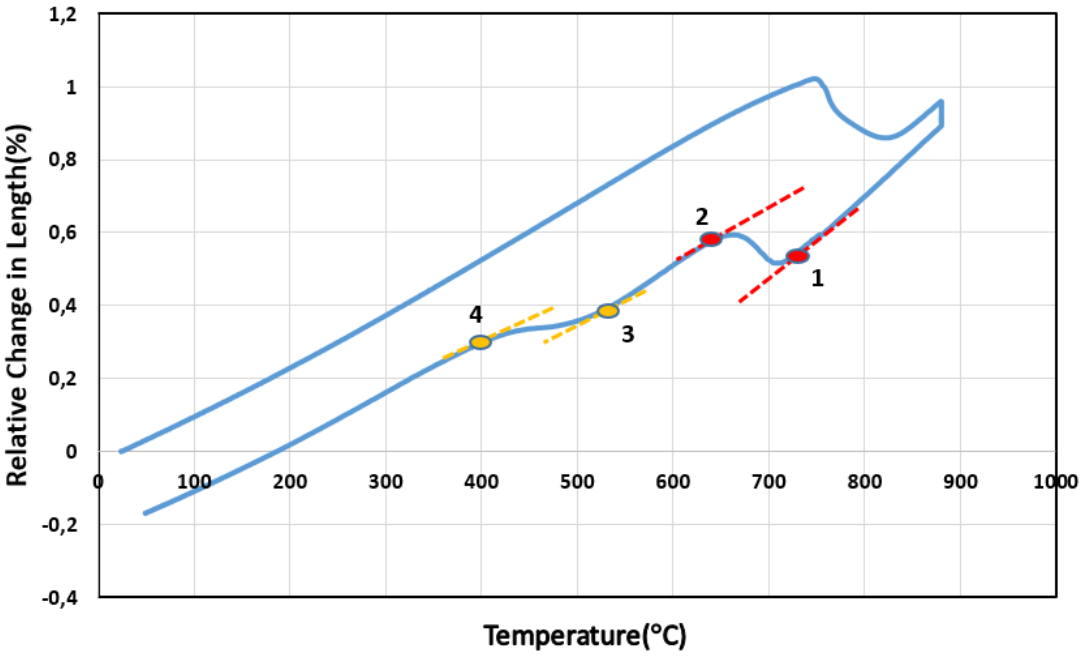

Figure 37. Relative change in length vs. temperature curve for 400s t8/5 time CCT test

The relative change in length curves (ex: Figure 37) indicate time and temperature of a phase transformation. However, these curves does not indicate which phase transformed from austenite. In order to identify the product phase, metallographic examination should be performed. The resulting microstructures after the dilatometer tests (given in Table 13) samples were analyzed taken at 5000x magnification via SEM. Figure 38 -Figure 40 show the results of those SEM examinations. As the cooling rate increases, the martensite and bainite fraction increase as shown in Figure 38. Also at cooling rates slower than 20 s $t_{8/5}$ time, the microstructure is composed of bainite, ferrite and pearlite, respectively in Figure 39 and Figure 40.

As the cooling rate increases, the diffusion time of carbon and other alloy elements decreases. In the perlite transformation occurring at slow cooling rates, as a result of Fe and C atoms diffusing, the structure consists of ferrite and cementite. As the cooling rate increases, the Fe atom cannot be diffused, the C atom becomes difficult to diffuse, and the bainitic transformation takes place. Bainite is divided into upper and lower bainite depending on the cooling rate. In the martensite transformation that takes place as a result of rapid cooling, the C and Fe atoms cannot be diffused.

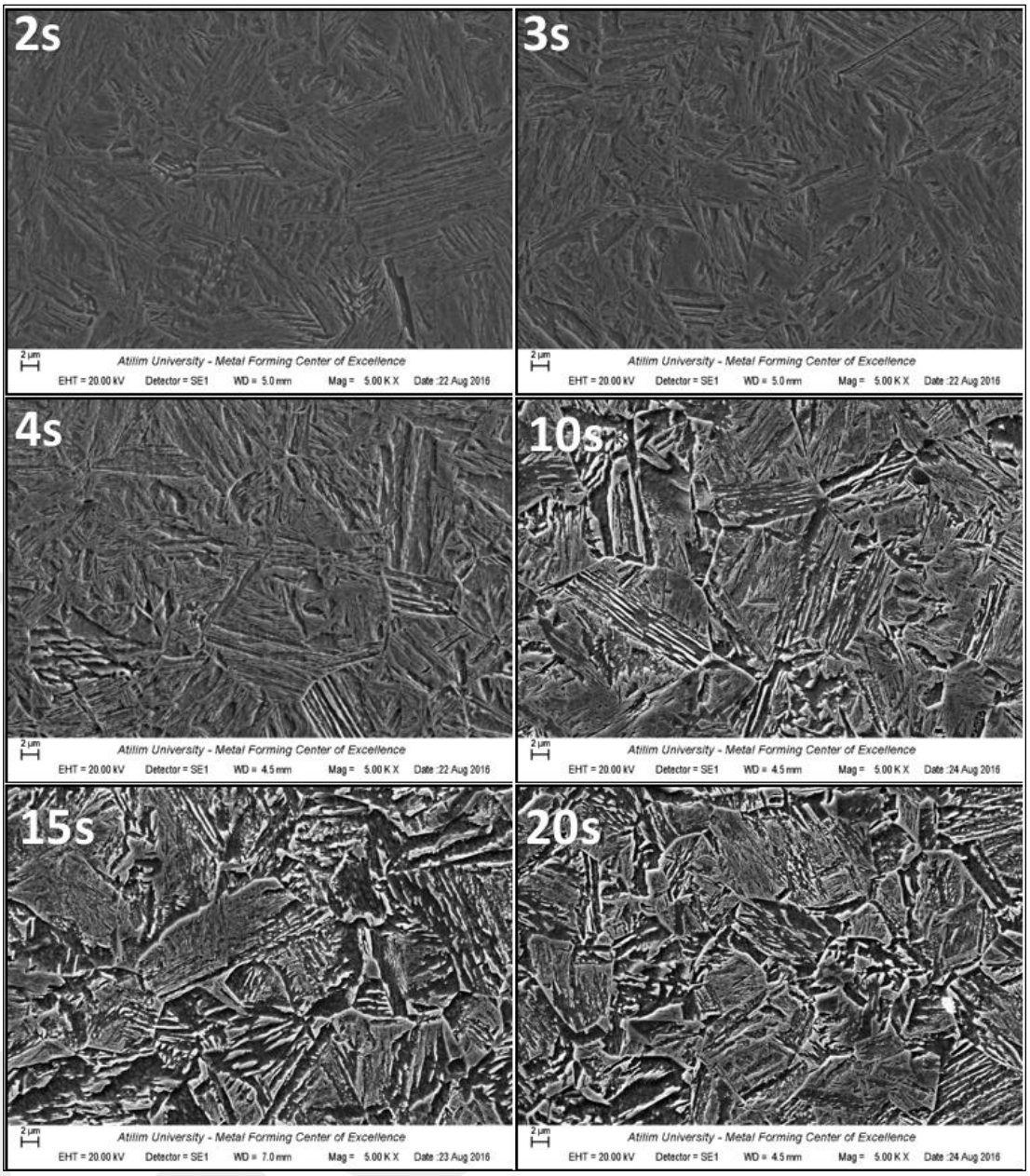

Figure 38. SEM micrographs of the samples taken at 5000x magnification. The corresponding t8/5 times are given in upper left corner of each micrograph

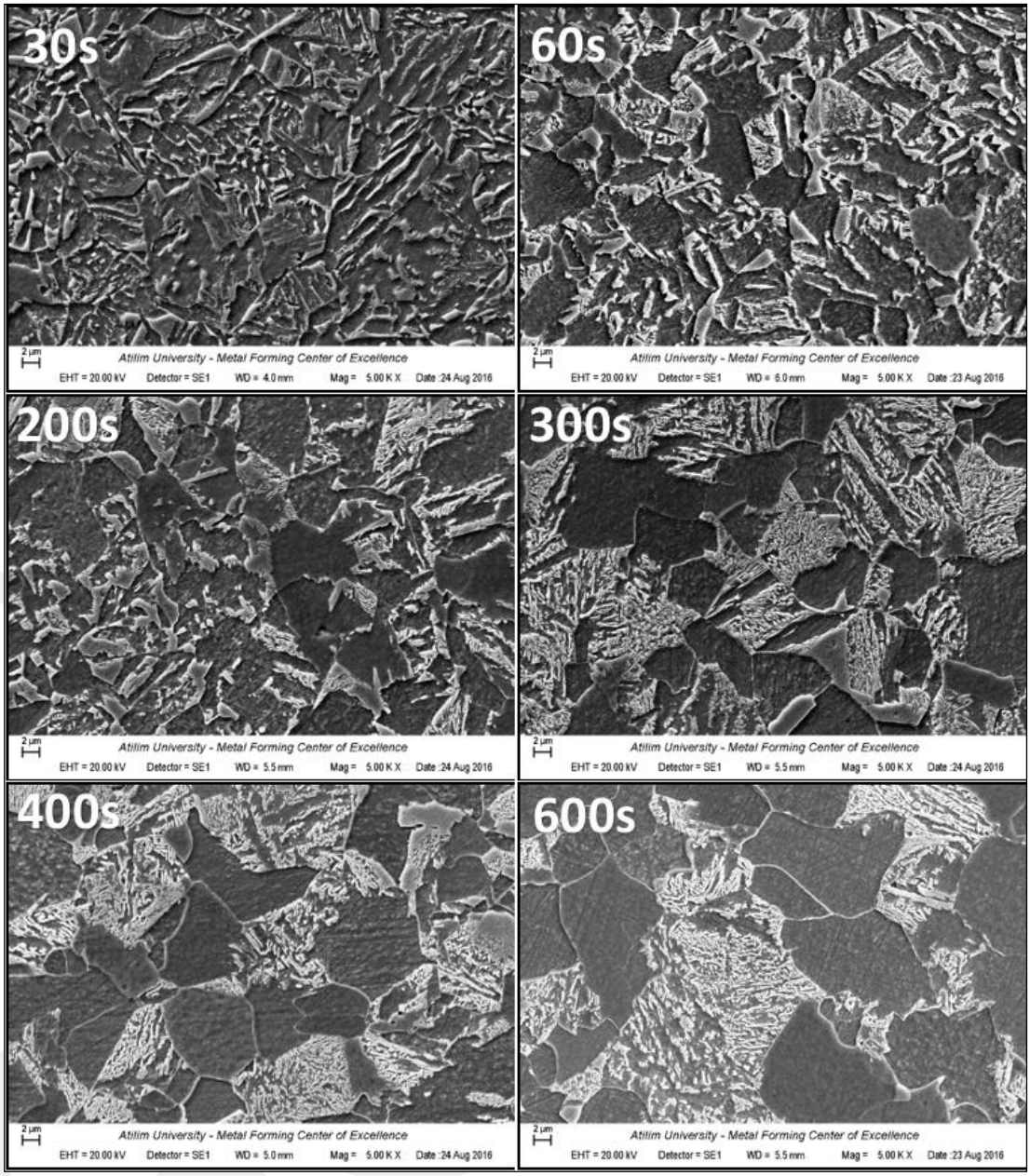

Figure 39. SEM micrographs of the samples taken at 5000x magnification. The corresponding t8/5 times are given in upper left corner of each micrograph

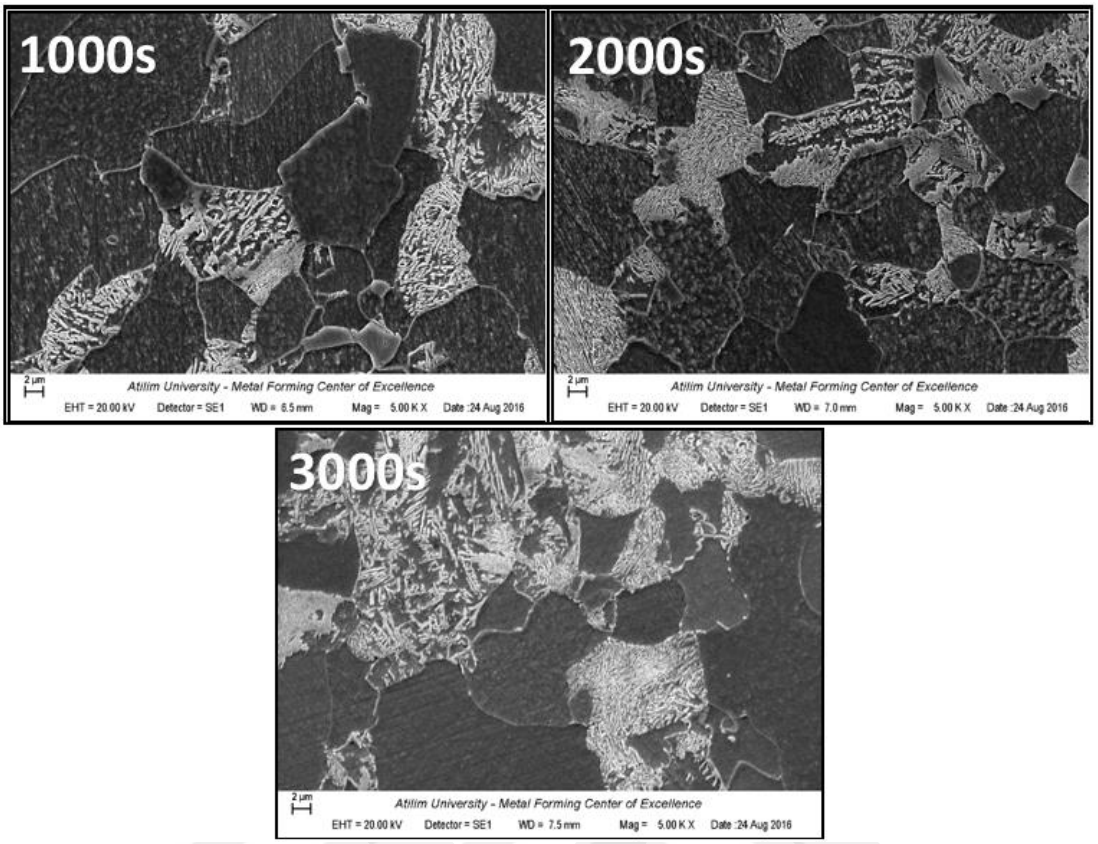

Figure 40. SEM micrographs of the samples taken at 5000x magnification. The corresponding t8/5 times are given in upper left corner of each micrograph

Figure 41 compares the experimentally determined CCT diagram of the DIN 22NiCrMo2-2 steel to the one that is calculated using JmatPro software. It should be noted that the $t_{8/5}$ times tabulated in Table 13 were determined based on the CCT diagram calculated by JMatPro®. Since CCT diagrams are a function of cooling rate, an adequate comparison requires the same, if not similar, cooling rates. Figure 41 indicates a reasonable agreement between the experimental and computational studies for determining the CCT diagram of DIN 22NiCrMo2-2 steel. There are also some minor differences between the diagrams in Figure 41, particularly in the "ferrite start" curves. Also CCT diagram in literature of 8620 steel is given in Figure 42.

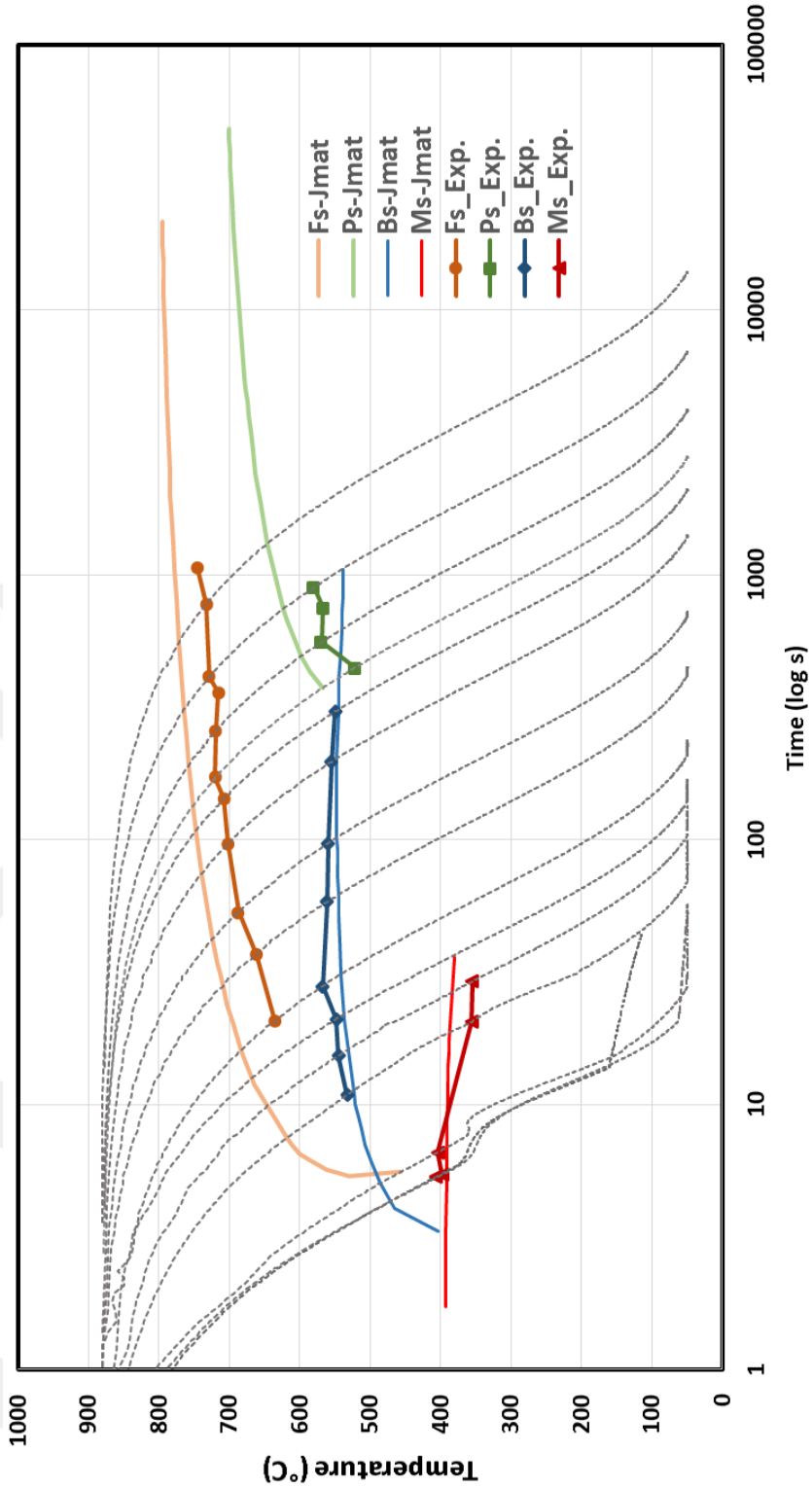

Figure 41. Comparison of CCT diagrams of DIN 22NiCrMo2-2(SAE 8620H) steel obtained experimentally and via JMatPro® software. Dashed lines refer as the cooling rate. (Composition: 0.21% C, 0.84% Mn, 0.33% Si, 0.53% Ni, 0.57% Cr, 0.24% Mo)

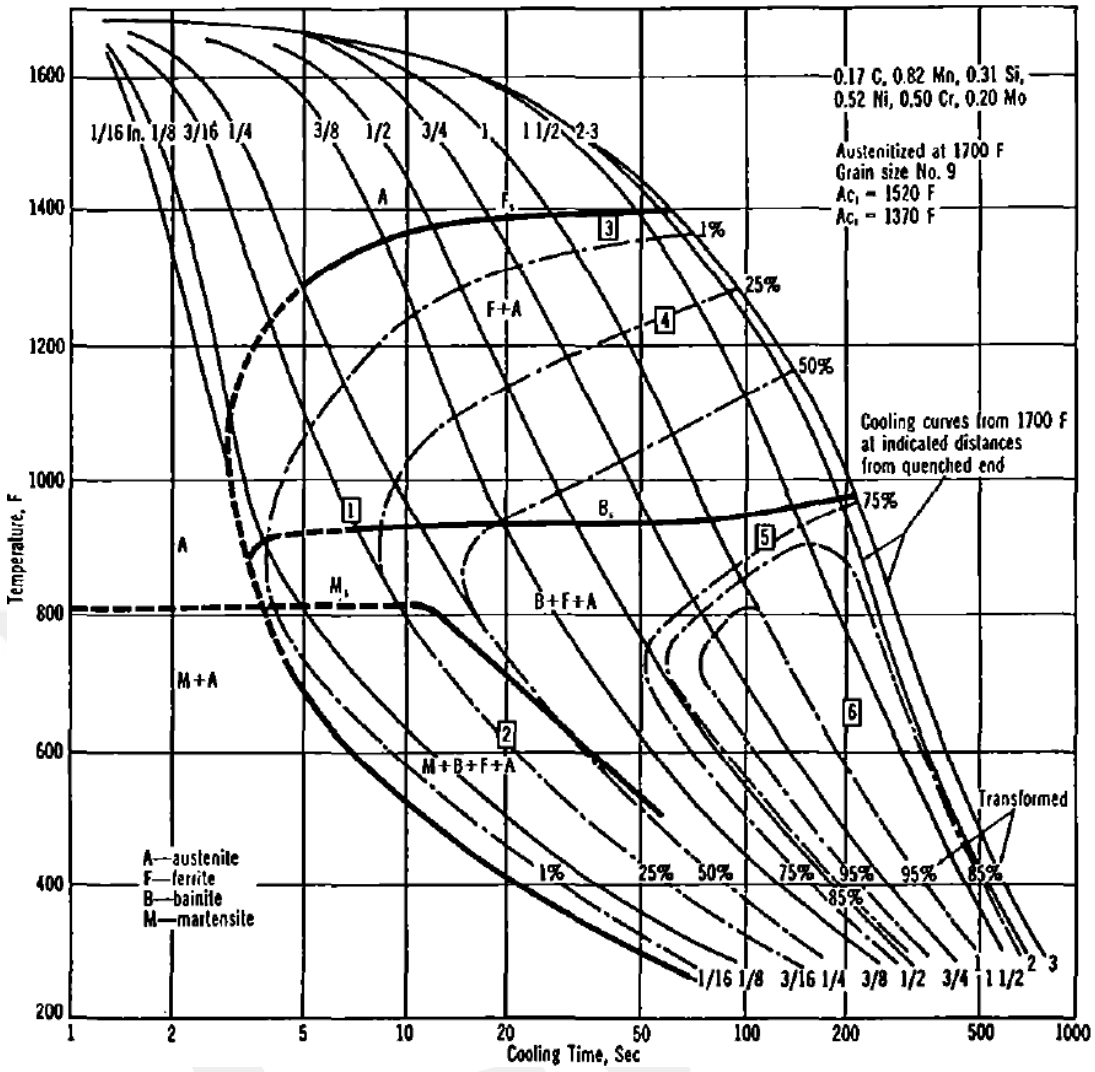

Figure 42. 8620 CCT diagram. Composition: 0.17% C, 0.82% Mn, 0.31% Si, 0.52% Ni, 0.50% Cr, 0.20% Mo. Austenitized at 925°C. Grain size: 9 [31]

5.3. Experimental Determination of Critical Temperatures (M_s, M_f, B_s, A_{c1} and A_{c3})

The temperature for the austenite begins to form (A_{c1}), the finish temperature for the transformation from ferrite into austenite (A_{c3}), the bainitic transformation start temperature (B_s), the martensitic transformation start temperature (M_s) and the martensitic transformation finish temperature (M_f) were experimentally determined by using quenching dilatometry for DIN 22NiCrMo2-2 steel.

Martensite is a diffusionless transformation of austenite formed by rapid cooling to room temperature. It is also called the athermal transformation. The transformation

starts at a certain temperature, which is the martensite starting temperature (M_s) and ends at a certain temperature which is the martensite finishing temperature (M_f). The temperatures M_s and M_f vary depending on the content of % C and these temperatures decrease as the amount of % C increases. In order to determine these temperatures, sub-zero test were carried out with a dilatometer device on a steel DIN 22NiCrMo2-2 containing 0.2 % C. The experiments were repeated 3 times.

The test program as shown in Figure 43, sample is heated to 880 °C with 1 °C/s and austenitization for 1 hour, then cooled to -120 °C with 250 °C/s. After sub-zero test, the sample length changing with temperature is shown in Figure 44. Looking at the change in the sample length in the curve, it is determined that the phase transformation takes place in region indicated by 1 number.

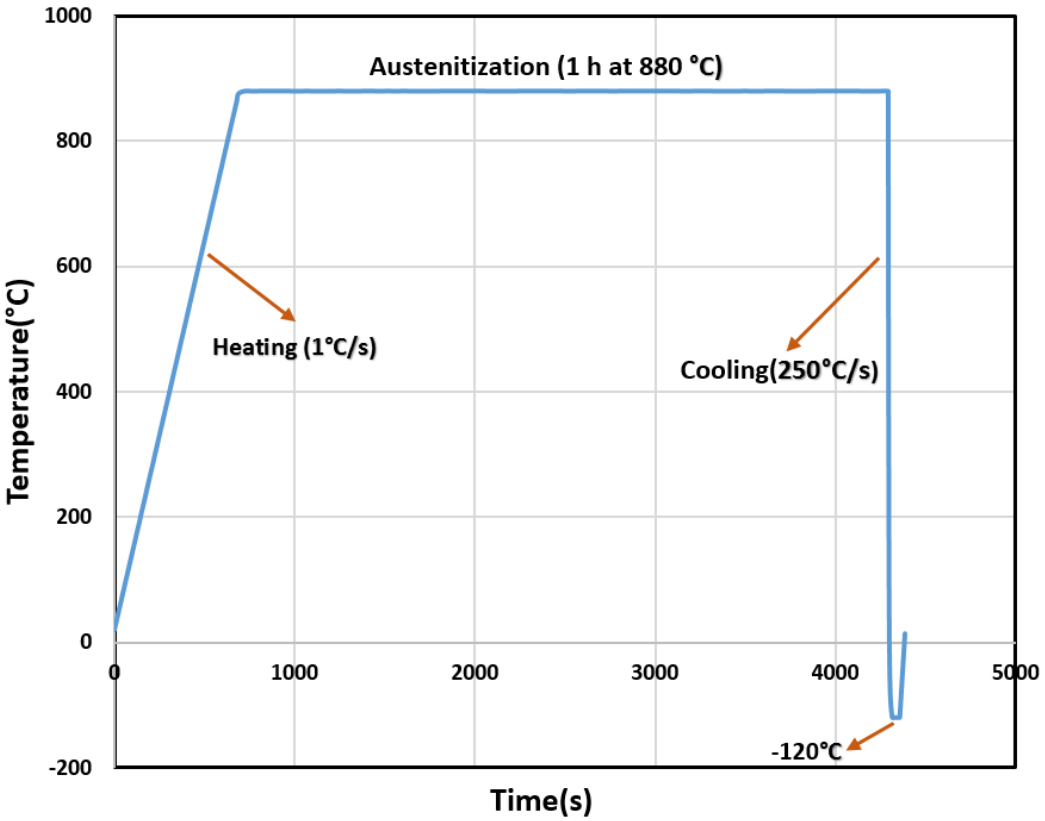

Figure 43. Temperature program for sub-zero test

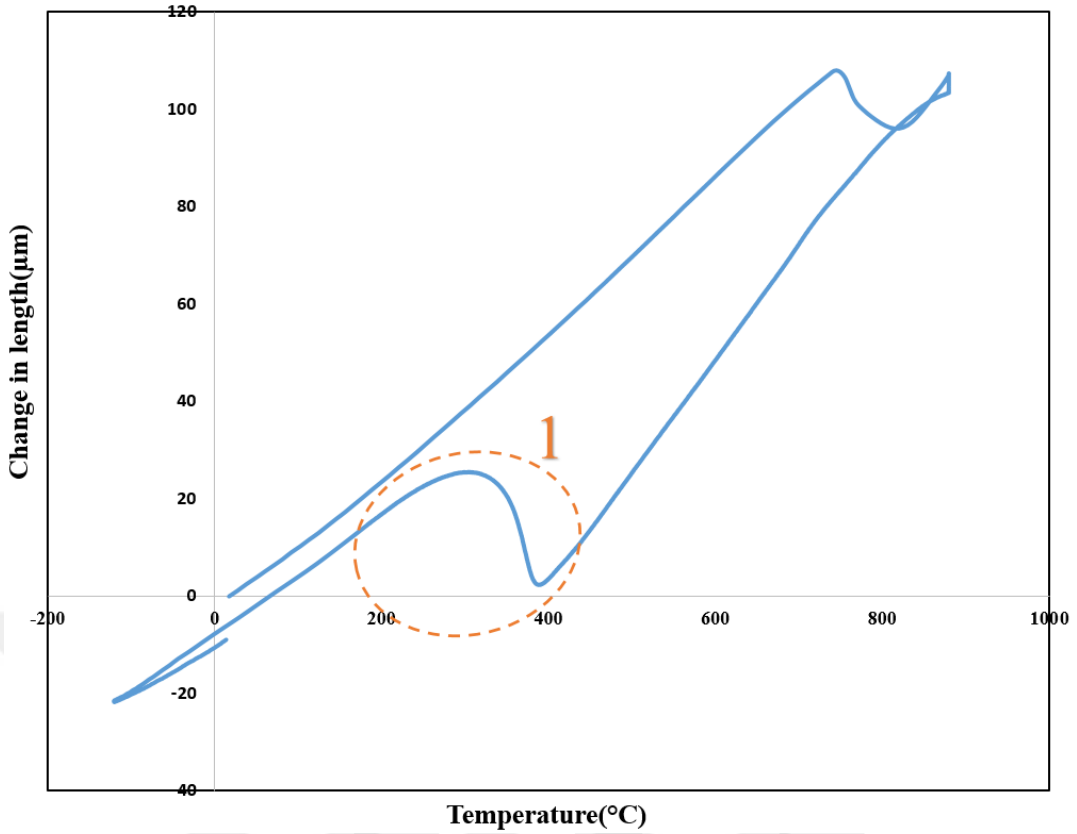

Figure 44. Change in length vs. temperature curve for sub-zero test, region 1 indicate the transformation of the austenite phase to the martensite phase.

Figure 45 shows the region 1, which is shown in Figure 44, in more detail. Here, rather than using the offset method, tangent lines were drawn in the regions where the transformation into martensite started and finished. In order to determine the phase fraction at any temperature (T), linear mixing rule of dilation was used [62], [63] :

$$f(T) = \frac{l(T) - ls(T)}{lf(T) - ls(T)} \qquad \text{Eq. 15}$$

where, f (T) is phase fraction, $l\ (T)$ is length change at a given temperature, ls (T) is length change at a given temperature on austenite line and lf (T) is length change at a given temperature on martensite line.

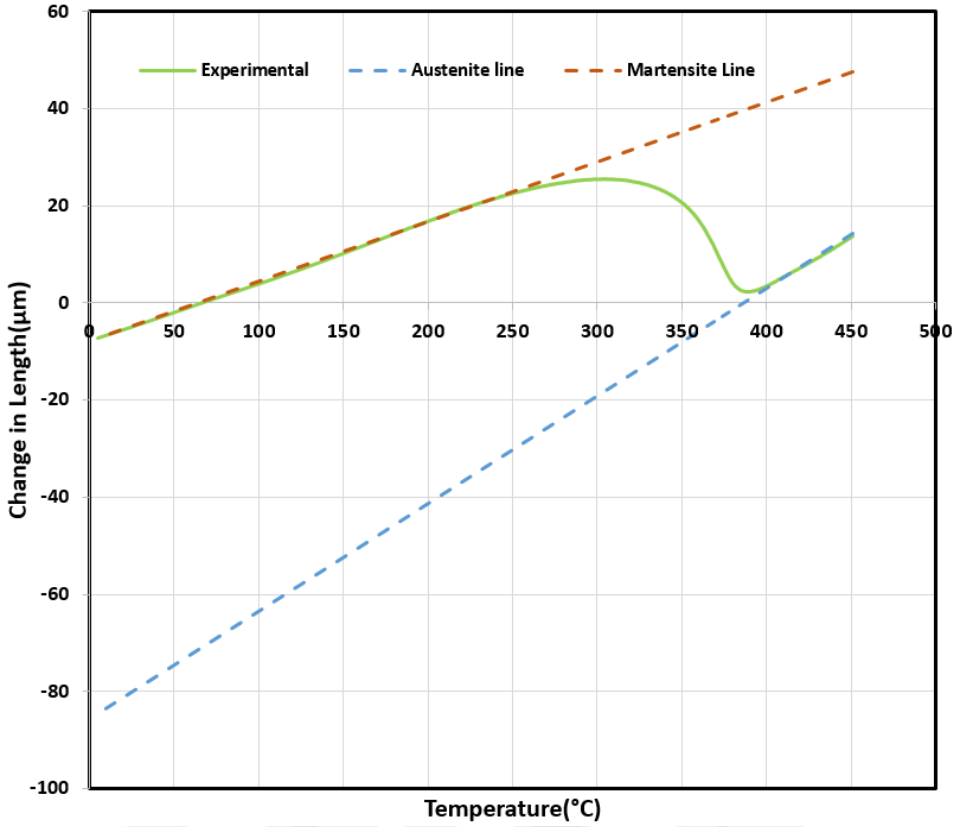

Figure 45. Change in length vs. temperature curve which represent to martensitic transformation

Phase fraction of martensite versus temperature curve was calculated using Eq. 15 and shown in Figure 46. The M_s temperature is define as the temperature at which the martensite phase fraction is 1%. In a similar manner, the M_f temperature is defined as the temperature at which the martensite fraction is 99%. Using this procedure, the martensite start and finish temperatures of the present DIN 22NiCrMo2-2 steel were calculated as 387±4 °C and 230±9 °C. Those temperatures were calculated from the results of experiments, which were repeated 3 times. After the determination of the M_s and M_f temperatures, the Koistinen Marburger model was used to study the martensitic transformation kinetics. By changing the model parameter α in the Eq. 12, the transformation kinetics were fitted in accordance with the experimental data. As can be seen in Figure 46, the model generated by taking α value 0.02 is in good agreement with the experimental data. Moreover, the bainitic transformation start temperature (B_s) was determined as 567°C from the CCT curves.

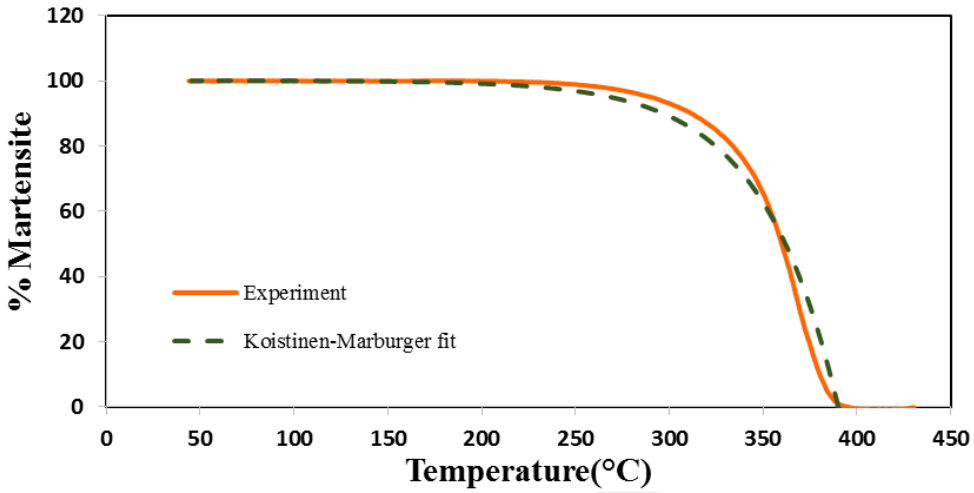

Figure 46. Martensite fraction vs. temperature curves determined by experimentally and fitting of the Koistinen-Marburger equation

In all of the CCT tests, austenite transformation takes place in region 2 on the Figure 35, so the A_{c1} and A_{c3} temperatures can be determined from all of these tests. As an example, the austenite transformation from initial phase and the A_{c1} and A_{c3} temperatures which were determined using offset method are shown in Figure 47. A_{c1} temperature was determined as 727.75±16 °C and A_{c3} temperature as 838.15±4 °C by taking the average of all measurements.

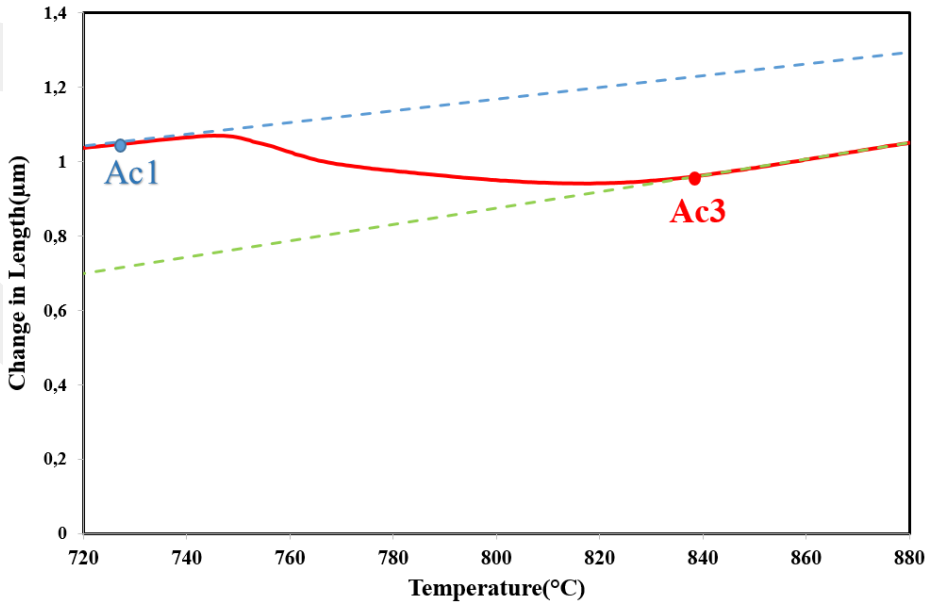

Figure 47. Change in length vs. temperature curve which represents to the austenite transformation

5.4. Determination of Isothermal Diagram (TTT) From Inverse Analysis of CCT

The TTT diagram is calculated from the experimentally determined CCT diagram by using inverse analysis method implemented in the Forge® software. In this computer-aided calculation method, the experimentally determined Continuous Cooling Transformation curves (CCT curves), critical temperatures, prior austenite grain size (PAGS) and the chemical composition of the material are the input parameters. The software first calculates a reference TTT diagram, according to the chemical composition of the steel. Also, this reference TTT diagram determines the range of optimization parameters to be used in the calculation. The software uses the Kirkaldy model which is fixing three optimization parameters (P_1, P_2 and P_3) to calculate the transformation initial curves for ferrite, pearlite, and bainite then transformation curves for pearlite and bainite up to 90%:

$$Log_{10}\big(Time(s)\big) = P_1 - P_2 Log_{10}\big(A_s(K) - T(K)\big) + \frac{P_3}{T(K)} \qquad \text{Eq. 16}$$

where $T(K)$ and $A_s(K)$ are respectively transformation temperature and asymptotic temperature in Kelvin for different phases and P_1, P_2, P_3 are optimization curve parameters [64].

In this study, the experimental CCT diagram shown in Figure 41 was entered into the forge software and the TTT diagram was calculated by inverse analysis. The parameters which were referred in Eq. 16 and calculated using inverse analysis in Forge software were listed in the Table 14. The nose times were calculated as 3.07 second for ferrite and 952.69 second for pearlite and 1.637 second for bainite, using parameters in Table 14. In addition, the TTT diagram was calculated in the JmatPro software using the input data which are the chemical composition, austenite temperature and PAGS number of DIN 22NiCrMo2-2 steel. A comparison of the TTT diagrams calculated via Forge® and JmatPro® software were shown in Figure 48. Besides, the TTT diagram of 8620 steel in the literature is given in Figure 49.

Table 14.Transformation kinetic parameters for the model

IT Curve Name	A_s(°C)	P_1	P_2	P_3
Ferrite_TDEB	810	3.839	4.041	5283.482
Pearlite_TDEB	739	10.250	4.455	2258.947
Banite_TDEB	567	-0.988	3.040	5418.639
Pearlite_T90	739	2.950	0.190	394.030
Bainite_T90	567	0.232	0.190	394.030

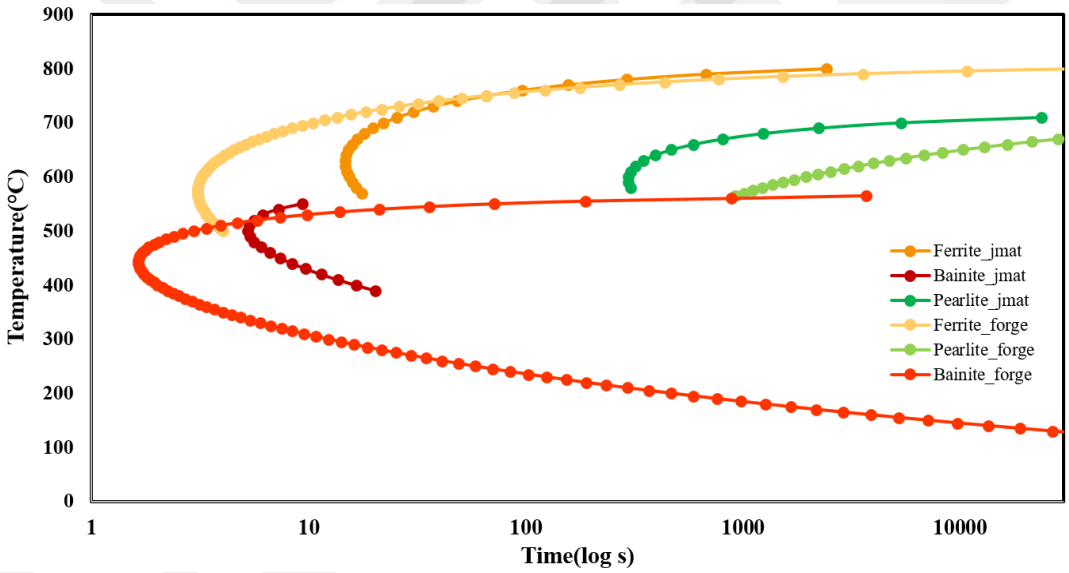

Figure 48. Comparison of TTT diagrams for the DIN 22NiCrMo2-2(SAE 8620H) steel

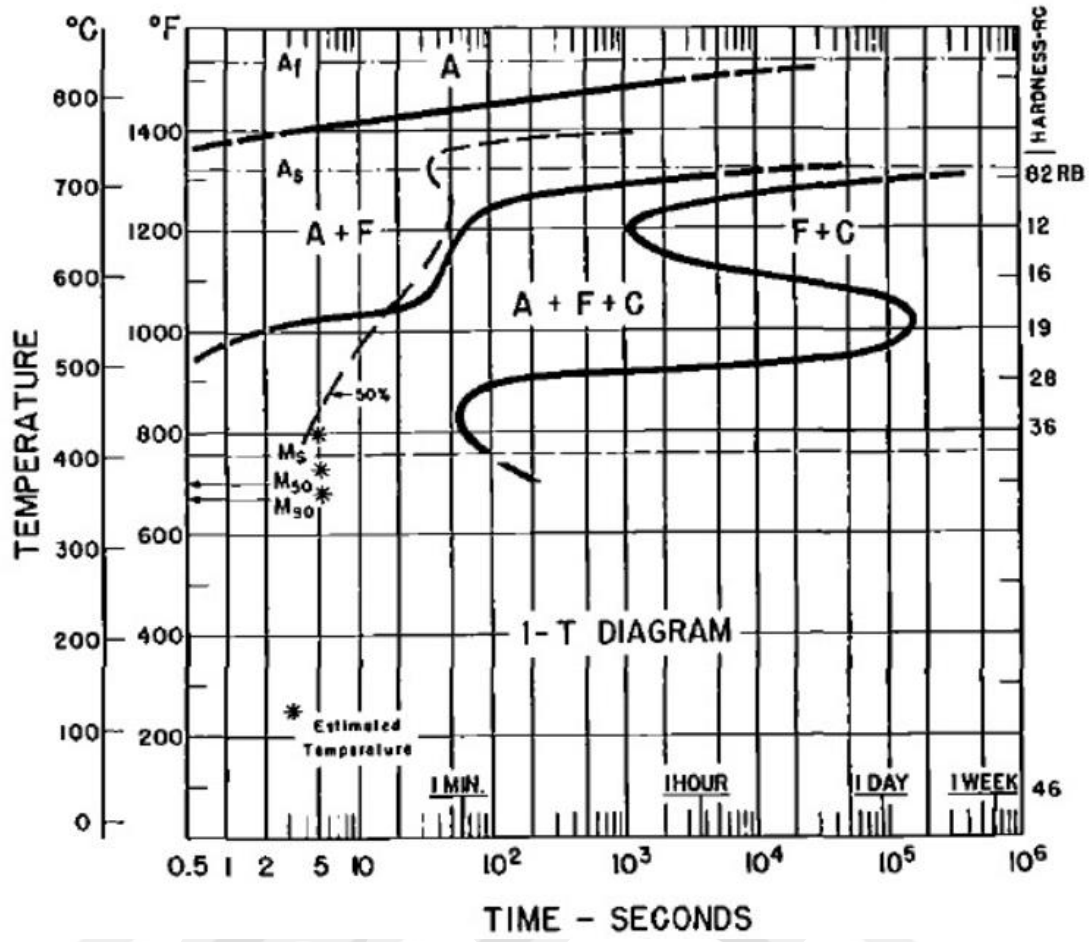

Figure 49. TTT diagram of 8620 steel; composition: 0.18 C, 0.79 Mn, 0.52 Ni, 0.56 Cr, 0.19 Mo. Austenitized at 899°C. Grain size: 9-10. A_{c3}: 825°C. A_{c1}: 745°C [31]

5.5. Discussions

In this chapter, CCT diagram and critical temperatures were experimentally determined via dilatometric analysis. Furthermore, TTT diagram was determined by inverse analysis from CCT using Forge® software with computational method. Moreover, TTT and CCT diagrams calculated via JmatPro® software.

The CCT diagrams calculated by the experimental method and JMatPro® are compared and found to be compatible with each other. Only, a difference of 35-50 °C at around ferrite and pearlite curves were observed, as seen in Figure 41. The difference between the experimental and computationally determined CCT diagrams may depend on the experimental conditions. Particularly, austenite grain size which varies depending on the austenite temperature has a significant effect on phase

transformation temperature [65]. Also, it should be noted that during the dilatometer tests austenitization was carried out at 880 °C. For this temperature the prior austenite grain size was not clearly determined. The JmatPro software uses the PAGS in the CCT calculation and the PAGS in the software is entered as 9 ASTM based on the work done in Chapter 4. For this reason, there was a slight difference between CCT diagrams which are determined by experimental method and JMatPro®.

When the CCT diagrams determined in this study were compared to the ones in the literature, it is seen that the curves are consistent but slight differences are also present. The amount of alloying elements in the literature study are more than the steel used in this study. It has been determined in the literature studies that the differences in chemical composition cause a change in the CCT diagram. The increase in the amount of alloying elements shifts phase transformations for a longer period of time [66]. Also S.Chupatanakul has studied the effect of alloying elements on the M_s and B_s temperatures. The decrease in M_s and B_s temperatures is clearly visible in the Eq. 17 and Eq. 18 which are used to calculate these temperatures as the alloying elements increase [67], [68].

$$M_s(°C) = 545 - 470.4(\%C) - 3.96(\%Si) - 37.7(\%Mn) - 21.5(\%Cr) + 38.9(\%Mo) \quad \text{Eq. 17}$$

$$B_s\ (°C) = 830 - 270(\%C) - 90(\%Mn) - 37(\%Ni) - 70(\%Cr) - 83(\%Mo) \quad \text{Eq. 18}$$

Moreover, the accuracy of the experimentally determined CCT diagram depends on the accuracy of the transformation points. The results of the dilatometer measurements can be influenced by the the measurement method. There is absolutely no specific method for material diversity, thermal properties and therefore the shape of the curves. Since the individual approach was used in the evaluation of dilatometric curves, variations can occur.

The variations in the CCT diagram which is determined experimentally by using dilatometric curves also affects the TTT diagram, which was determined by inverse analysis of CCT. This may be another reason for the difference between the TTT diagrams in Figure 48, other than the PAGS which also affects the phase transformations. As PAGS decreases, the M_s and B_s temperature decreases [69].

Because, fine austenite grain sizes promote the nucleation kinetics, and as the austenite grain size gets smaller, the austenite grain boundary area per volume increases, which increases the density of nucleation sites. Moreover, the fine austenite grains have more grain boundaries which play a role as obstacles during the growth of the martensite, therefore reducing the M_s and B_s temperatures [70], [71]. The PAGS effect is seen clearly in difference between bainite transformation curves in Figure 48.

In the TTT calculations using the inverse analysis in the Forge software, firstly the CCT curves are fitted in accordance with the experimentally obtained CCT diagram. Also the calculated critical temperatures (M_s, M_f, B_s, A_{c1} and A_{c3}) are entered into the program to set CCT curves. The parameters in Table 14 are determined by the average measurements of the experimentally obtained critical temperatures, neglecting the variation. The variation in critical temperatures may cause to difference of TTT curves between Forge® and JmatPro® software in Figure 48.

The differences between CCT and TTT diagrams determined experimentally, computationally and from literature are attributed to variations in the PAGS, the differences in the chemical composition and variation of measurement methods.

The raw material characterization, austenite grain growth kinetics and phase transformation kinetics studies which were described up to this section had been done so that the DIN 22NiCrMo2-2 steel can be added to the material library of the simulation software. In the next section, experimental and simulation studies for carburized quenching of DIN 22NiCrMo2-2 and DIN 16MnCr5 steels are presented. Moreover, the results of the DoE studies on carburized quencing are also evaluated.

CHAPTER 6

CHARACTERIZATION STUDIES ON GAS CARBURIZED SHAFTS

6.1. Introduction

In the previous chapters of this thesis, characterization studies in laboratory environment for DIN 22NiCrMo2-2 material was explained. This chapter describes the characterization of carburized quenched shafts, the process of which were carried out on the stepped and stepless shaft in the industrial and simulation environments. The shaft adjusts the amount of fuel according to the engine's different load and speed conditions. It is necessary to increase the usage performances in order the shafts to perform this operation. Thus, the outer parts of the shafts must be resistant to abrasion, the inner parts must be resistant to possible impacts and to be tough. Carburizing heat treatment is applied to the shafts in order to provide high hardness, fatigue resistance and wear resistance. The surface hardening thermochemical heat treatment procedure with carburizing which is made on a shaft manufactured in industry (ESTAŞ Company) is shown in Figure 50. The procedure consists of heating, carburizing, diffusion, oil cooling, deep freezing and finally tempering.

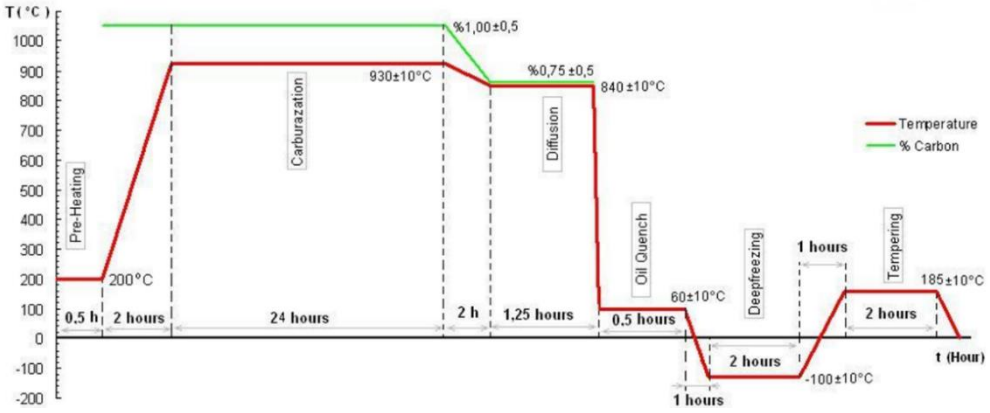

Figure 50. The surface hardening thermochemical heat treatment procedure made on cam shaft.

Since carburizing is a time-consuming process, industrial companies may use different furnaces for the production of the same component depending on the schedule and availability within the firm. Furnaces from different manufacturers and even different types of carburizing furnaces can be used for the same part. This can cause a huge variability in the case-depth, hardness distribution and distortion behavior of the products. In fact, the present study revealed that a significant variation is observed even in between two same model furnaces manufactured by the same company. The parameters controlling the variability is diverse and is very hard to control under industrial conditions. Some of those hard to control parameters include endogas generation system, gas flow control system, sealing of the furnace, damage in the refractory material, conditions in the quench bath etc. From an industrial perspective, it is almost impossible to keep these independent furnaces to operate exactly the same. Thus, an intelligent approach which can reduce the variability under real manufacturing conditions is necessary. In H.Yılmaz`s thesis [5], this problem was handled by optimization using the Taguchi method. The main objective was to determine the process parameters which minimize the variability in process outputs (case-depth, core-hardness, carbon depth, diameter change etc.) independent of the selected furnace. The target was to maximize the Signal/Noise Ratio (SNR) for case-depth while minimizing the mean value of diameter change. This chapter focusses on the determination distribution of hardness and microstructure on the carburized quenched shafts in this prescribed DoE approach. The details of the experimental design and complete results can be found in H.Yılmaz`s thesis [5].

6.2. Test Procedure and Materials

Microstructure, hardness and case depth of the shafts can be controlled by controlling the parameters of the carburizing process. In order to reduce variation of process parameter, 3 factor 2 level Taguchi design was utilized. In this experiment design, the furnace used as a variation source (noise factor). For this reason, experiments were carried out using 2 different (noise level) furnaces.

The aim of the Taguchi design is to determine the parameters that will minimize the variability in the depth of the hardened layer in the furnace. The fixed and variable parameters in the Taguchi experiment are shown in Table 15.

Table 15.Variable and fixed parameters and their values used in the Taguchi experiment

	Parameters	**Values**
Variable	**T_1 (**Carburizing Temperature)	910°C-930°C
Variable	**%C_1 (**Carbon potential at the carburizing step)	0.90%C-1.10%C
Fixed	**t_1 (**Carburizing time)	24 hour
Fixed	**T_2 (**Temperature before quenching)	850°C
Fixed	**%C_2 (**Carbon potential before quenching)	0.7%
Fixed	**t_2 (**Waiting time before quenching)	2 hour
Variable	**T_{oil} (**Oil temperature)	60°C-70°C
Variable	**F(**Furnace**)**	F1-F2

The carburizing experiments with the Taguchi test design described in Table 17 were carried out on the stepped and stepless shaft produced from DIN 16MnCr5 and DIN 22NiCrMo2-2 steels for each set. According to Taguchi test design only experimental tests were performed on DIN 22NiCrMo2-2 steel since the data of the steel is not included in the simulation software's material library. Also carburizing studies were performed on the DIN16MnCr5 material whose chemical composition close to DIN 22NiCrMo2-2 steel, for comparison of simulation and experimental tests. The chemical compositions of the DIN 16MnCr5 steel is present in the simulation software's material library and determined experimentally were given in Table 16. Also the chemical composition of the DIN 22NiCrMo2-2 steel which was specified in section 3.1 is also given in Table 16. Figure 51 shows the geometry of the stepless and stepped shafts used in the industrial carburizing tests. The central section of the stepless shaft and the middle sections of each step of the stepped shaft which were represented in Figure 51 were cut with wire cut electrical discharge machining (EDM) to remove the 20 mm high samples, for the hardness and microstructure analysis.

Table 16.Chemical composition of DIN 22NiCrMo2-2 steel and DIN 16MnCr5 steel

	Wt%	C	Mn	Cr	Si	P	S	Mo	Ni	Fe
DIN 16MnCr5	Experiment	0.168	1.12	0.83	0.31	0.007	0.018	-	-	Bal
	Simulation software's material library	0.15-0.22	0.6-0.9	0.8-1.2	0.1-0.4	<0.035	<0.035	0.15-0.25	0.15	Bal
DIN 22NiCrMo2-2	Average Std.Dev.	0.21 ± 0.005	0.84 ± 0.011	0.57 ± 0.010	0.33 ± 0.018	0.005 ± 0.0002	0.022 ± 0.0007	0.24 ± 0.003	0.53 ± 0.018	Bal

Table 17.3-factorial and 2-level Taguchi type test matrix

Experiment Set No	**F**	**T1 (°C)**	**%C1**	**Toil (°C)**
1	F1	910	0.90	60
2	F1	910	1.10	70
3	F1	930	0.90	70
4	F1	930	1.10	60
5	F2	910	0.90	60
6	F2	910	1.10	70
7	F2	930	0.90	70
8	F2	930	1.10	60

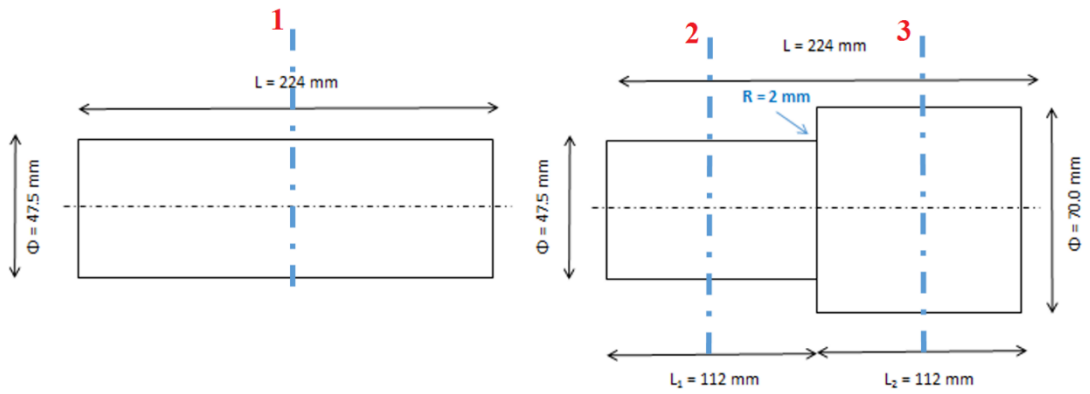

Figure 51. The regions, from which samples are extracted from shafts for metallographic and hardness tests. Sample codes are: number 1 is stepless, number 2 is stepped-Ø47.5, and number 3 is stepped-Ø70 shafts.

6.3. Hardness, Carbon and Microstructure Analysis Results and Discussions

Hardness measurements were taken on the samples which were represented in Figure 51 for each material (DIN 22NiCrMo2-2 and DIN16MnCr5) and each experimental set. Hardness measurements were taken in Zwick® micro-hardness device under 2 kg load using a Vickers tip. The measurements were taken at 200 micron steps from the surface to a depth of 2 mm, and were taken at specific distance from 2 mm to the center. This measurements were repeated for each disc in 3 different angular directions (120 degree angles) and the averages of the measurements were taken.

As a result of carbon profile simulation studies made on stepped and stepless shafts, it has been determined that there is no effect on the carbon distribution of the geometry [6]. Therefore, for carbon profile measurements, cylindrical specimens of 25 mm height with a diameter of 47.5 mm were produced from DIN 16MnCr5 and DIN 22NiCrMo2-2 steels. Carbon profile measurements were taken at a depth of 2 mm from the surface at 200 µm intervals via optical emission spectrometer.

The hardness and carbon graphs obtained from each experimental set were shown in Figures 52 – 55. The graphs represent a change in hardness value and in the amount of carbon as it moves away from the surface for the stepless and stepped shafts.

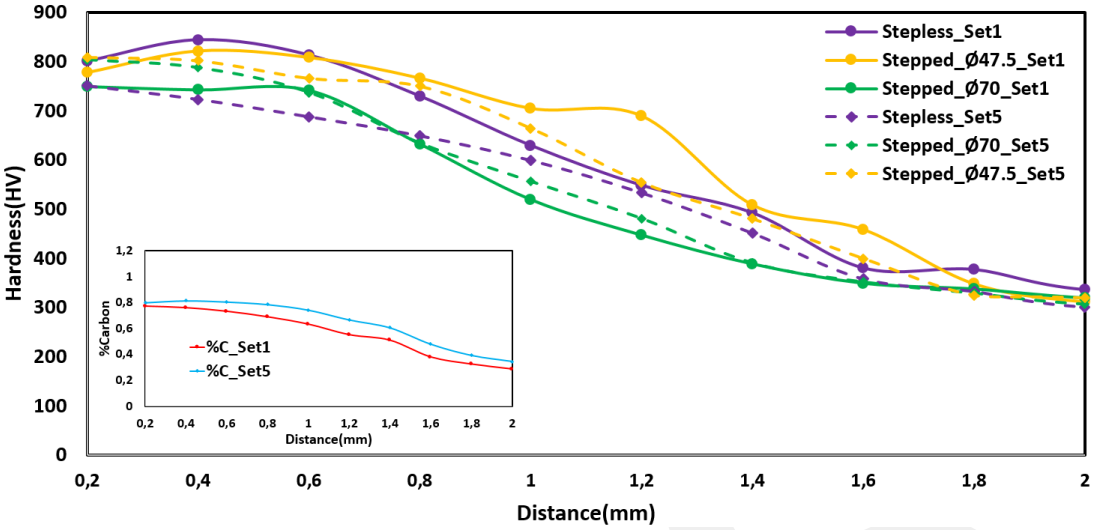

Figure 52. Hardness and %Carbon content graphs of the 1st (T910_%C0.9_Toil60_F1) and 5th (T910_%C0.9_Toil60_F2) sets of DIN 22NiCrMo2-2 steel with stepped and stepless shaft varying from surface to center.

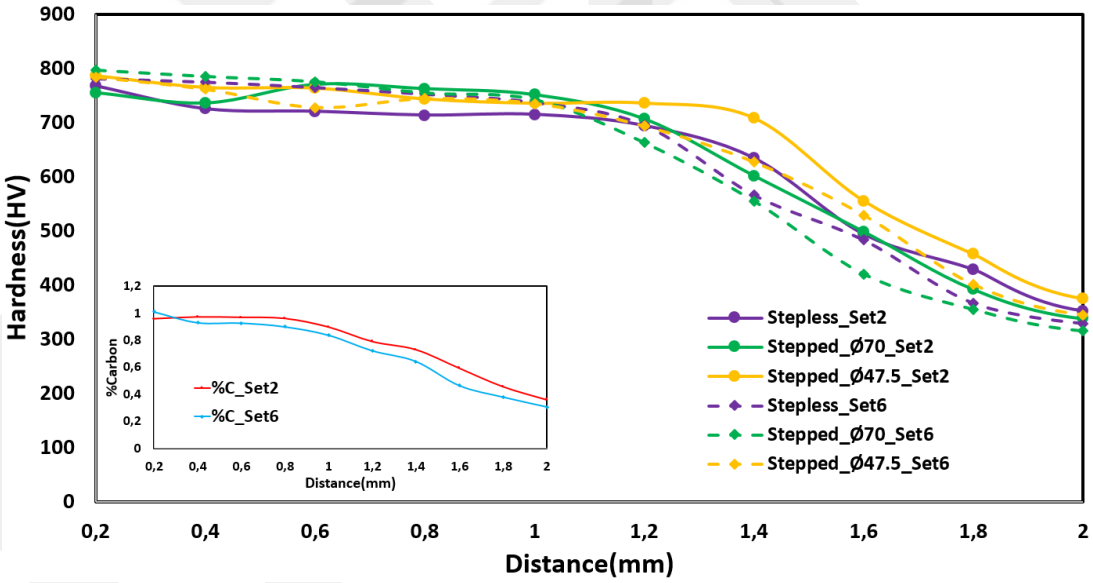

Figure 53. Hardness and %Carbon content graphs of the 2nd (T910_%C1.1_Toil70_F1) and 6th (T910_%C1.1_Toil70_F2) sets of DIN 22NiCrMo2-2 steel with stepped and stepless shaft varying from surface to center.

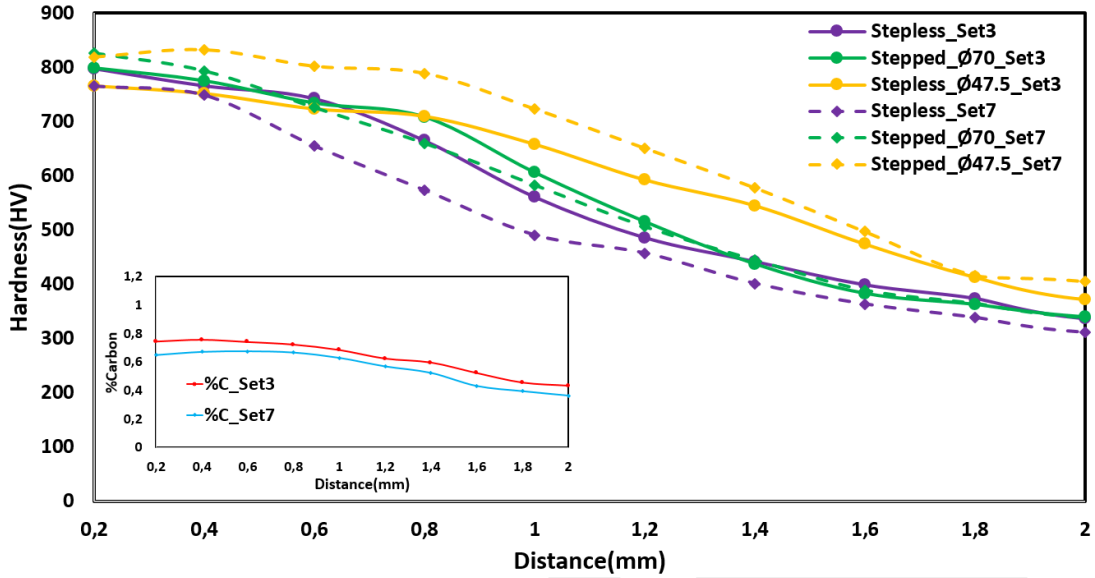

Figure 54. Hardness and %Carbon content graphs of the 3rd (T930_%C0.9_Toil70_F1) and 7th (T930_%C0.9_Toil70_F2) sets of DIN 22NiCrMo2-2 steel with stepped and stepless shaft varying from surface to center.

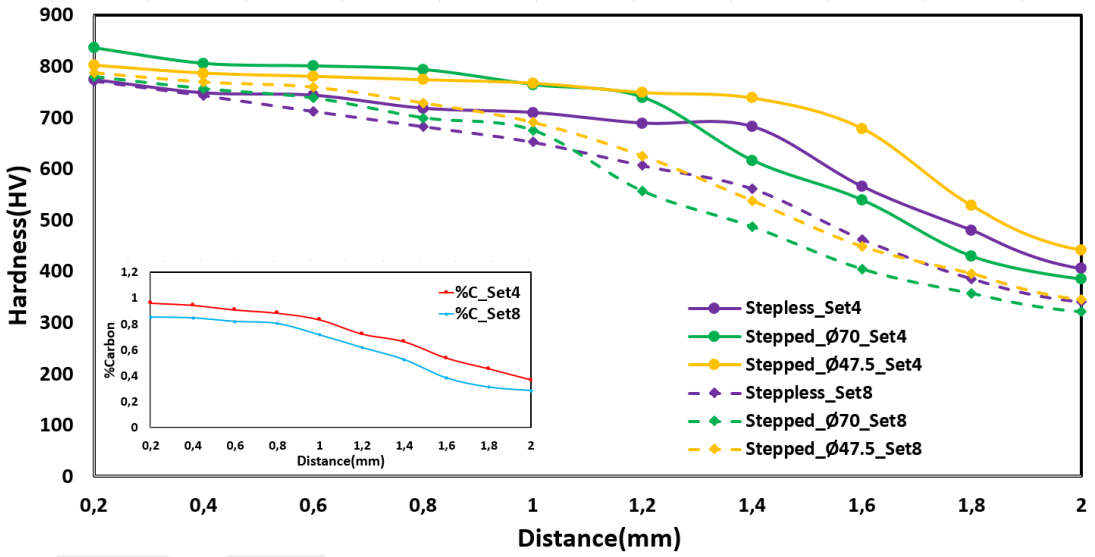

Figure 55. Hardness and %Carbon content graphs of the 4th (T930_%C01.1_Toil60_F1) and 8th (T930_%C01.1_Toil60_F2) sets of DIN 22NiCrMo2-2 steel with stepped and stepless shaft varying from surface to center.

When, surface-to-center carbon profiles shown in Figures 52 – 55 were examined, it was seen that the carbon profiles in the experiments performed in Furnace 1 was higher. The hardness value obtained after quenching and the hardenability of the steel are directly related to the carbon content. It was observed that the hardness value decrease in accordance with the decrease in carbon amount from the surface to the center in all of the graphs in Figures 52 – 55.

Since the 1.1% carbon potential is used in the 2nd and 4th experimental sets, the amount of carbon in the surface is higher in those sets, as shown in Figures 52 – 55. These sets have the same carbon potential (1.1%) but in 4th set the carburizing temperature is 20 °C higher than 2nd sets. The effect of carburizing temperature on diffusion is important as explained in the Eq. 10. The increase in diffusion with increasing temperature has resulted in a higher carbon concentration on the 4th set surface.

The surface and core hardness results of the experiments in the Furnace1 were compared for the stepless shaft of the DIN 22NiCrMo2-2 steel, as shown in Figure 56. The amount of carbon dissolved in the austenite phase is a precise factor that determines the surface hardness. The carbon concentration in the austenitic phase and the percent of alloy elements that influence the carbon diffusion [27]. As the amount of dissolved carbon increases, the hardness of martensite increases with the increase of the distortion of the martensite cubic structure formed after rapid cooling. For this reason, higher surface hardness was obtained in experiments with 1.1% carbon potential. In the 4th experiment set with 1.1% carbon potential and 930°C carburizing temperature, the highest hardness value was reached on the surface with increasing diffusion at high temperature. In addition, the hardness values in the center were lower in all sets than in the surface due to the decreasing carbon diffusion from surface to the center.

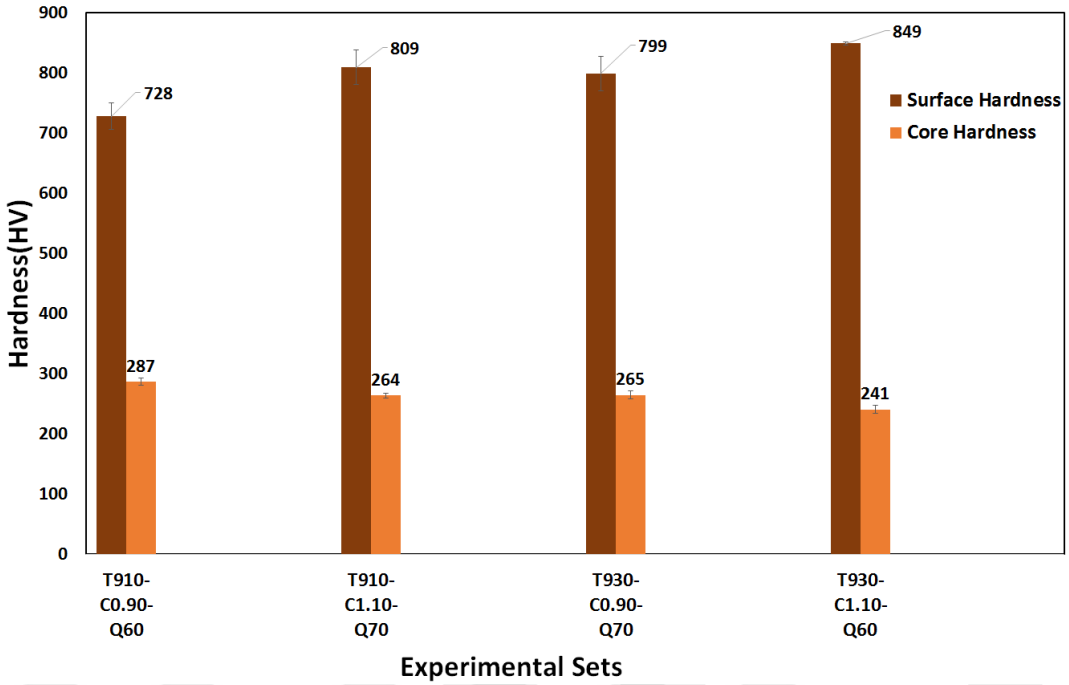

Figure 56. Comparison of surface and center hardness of DIN 22NiCrMo2-2 steel for stepless shaft.

Hardness distributions (profiles) of the 1st and 5th sets for materials DIN 22NiCrMo2-2 and DIN 16MnCr5 were given in Figure 57 and Figure 58 to examine the effect of both material and furnace differences. The DIN 22NiCrMo2-2 steel surface hardness was slightly higher than DIN 16MnCr5 steel for each of the sets in Figure 57 and Figure 58 . Considering the chemical composition of the DIN 22NiCrMo2-2 steel in Table 16, the amount of alloying element is different than DIN 16MnCr5. Also each element has some effect on hardenability in steel. All of the known elements except cobalt, especially elements such as C, Mn and Cr, increase the hardenability of the steel. Since cobalt increases pearlite nucleation and growth, it reduces hardenability [10]. Alloying elements such as chromium and manganese incorporated into the steel slow down the diffusion of carbon atoms during cooling. Therefore, a more moderate cooling rate allows the carbon to remain in the cubic structure and to form martensite. Since 16MnCr5 contains higher Mn and Cr, the hardness curve of 16MnCr5 is higher as shown in Figure 57 and Figure 58. As seen in Figures 52 – 55, the carbon profiles were higher in the furnace 1 than in the furnace 2, therefore it cause the hardness profiles of each materials were also higher in the furnace 1.

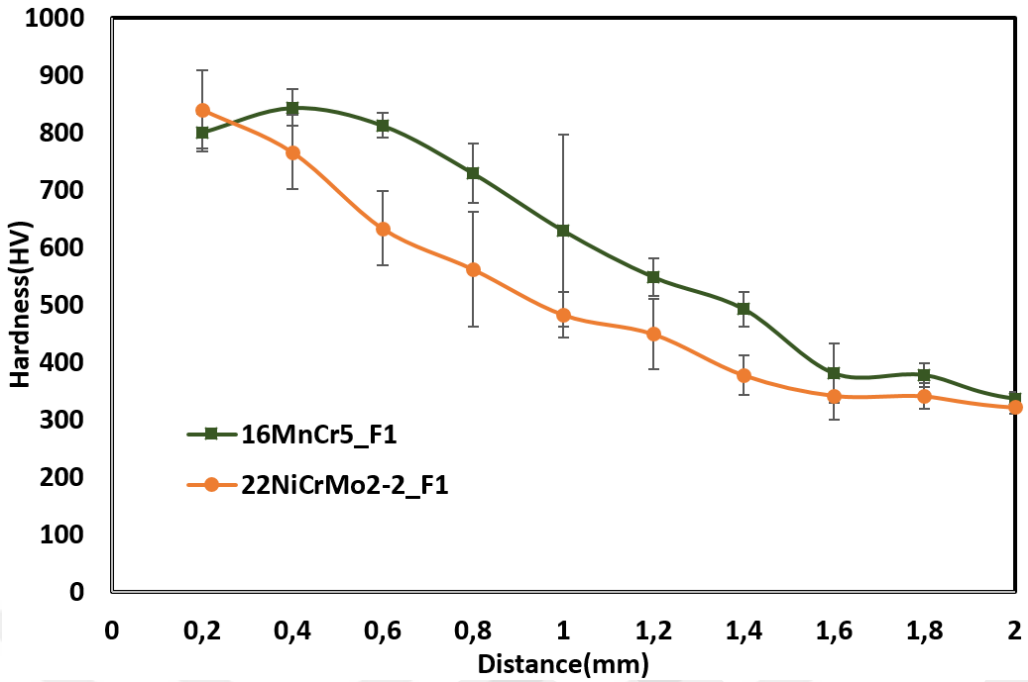

Figure 57. Hardness distributions of the DIN 22NiCrMo2-2 and DIN 16MnCr5 steels for the 1st test set

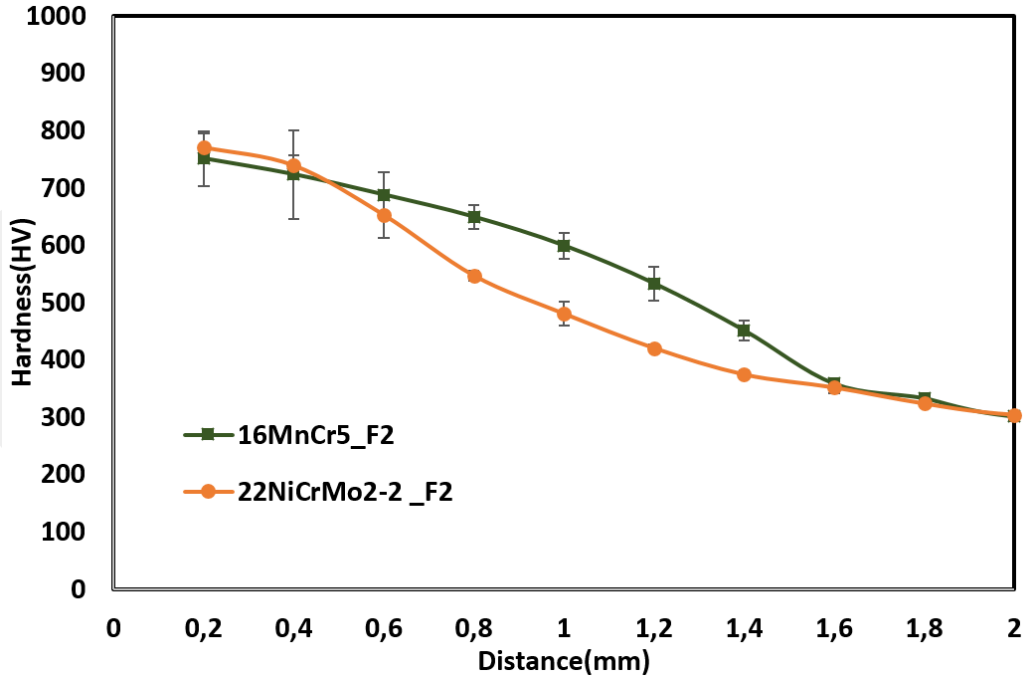

Figure 58. Hardness distributions of the DIN 22NiCrMo2-2 and DIN 16MnCr5 steels for the 5st test set

The growth kinetics of the austenite grain size with increasing temperature is explained in Chapter 4. In addition, increasing prior austenite grain size decreases the grain boundary area per unit volume. With increasing austenite grain size, the pearlite and ferrite nucleation site density decreases. Literature studies indicate that as the austenite grain size increases, the phase fraction of martensite and bainite increases while the ferrite phase fraction decreases [53], [72]. Thus, grain growth leads to increase hardness at higher temperature as shown in Figure 59 and Figure 60.

After examining the hardness results, the microstructures of the samples were examined. For the microstructure studies, the procedure for preparing the metallographic specimen as specified in Chapter 3 was exactly performed. Prepared specimens were examined under magnification from 50x to 500x under light field illumination with a Nikon Eclipse LV 150 optical microscope.

Figure 61 and Figure 62 represent the microstructures of the DIN 22NiCrMo2-2 and DIN 16MnCr5 steels of 1^{st} and 5^{th} test sets taken from the shell (hardened layer) and center regions for the stepped and stepless shaft. When the microstructures are examined after the carburizing heat treatment, it has been found that martensitic structure is located in the case zone while the bainitic structure is located in the center. The phase changes in the microstructure vary from martensite to bainite, depending on the amount of carbon and diffusion velocity decreasing from the surface to the center. This phase change in the microstructure matches the phases obtained as a result of the carburizing simulations which are explain in section 6.5 .

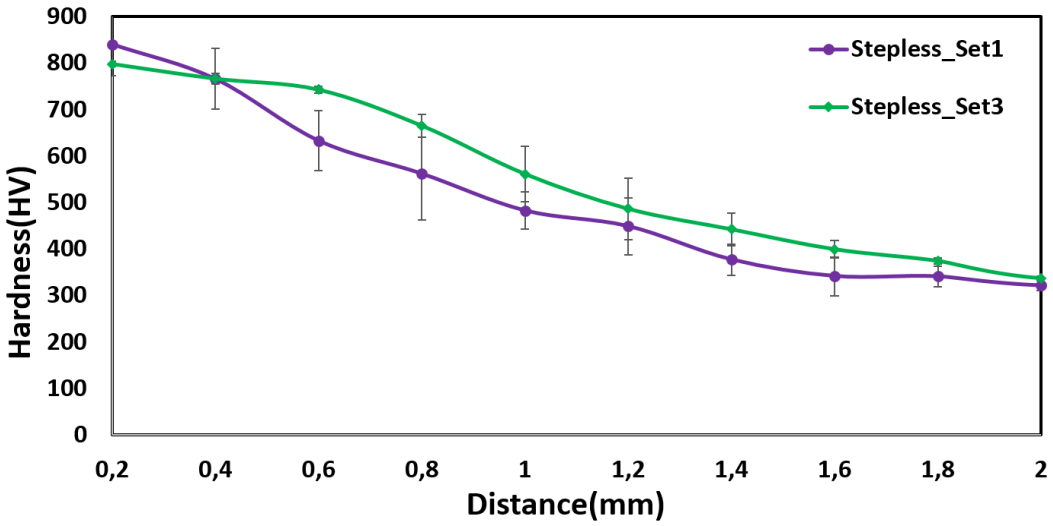

Figure 59.Comparison of hardness distributions of the 1st (T910_%C0.9_Toil60_F1) and 3st (T930_%C0.9_Toil70_F1) test sets for the DIN 22NiCrMo2-2

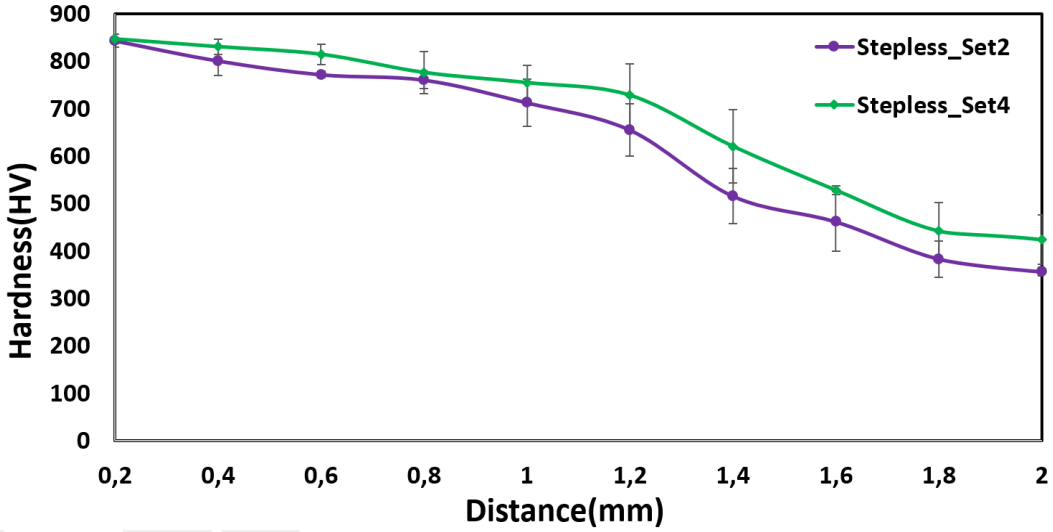

Figure 60. Comparison of hardness distributions of the 2nd (T910_%C1.1_Toil70_F1) and 4th (T930_%C1.1_Toil60_F1) test sets for the DIN 22NiCrMo2-2

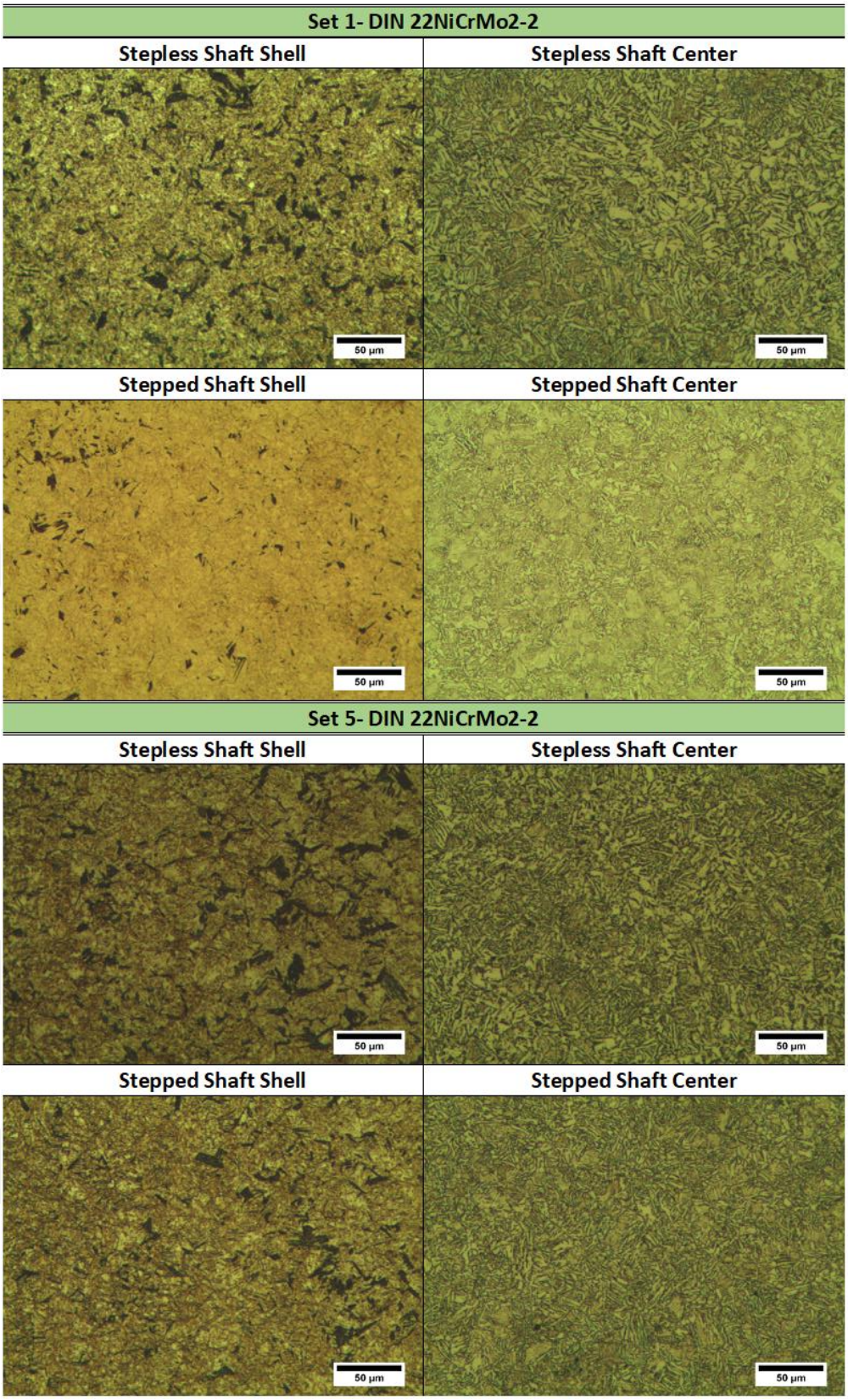

Figure 61. Optical micrographs of the 1st and 5th test sets of 22NiCrMo2-2 steel taken at 200x magnification, from shell and center regions for stepless and stepped shafts

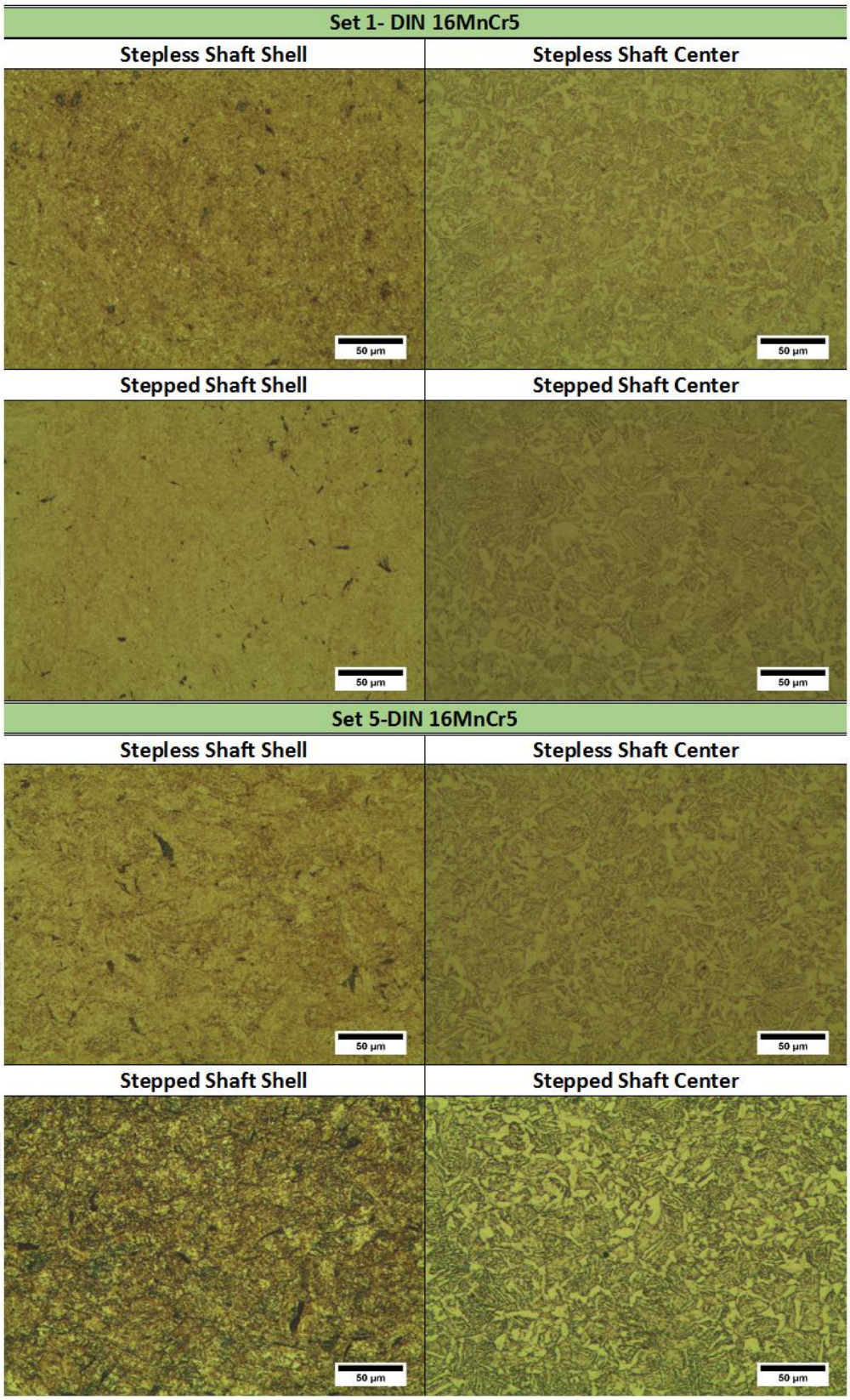

Figure 62. Optical micrographs of the 1st and 5th test sets of 16MnCr5 steel taken at 200x magnification, from shell and center regions for stepless and stepped shaft.

6.4. Case Depth Results

Microscopic visual procedure was used for determination of case depth of the samples [13], [73]. To determine the total case depth with this method, samples prepared for metallographic examination were used. The panoramic micrographs from the surface to the center of the samples were taken via an optical microscope. The total case depth was calculated on the panoramic micrographs using ImageJ®. The total case depth calculation example for the stepped shaft sample of DIN 16MnCr5 for the 2nd set experiment was represented in Figure 63.

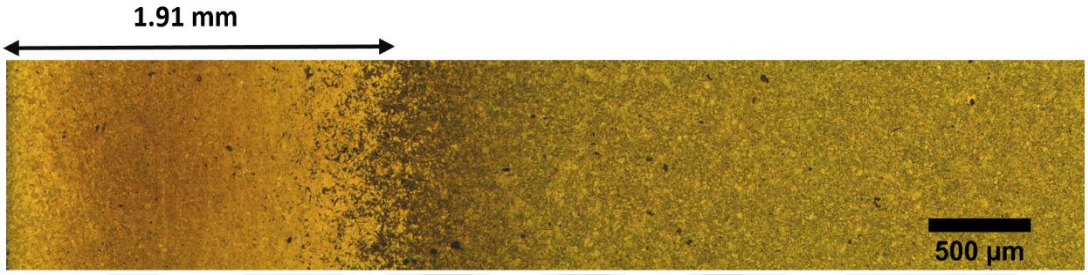

Figure 63. Calculation of total case depth using a panoramic micrograph

The calculated total case depths for all sets of stepless and stepped-Ø47.5 shaft steel for DIN 22NiCrMo2-2 and DIN 16MnCr5 materials were given in Figure 64. The highest case depth values in both materials were reached with experiments in the Furnace 1. The difference in the case depth results of the DIN 22NiCrMo2-2 and DIN 16MnCr5 materials was due to the difference between the chemical compositions of the materials given in Table 16.

When the case depth results were examined according to the Taguchi design, it was seen that the highest case depth is obtained in the 4th set test which is made in the furnace 1 with 1.1% carbon potential, the 930°C carburizing temperature, and the 60°C oil temperature. The carbon potential was determined as the most effective parameter according to case depth results. Also in the literature, the most effective parameter was determined as carbon potential as a result of the Taguchi design which is studied to find the important parameter affecting the case depth [74].

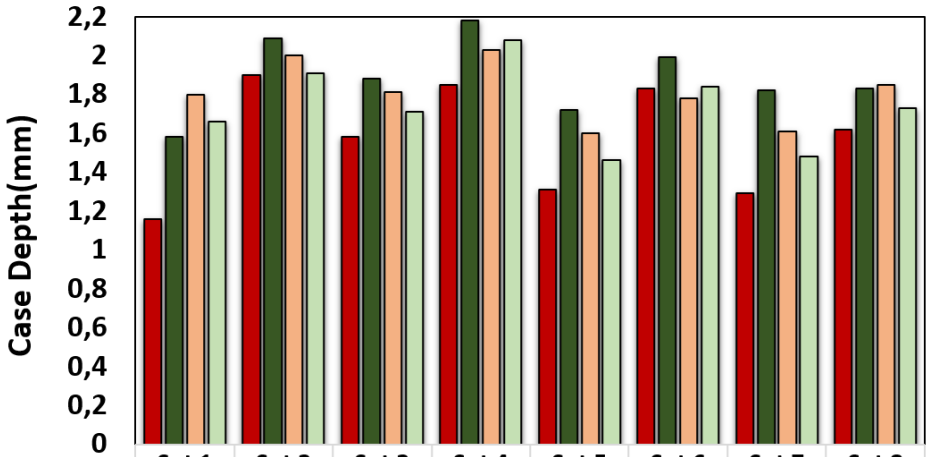

	Set 1	Set 2	Set 3	Set 4	Set 5	Set 6	Set 7	Set 8
22NiCrMo2-2_Stepless	1,16	1,9	1,58	1,85	1,31	1,83	1,29	1,62
22NiCrMo2-2_Stepped	1,58	2,09	1,88	2,18	1,72	1,99	1,82	1,83
16MnCr5_Stepless	1,8	2	1,81	2,03	1,6	1,78	1,61	1,85
16MnCr5_Stepped	1,66	1,91	1,71	2,08	1,46	1,84	1,48	1,73

Figure 64. Case Depth vs. Experimental Sets for Stepless and Stepped_Ø47.5 Shaft of DIN 22NiCrMo2-2 and DIN 16MnCr5 Steels

6.5. Comparison of Simulation and Experimental Results and Discussions

Simulation studies were carried out for the DIN 16MnCr5 material under the experimental conditions specified in Table 17 using the SYSWELD® heat treatment simulation software [6]. Also details of the simulation results can be found in B.Yazır Terzi's thesis study [6]. The carburizing heat treatment on the stepped and stepless shafts were simulated for the first 4 sets, since the furnace variation could not be added as an input parameter in the simulation studies. In Figure 65 and Figure 66, the hardness and phase fraction results of the simulations (4th set) were compared with the hardness results of the experiments (4th set and 8th set) for the stepped and stepless shaft. Figure 67 represents the comparison of the simulation studies with the experiments which were performed in the Furnace 1, whereas Figure 68 represents the comparison of experiments performed in the Furnace 2. The simulations were carried out for the first 4 sets, but the simulation set numbers in Figure 68 were given in accordance with the experiment set number for the ease of comparison.

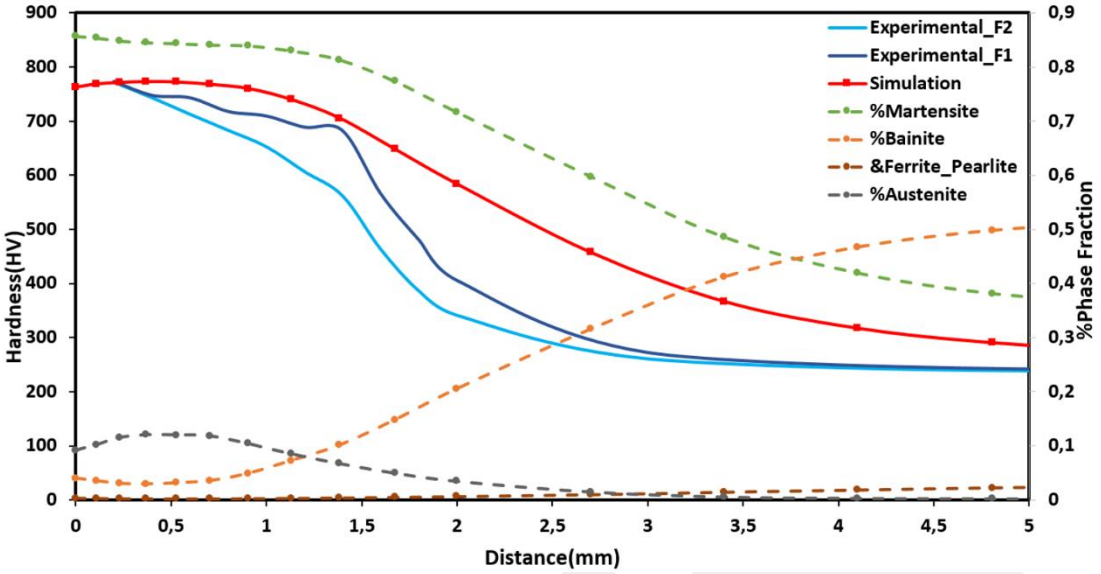

Figure 65. Comparison of hardness results of simulations and experiments on T930, % C1.1, Toil60, F1- F2 conditions for stepless shaft

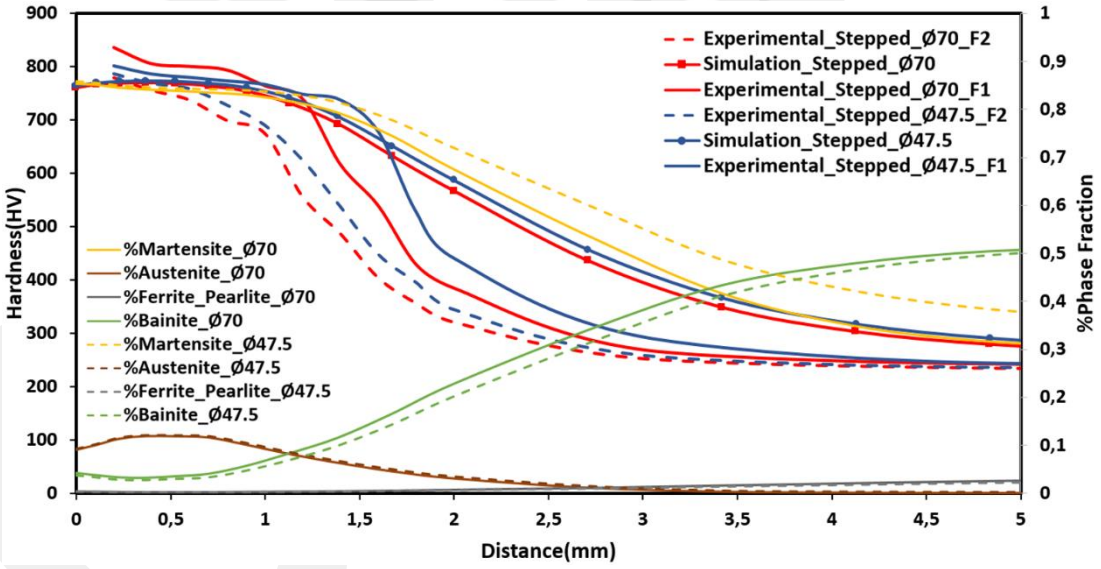

Figure 66. Comparison of hardness results of simulations and experiments on T930, % C1.1, Toil60, F1- F2 conditions for stepped shaft

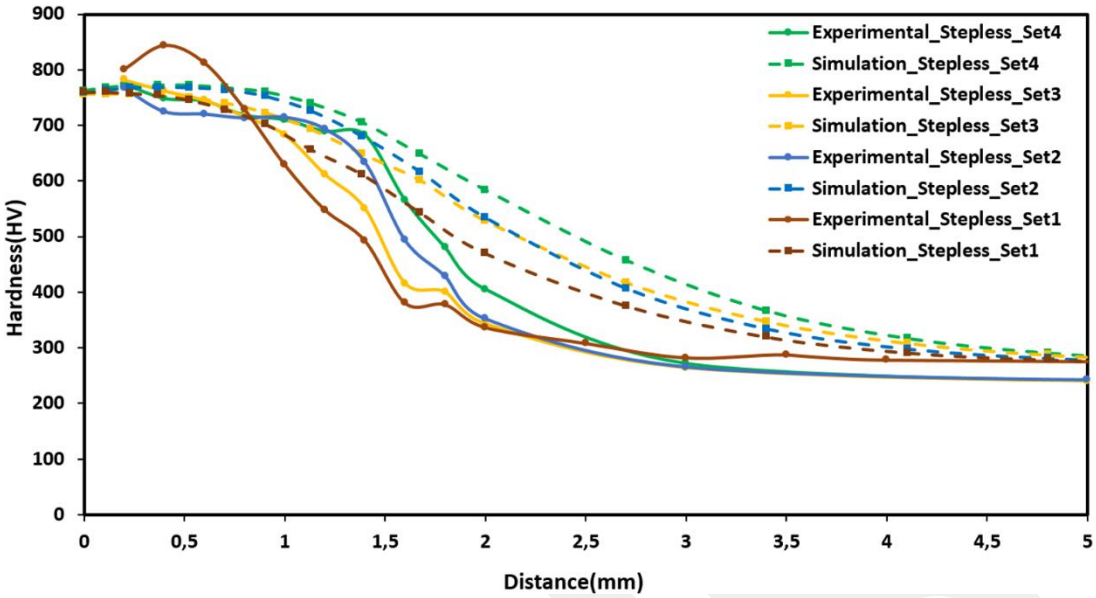

Figure 67. Comparison of experimental and simulation results in 1st, 2nd, 3rd and 4th test sets

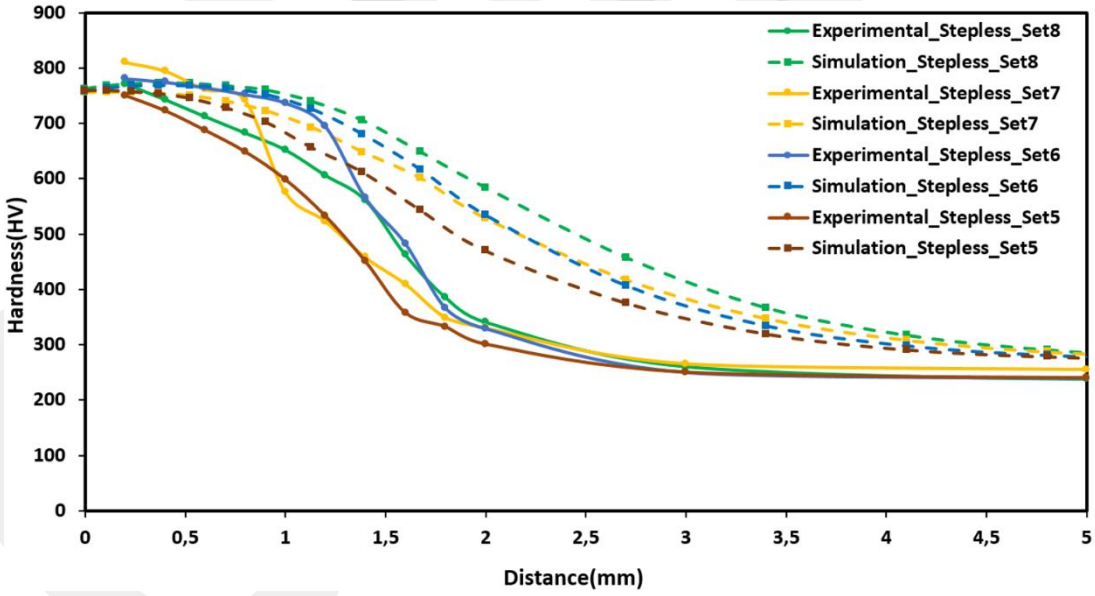

Figure 68. Comparison of experimental and simulation results in 5th, 6th, 7th and 8th test sets

The martensite phase fraction decrease from surface to the center depending on the decrease of cooling rate and the amount of carbon, as shown in Figure 65 and Figure 66. It appears that the fraction of bainite phase, which is less hard than martensite, begins to increase towards the center where the cooling rate is slower and the amount of carbon reduce. Since the martensite phase fraction at the surface is the highest, the surface hardness value is higher than the center. Resulting the martensite transformation, a body-centered-tetragonal (BCT) crystal structure is longer than one axis of the FCC. As the carbon amount increases, this dimensional difference increases, thereby hardness value of martensite phase increase [75].

The hardness distribution also varies depending on the diameter of the material. When the hardness distributions for the 47.5 and 70 diameters of the shafts in Figure 66 were examined, the higher hardness distribution was determined for Ø47.5 in both simulation and experimental results.

The highest hardness distributions were obtained both simulated and experimentally in the 4^{th} and 8^{th} set when all experimental and simulation sets were compared in Figure 67 and Figure 68. Also the lowest hardness distributions were obtained both simulated and experimentally in the 1^{st} and 5^{th} set. Considering the experimental conditions given in Table 17, for the 4^{th} and 8^{th} sets, it is seen that the carbon potential was 1.1% and the carburizing temperatures is 930°C. For the 1^{st} and 5^{th} sets, the carbon potential was 0.9% and the carburizing temperature is 910°C. The highest values of temperature and carbon potential cause the hardness distribution of 4^{th} and 8^{th} sets to be higher than other sets.

In Figure 67, internal oxidation may be the reason of the hardness result of 1^{st} set, where the highest hardness value slightly beyond the surface. Generally internal oxidation is to be expected during carburizing because all normal carburizing media used contain oxygen compounds (CO_2, CO, H_20 and so forth) and all commercial case-hardening steels contain alloying elements with a higher affinity for oxygen than iron (Si, Cr, Mn and so forth) [76].

It was seen that the simulation and experimental hardness curves generally match each other as shown in Figure 67 and Figure 68. It was also seen that for the stepped and stepless shaft, the hardness curve obtained in the Furnace 1 is more compatible with the simulation than the Furnace 2.

The difference between the simulation and the experimental results in Figure 67 and Figure 68 is in the 15-30% range also it was determined that this differences particularly begin with the below 1.3-1.5 mm depth of surface and increase of the bainitic volume fraction. In the literature, it was obtained that bainite formation during cooling is strongly dependent on the austenite grain size and alloying element [77].

The increase in the carbon diffusion coefficient depends on the amount of carbon in the environment, and the proportions of alloying elements. Also the alloying elements are important parameters affecting the hardness result. The addition of a small amount of alloying element which are stabilize the austenite phase, such as Ni and Si, considerably lower carbon transfer from the carburizing atmosphere and the rate of carburizing is slowing down. However, carbide-forming elements such as Cr, Mo significantly increases the mass transfer of carbon on the surface and thus the rate of carburizing increases [78], [79]. The Mo element is in the range of 0.15-0.25 in the simulation study, while it not exist in the chemical composition of the experimentally used DIN 16MnCr5 steel. At the same time, the amount of Cr element is more in the chemical composition used in simulations.

The direct effect of the mass transfer coefficient and diffusion coefficient on the carbon profile changes the hardness and case depth results. The fact that, the values of the mass transfer coefficient and diffusion coefficient in the simulation are different from the experimental value may be the other reason for the difference in simulation and experimental hardness results.

According to the results, it can be obtained that the compatibility of the simulation and experiment results changed depending on the chemical composition, mass transfer coefficient, diffusion coefficient, PAGS and bainitic transformation kinetics.

CHAPTER 7

CONCLUSION

In this study, firstly the material dataset for simulation of carburized quenching of DIN 22NiCrMo2-2 (SAE 8620H) steel has been obtained. This dataset includes chemical and microstructural characterization of the raw material, kinetics of austenite grain growth, critical temperatures and transformation kinetics in the form of TTT and CCT diagrams. The following conclusions can be drawn from those studies:

- ✓ The chemical and microstructural analysis indicate that the raw material is qualified for the process. The billets are free of macro-segregation, however exhibit banded and equiaxed ferrite-pearlite structure. The banded structure is due to micro-segregation of alloying elements, specifically Mn and Cr. The degree of banding have been evaluated in accordance with the ASTM E1268 [44], and the anisotropy index has been found to be between 1.14 – 1.24. The relative accuracy of the quantitative metallographic studies were below 10%, which indicates a rather homogenous distribution ferrite-pearlite microstructure along the billet.
- ✓ The phase diagram of DIN 22NiCrMo2-2 steel was determined by the CALPHAD method. From this diagram, 1.1 wt. % carbon concentration was determined to be the upper limit that could produce microstructures without the formation of undesired pro-eutectoid cementite.
- ✓ Austenite grain growth studies for the present steel indicate that it can be explained via ideal grain growth law. From those studies, the kinetic parameters Q and K_0 were calculated as 18.476 (J/mol) and 8.29×10^{-7} (mm^2/min) by taking the kinetic exponent, m, as 2. Those model parameters agree reasonably well with the literature. Slight differences with the literature

were found in the grain growth kinetics at temperatures lower than 900 ^{o}C; and were attributed to differences in composition, especially in fine carbide forming elements such as Mo. At higher temperatures, the influence of compositional differences are lower, since the alloy carbides would start to dissolve.

- ✓ Experimentally determined CCT and TTT diagrams agree well with the computationally determined ones. The difference between the diagrams depends on the variations from the used method to calculate the dilatometer curves and the PAGS. As the austenite grain size decreases, critical temperatures decrease and phase transformations occur in shorter times. Also it has been determined that the difference between the experimentally determined CCT and TTT diagrams from the literature is due to the difference in the alloying elements which are shifted the phase transformations for a longer period.

After obtaining the material data set, Design of Experiments (DoE) using the Taguchi method is conducted, both experimentally and computationally, on steel shafts made of DIN 22NiCrMo2-2 and DIN 16MnCr5 steels to minimize the variability of the industrial process. Those DoE studies were subject of 2 different thesis studies within the scope of larger project involving this study. The last part of this thesis presents microstructure and hardness distributions for the quality assessment of experimental studies and validation of computer simulations, both of which were conducted in the aforementioned complementary studies. For this part the following conclusions could be drawn:

- ✓ According to the results of the experimental carburizing tests with the Taguchi design for DIN 22NiCrMo2-2 and DIN 16MnCr5 steel, the surface-to-center hardness curves of these steels vary from each other. Those hardness differences were attributed to the chemical composition differences, which also causes differences in the hardenability.

- ✓ The case depths of the DIN 22NiCrMo2-2 and DIN 16MnCr5 steels vary depending on the austenitizing (carburizing) temperature and the amount of carbon dissolved in the austenite. As the austenitizing temperature increases the diffusion coefficient for carbon in austenite and the austenite grain size

increase, and therefore the hardenability increases. It has been determined that the present carburized quenching treatment produces the highest case depth in both steels for the following process conditions: 930 °C carburizing temperature, 1.1% carbon potential, 60 °C oil temperature. Moreover, the most effective parameter on case depth is determined as carbon potential, from the results of DoE.

- ✓ For the DIN 16MnCr5 steel, the hardness profiles obtained experimentally indicate the same trend with those obtained via computer simulations. The hardness at the surface and up to 1.5 mm depths agree very well, the differences are lower than 10%. The highest difference between the experimental and simulation results can be up to 30%. This highest disagreements correspond to the regions where bainite volume fraction is estimated to be higher than 15% and at depths 1.3 - 1.5 mm below the surface. Therefore, it can be concluded that the agreement between simulation and experimental results can be improved by determining bainite transformation kinetics more precisely, which may involve including its dependence on stress, local differences in austenite grain size and chemical composition.

As a future work, the grain growth kinetics model can be improved by determining PAGS in experiments which are conducted at different austenitizing temperatures. Thus, the CCT and TTT diagrams determined by experimental and computational methods can be made more consistent. DIN 22NiCrMo2-2 material data can be added into the simulation material library according to these improvements. Also the simulation and experimental results for DIN 16MnCr5 steel can be made further compatible by changing the chemical composition, mass transfer coefficient, PAGS and bainitic transformation kinetics which are input parameters in the simulation program.

REFERENCES

[1] C. A. Apple and G. Krauss, “Microcracking and Fatigue in a Carburized Steel,” *Metall. Trans.*, vol. 4, no. May, pp. 1195–1200, 1973.

[2] M. A. Majid, “The effect of thermochemical treatment on the fatigue properties of alloy steels,” Aston University, 1980.

[3] K. Genel and M. Demirkol, “Effect of case depth on fatigue performance of AISI 8620 carburized steel,” *Int. J. Fatigue*, vol. 21, no. 2, pp. 207–212, 1999.

[4] T. Domanski and A. Bokota, “Numerical Models of Hardening Phenomena of Tools Steel Base On The TTT And CCT Diagrams,” *Archihives Metall. Mater.*, vol. 56, no. 2, 2011.

[5] H. Yılmaz, “Investigation of Carburized Quenching Process of Shafts Using Design of Experiments,” Atılım University, 2017.

[6] B. Yazır, Terzi, “Investigation of Carburized Quenching Process of Shafts Using Computer Simulations,” Atılım University, 2017.

[7] C. Şimşir, “Modeling and Simulation of Steel Heat Treatment—Prediction of Microstructure, Distortion, Residual Stresses, and Cracking,” in *Steel Heat Treating Technologies*, vol. 4B, ASM International, Materials Park, OH, pp. 409–458.

[8] M. Tarakci, K. Korkmaz, Y. Gencer, and M. Usta, “Plasma electrolytic surface carburizing and hardening of pure iron,” *ScienceDirect*, vol. 199, no. 2–3, pp. 205–212, 2005.

[9] E. Boyle, “Microstructural Effects on the Mechanical Properties of Carburized Low-Alloy Steels,” Windsor University, 2007.

[10] G. Krauss, *Steels: Processing, Structure, and Performance*. ASM International, Materials Park, OH.

[11] C. Zhang, “Assessment of depth of case-hardening in steel rods by electromagnetic methods,” Iowa State University, 2009.

[12] R. Winston Lehr, “Carbon diffusion in low carbon steel at sub-critical temperatures,” Southern California University, 1961.

[13] ASM International, *ASM Metals Handbook Volume 4: Heat Treating*. 1991.

[14] J. L. Dossett and H. E. Boyer, *Practical Heat Treating*. ASM International, Materials Park, OH, 2006.

[15] K.-E. Thelning, *Steel and its Heat Treatment, Bofors Handbook*. 1967.

[16] A. Ç. Can, A. R. Tarakcılar, and Y. Özmen, “Decreasing Heat Treatment Cost Of Surface Hardened Machine Parts By Case Carburization,” *Pamukkala Univ. J. Eng. Sci.*, pp. 429–433, 1997.

[17] W. F. Smith, *Structure and properties of engineering alloys*. 1993.

[18] J. R. Davis, *Surface Hardening of Steels*. 2002.

[19] W. Callister and D. Rethwisch, *Materials science and engineering: an introduction*, vol. 94. 2007.

[20] J. Moon, J. Lee, and C. Lee, “Prediction for the austenite grain size in the presence of growing particles in the weld HAZ of Ti-microalloyed steel,” *Mater. Sci. Eng. A*, vol. 459, no. 1–2, pp. 40–46, 2007.

[21] A. H. Seikh, M. S. Soliman, A. AlMajid, K. Alhajeri, and W. Alshalfan, “Austenite Grain Growth Kinetics in API X65 and X70 Line-Pipe Steels during Isothermal Heating,” *Adv. Mater. Sci. Eng.*, vol. 2014, pp. 1–8, 2014.

[22] P. A. Manohar, D. P. Dunne, T. Chandra, and C. R. Killmore, “Grain Growth Predictions in Microalloyed Steels.,” *ISIJ Int.*, vol. 36, no. 2, pp. 194–200, 1996.

[23] E. Khzouz, “Grain Growth Kinetics in Steels,” Worcester Polytechnic Institute, 2011.

[24] N. S. L. Phillips, “Phase transformations in cast superaustenitic stainless steels,” Iowa State University, 2006.

[25] Y. Kim, “Phase transformations in cast duplex stainless steels,” Iowa State University, 2004.

[26] D. Askeland, P. Fulay, and W. Wright, *The Science and engineering of materials*. 2010.

[27] P. Cavaliere, G. Zavarise, and M. Perillo, “Modeling of the carburizing and nitriding processes,” *Comput. Mater. Sci.*, vol. 46, no. 1, pp. 26–35, 2009.

[28] S. Kang and Y. Im, “Finite element investigation of multi-phase transformation within carburized carbon steel,” *ScienceDirect*, vol. 183, no. 2–3, pp. 241–248, 2007.

[29] M. Tehler, “Modeling Phase Transformations and Volume Changes during Cooling of Case Hardening Steels,” KTH Royal Institute of Technology, 2009.

[30] A. Clark, “Comparison of Austempering and Quench-and-Tempering Processes for Carburized Automotive Steels,” Windsor University, 2013.

[31] G. F. Vander Voort, *Atlas of Time-Temperature Diagrams for Irons and Steels*. ASM International, Materials Park, OH, 1991.

[32] R. Meyendorf, “Nondestructive Determination Of Case Depth In Surface Hardened Steels By Combination Of Electomagnetic Test Methods,” Dayton University, 2011.

[33] H. Bhadeshia and R. Honeycombe, *Steels: Microstructure and Properties*. 2006.

[34] Y. H. Lee, “Hardenability of ductile cast iron,” University of Kansas, 1988.

[35] ASTM E340-15, “Standard Practice for Macroetching Metals and Alloys,” in *ASTM International*, 2015, pp. 1–11.

[36] ASTM E3-11, “Standard Guide for Preparation of Metallographic Specimens,” in *ASTM International*, .

[37] ASTM E1122 - 96, “Standard Practice for Obtaining JK Inclusion Ratings Using Automatic Image Analysis,” in *ASTM International*, .

[38] S. Cai, “Microstructural Banding in Hot Rolled Microalloyed Low Carbon Steels,” Quenn’s University, 2004.

[39] M. D. Abramoff, P. J. Magalhaes, and S. J. Ram, “Image Processing with

ImageJ," *Biophotonics Int.*, vol. 11, no. 7, pp. 36–42, 2004.

[40] C. Grove and D. A. Jerram, "An ImageJ macro to quantify total optical porosity from blue-stained thin sections," *Comput. Geosci.*, vol. 37, no. 11, pp. 1850–1859, 2011.

[41] D. Sage, "Graylevel Watershed," *Biomedical Imaging Group*, 2011. [Online]. Available: http://bigwww.epfl.ch/sage/soft/watershed/. [Accessed: 27-May-2017].

[42] ASTM E112-13, "Standard Test Methods for Determining Average Grain Size," in *ASTM International*, 2014, pp. 1–28.

[43] J. D. Verhoeven, "A Review of Microsegregation Induced Banding Phenoomena in Steels," *J. Mater. Eng. Perform.*, vol. 9, no. 3, pp. 286–296, 2000.

[44] ASTM E1268, "Standard Practice for Assessing the Degree of Banding or Orientation of Microstructures," in *ASTM International*, vol. 01, no. July 1999, 2013, pp. 1–29.

[45] E. A. Jägle, "Modelling of Microstructural Banding during Transformations in Steel," Cambridge University, 2007.

[46] W. Bleck, *Materials science of Steel*. Institut fuer Eisenhüttenkunde, RWTH Aachen University, 2007.

[47] F. C Campbell, *Phase Diagrams*. ASM International, Materials Park, OH.

[48] E. J. Pickering and H. K. D. H. Bhadeshia, "The Consequences of Macroscopic Segregation on the Transformation Behaviour of a Pressure-Vessel Steel," *Press. Vessel Technol.*, vol. 136, 2014.

[49] M. Hunkel, E. Hoffmann, and H. Zoch, "Distortion of components due to segregations of a low alloy SAE 5120 steel after blank and case hardening," HTM - Harterei-Technische Mitteilungen, 2007.

[50] S. H. M. Azghandi, V. G. Ahmadabadi, A. Zabett, and F. Fazeli, "Modelling of austenite grain growth kinetics in a microalloyed steel (30MSV6) in the presence of carbonitride precipitates," *Philos. Mag.*, vol. 94, no. 24, pp. 2758–

2775, 2014.

[51] K. A. Alogab, D. K. Matlock, J. G. Speer, and H. J. Kleebe, “The Influence of Niobium Microalloying on Austenite Grain Coarsening Behavior of Ti-modified SAE 8620 Steel,” *ISIJ Int.*, vol. 47, no. 2, pp. 307–316, 2007.

[52] J. L. Pacheco and G. Krauss, “Microstructure and High Bending Fatigue Strength in Carburized Steel,” *J. Heat Treat.*, vol. 7, no. 2, pp. 77–86, 1989.

[53] H. Roelofs, S. Hasler, L. Chabbi, U. Urlau, J. Chen, and H. K. D. H. Bhadeshia, “Multiphase Structures in Case Hardening Steels following Continuous Cooling,” *Mater. Sci. Metall.*, 2008.

[54] E. R. Weibel and R. P. Bolender, “Stereological Techniques for Electron Microscopic Morphometry.pdf,” *Princ. Tech. Electron Microsc.*, vol. 3, 1973.

[55] G. F. Vander Voort, *Metallography Principles And Practice*. ASM International, Materials Park, OH.

[56] E. E. Underwood and E. A. Starke, “Quantitative Stereological Methods for Analyzing Important Microstructural Features in Fatigue of Metals and Alloys,” *Am. Soc. Test. Mater.,* pp. 633–682, 1979.

[57] P. R. Krahe, “Revealing the former austenite grain boundaries of high- purity iron-carbon alloys,” *ScienceDirect*, vol. 4, no. 2, pp. 171–175, 1971.

[58] C. Yue, L. Zhang, S. Liao, and H. Gao, “Kinetic analysis of the austenite grain growth in GCr15 steel,” *J. Mater. Eng. Perform.*, vol. 19, no. 1, pp. 112–115, 2010.

[59] S. Gu, “Cyclic Thermal Treatment,” Illinois Institute of Technology, 2015.

[60] M. . Islam and M. M. a. Bepari, “Effects of niobium additions on the structure, depth, and austenite grain size of the case of carburized 0.07% C steels,” *J. Mater. Eng. Perform.*, vol. 5, no. 5, pp. 593–597, 1996.

[61] H.-S. Yang and H. K. D. H. Bhadeshia, “Uncertainties in dilatometric determination of martensite start temperature,” *Mater. Sci. Technol.*, vol. 23, no. 5, pp. 556–560, 2007.

[62] O. Müştak, “Characterization Of SAE 52100 Bearing Steel For Finite Element Simulation Of Through-Hardening Process,” Middle East University, 2014.

[63] B. Pawlowski, P. Bala, and R. Dziurka, “Improper Interpretation Of Dilatometric Data For Cooling Transformation In Steels,” *Arch. Mater. Sci. Eng.*, vol. 59, no. 3, pp. 14–16, 2014.

[64] S. Marie, R. Ducloux, P. Lasne, J. Barlier, and L. Fourment, “Inverse Analysis of Forming Processes based on FORGE ® environment,” *Key Eng. Mater.*, vol. 611–612, pp. 1494–1502, 2014.

[65] A. Farrar, R, Z. Zhang, R. Bannister, S, and S. Barritte, G, “The effect of prior austenite grain size on the transformation behaviour of C-Mn-Ni weld metal,” *Mater. Sci.*, vol. 28, no. 5, pp. 1385–1390, 1993.

[66] G. Krauss and I. Introduction, “Solidification , Segregation , and Banding in Carbon and Alloy Steels,” *Metall. Mater. Trans. B*, vol. 34, no. December, pp. 781–792, 2003.

[67] S. Chupatanakul, “Kinetics of Bainite Transformation in Carburized 4317 M2,” Illinois Institute of Technology, 2006.

[68] D. Mukerjee, S. R.Mediratta, and V. Ramanswamy, “Dilatometric Study on Some Medium Carbon Constructional Steels,” *Trans. Japan Inst. Met.*, vol. 27, pp. 108–114, 1986.

[69] S. Lee and Y. Lee, “Effect of Austenite Grain Size on Martensitic Transformation of a Low Alloy Steel,” *Mater. Sci.*, vol. 479, pp. 3169–3172, 2005.

[70] Y. Zhang, “Microstructure and Modeling of Bainite Transformation in Deformed Austenite,” Queen’s University, 2004.

[71] A. Garcia-junceda, C. Capdevila, F. G. Caballero, and C. Garcia de Andres, “Dependence of Martensite Start Temperature On Fine Austtenite Grain Size,” *Sci. Direct*, vol. 58, no. 2, pp. 134–137, 2015.

[72] M. Peterli, M. Truong, N. Manopulo, and P. Hora, “A new optimization procedure for the accurate characterization of thermal phase transformation

curves based on controlled quenching experiments," *MATEC Web Conf.*, vol. 80, 2016.

[73] M. P. Products, "ASTM B931-14, Standard Test Method for Metallographically Estimating the Observed Case Depth of Ferrous Powder Metallurgy (P/M) Parts 1." ASM International, West Conshohocken, PA, 2014.

[74] K. Palaniradja, N. Alagumurthi, and V. Soundararajan, "Optimization of Process Variables in Gas Carburizing Process : A Taguchi Study with Experimental Investigation on SAE 8620 and AISI 3310 Steels," *Eng. Environ. Sci.*, vol. 29, no. 5, pp. 279–284, 2005.

[75] D. J. Medlin, "Metallurgical Phase Transformations in the Case Layer of a Carburized Bearing Steel Due to Rolling Contact," Nebraska University, 1993.

[76] J.-I. Hwang, "A Thermodynamic Study on Carburizing of Plain Carbon and Alloy Steels," Marquette University, 1986.

[77] S. M. C. Van Bohemen and J. Sietsma, "The kinetics of bainite and martensite formation in steels during cooling," *Mater. Sci. Eng. A*, vol. 527, no. 24–25, pp. 6672–6676, 2010.

[78] L. B. Cerully, "The Fabrication Of Thin-Walled Steel Alloys Through The Gas Carburization Of Reduced Metal Oxide Extrusions," Georgia Institute of Technology, 2010.

[79] A. A. Sorour, "High Temperature Corrosion Of Heat Resistant Nickel-Based Alloys In Carburizing Environments," King Fahd University of Petroleum and Minerals (KFUPM), 2007.

APPENDICES

A. Raw Material Characterization Results

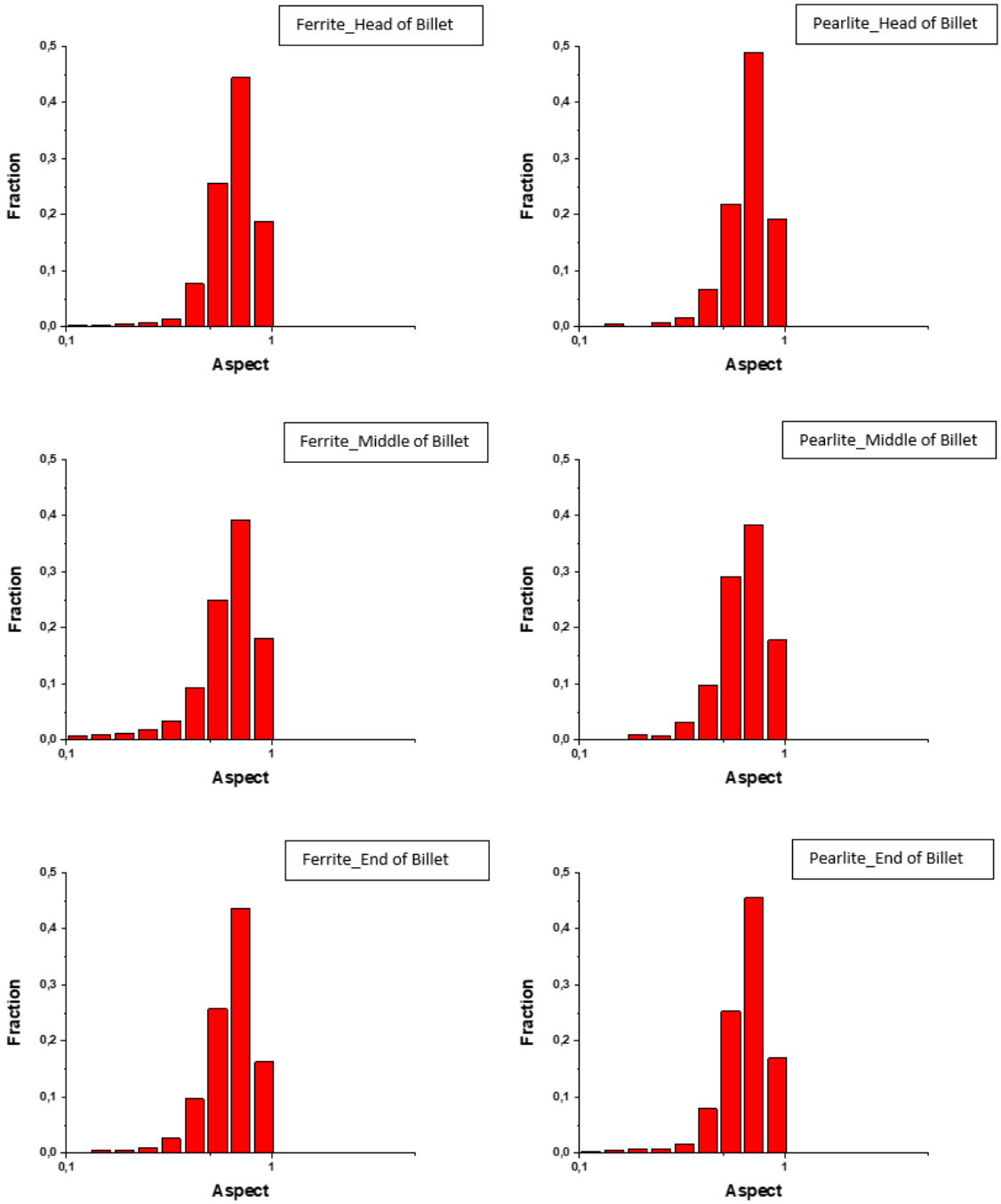

Figure A. 1. Ferrite and pearlite aspect ratio distributions of section 1 for the head, middle, end of the billet

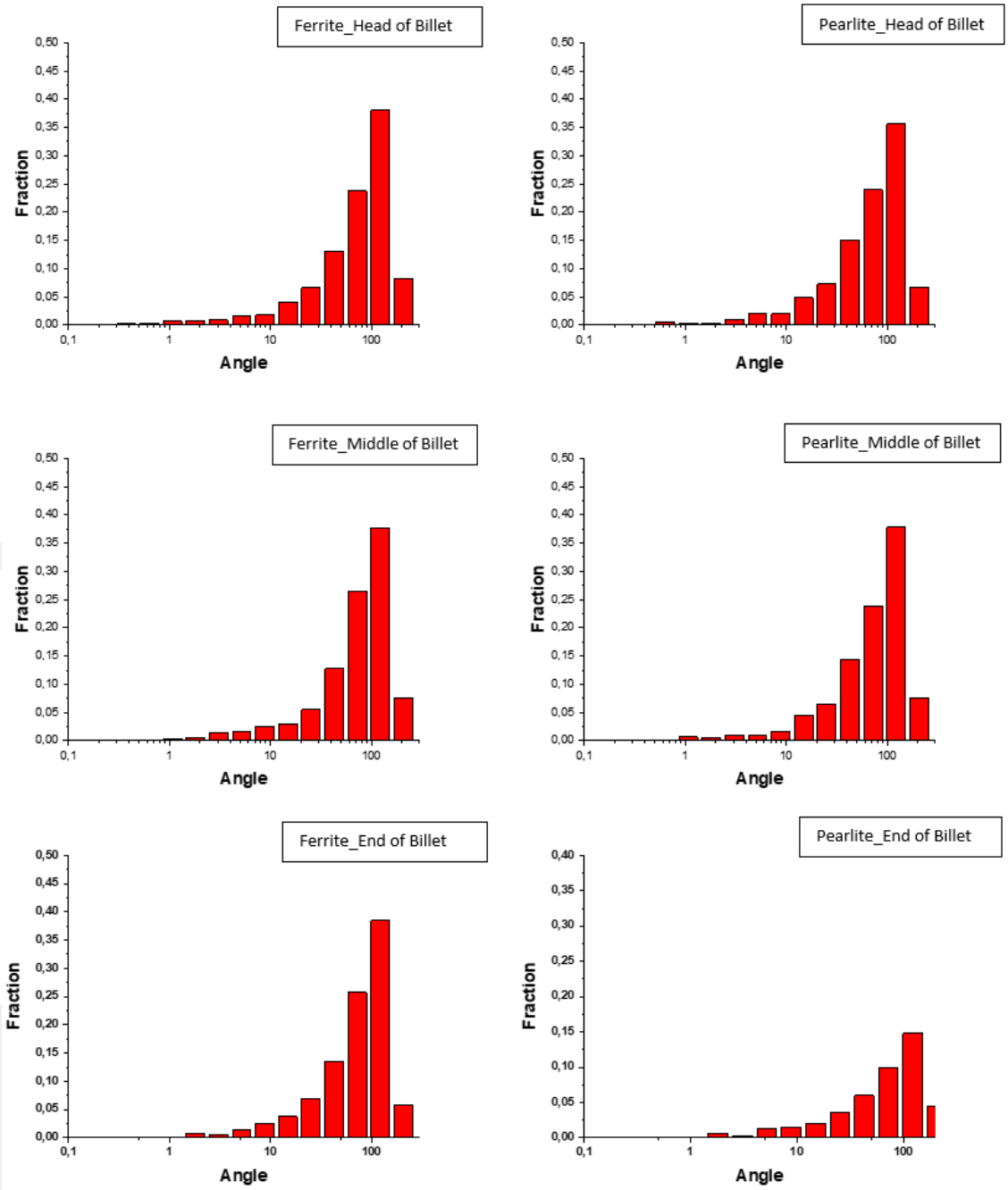

Figure A. 2. Ferrite and pearlite angle distributions of section 1 for the head, middle, end of the billet

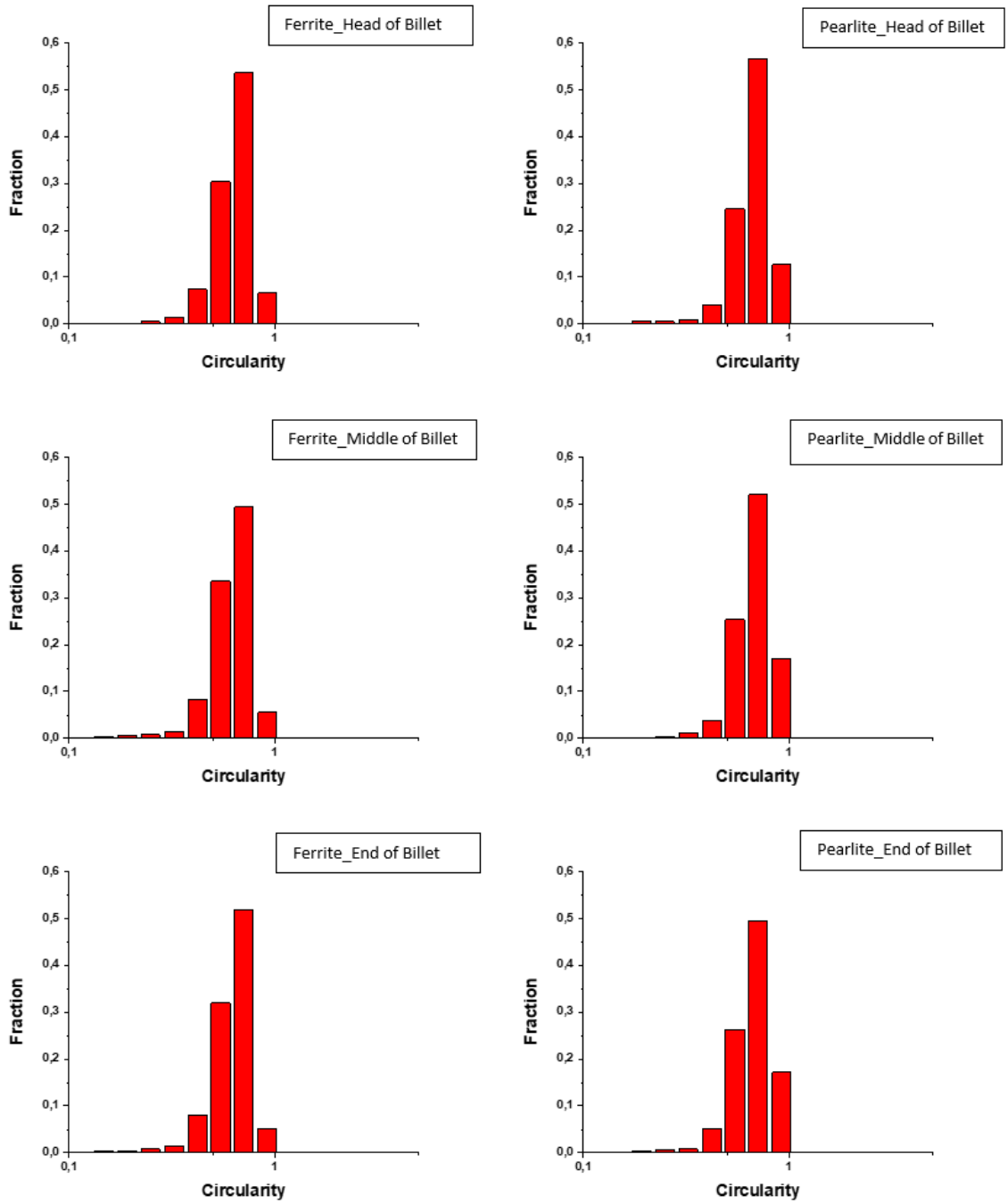

Figure A. 3. Ferrite and pearlite circularity distributions of section 1 for the head, middle, end of the billet

B. Microstructure Results of Carburized Shafts

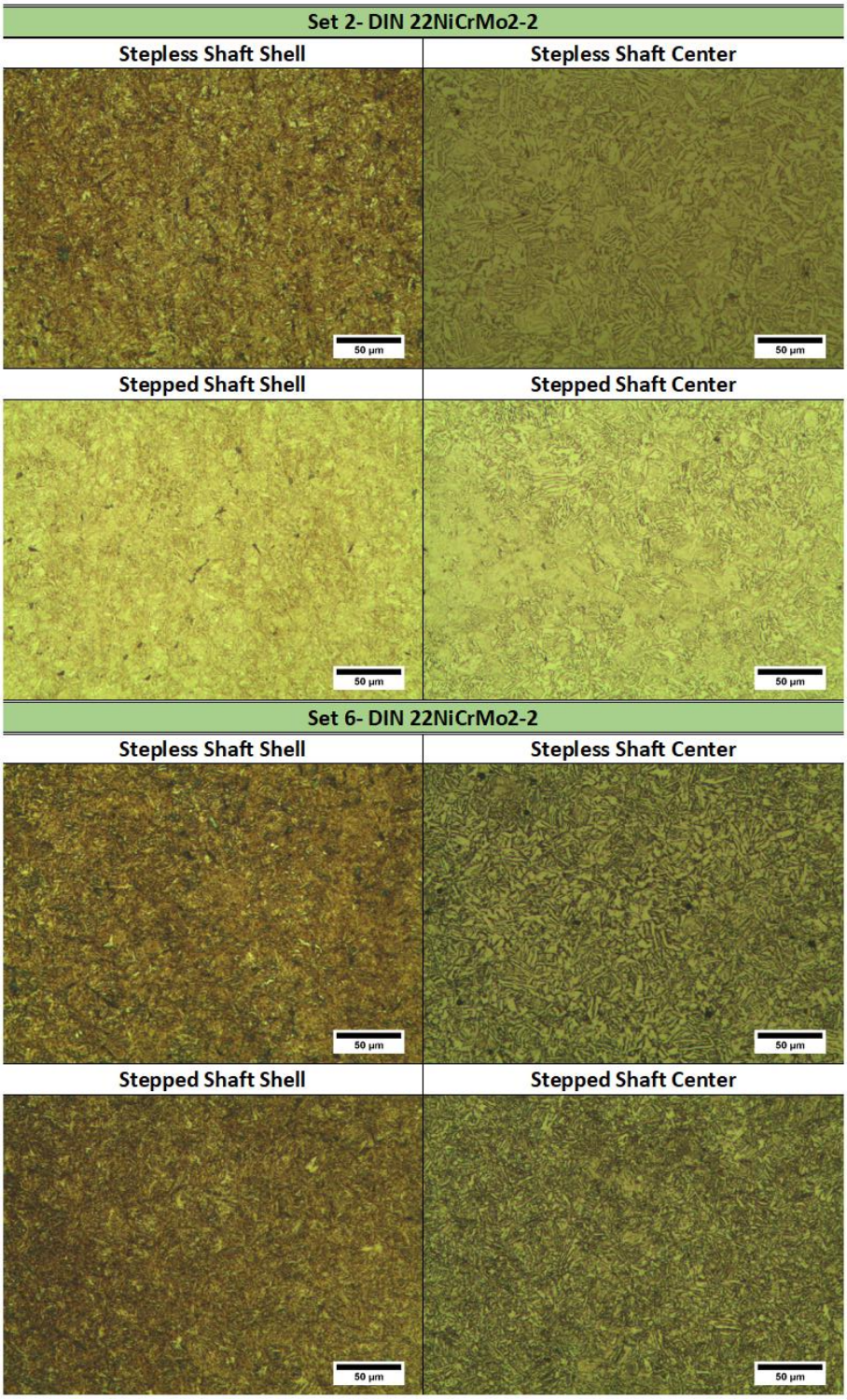

Figure A. 4. Optical micrographs of the 2nd and 6th test sets of 22NiCrMo2-2 steel taken at 200x magnification, from shell and center regions for stepless and stepped shaft.

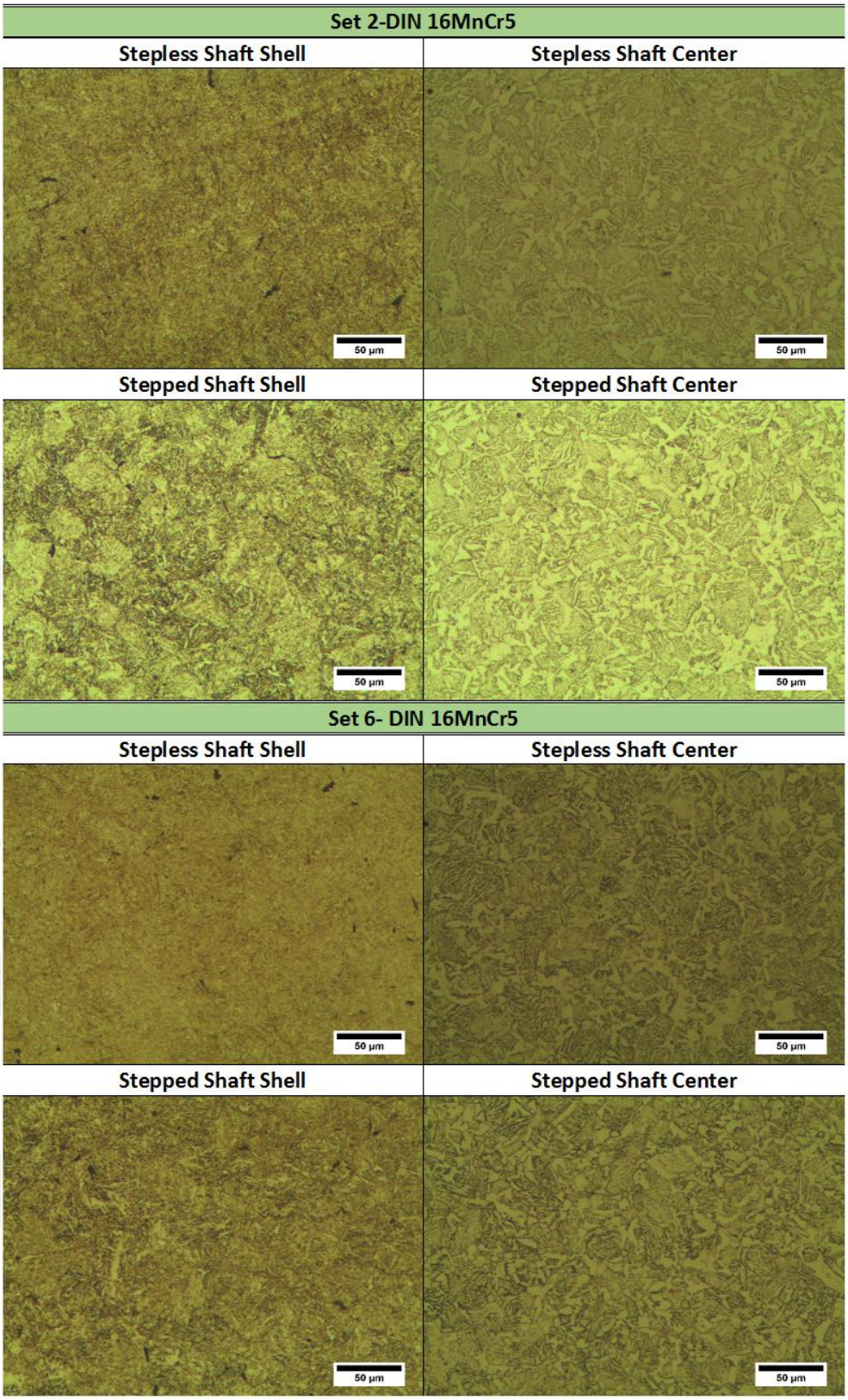

Figure A. 5. Optical micrographs of the 2nd and 6th test sets of 16MnCr5 steel taken at 200x magnification, from shell and center regions for stepless and stepped shaft.

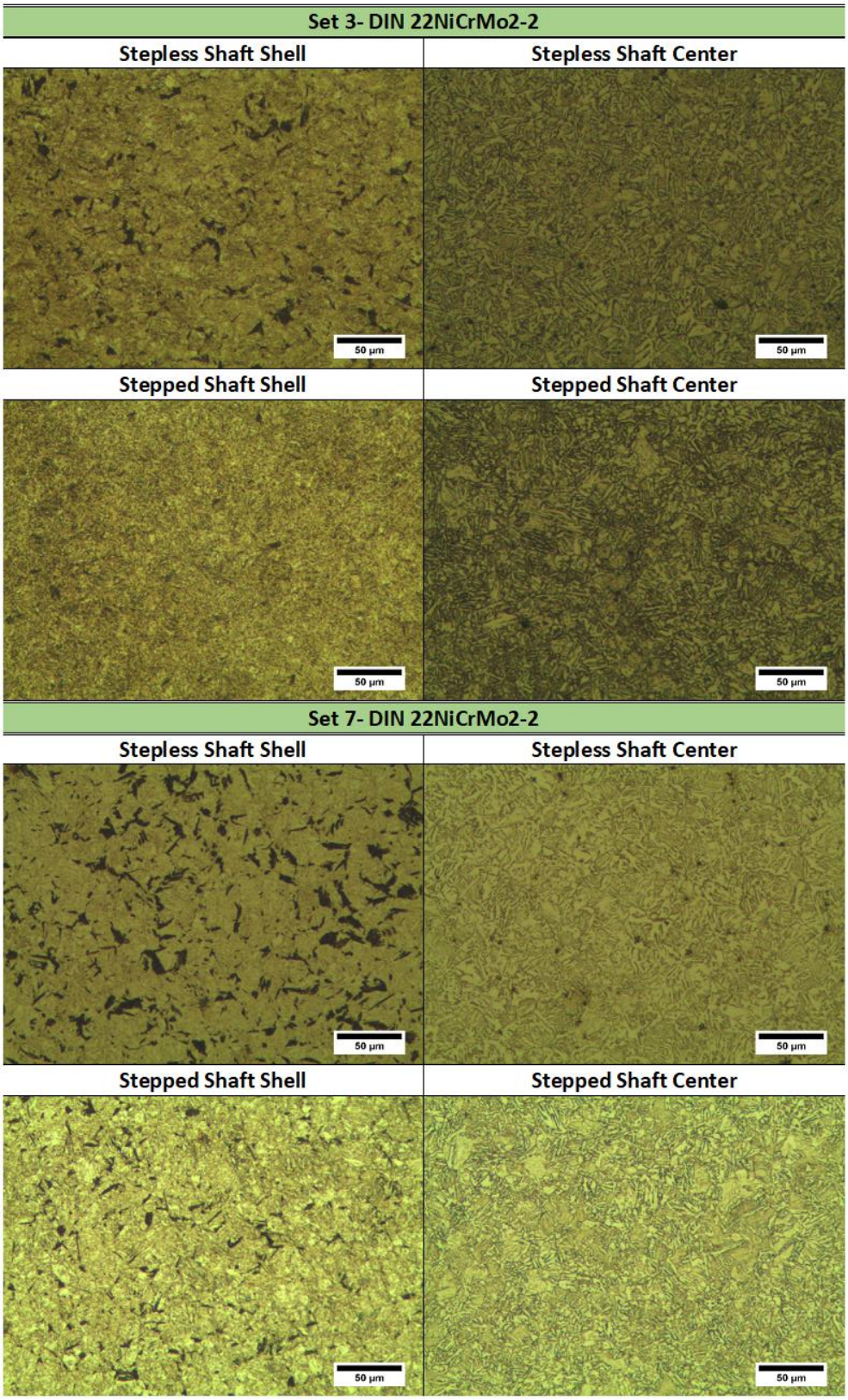

Figure A. 6. Optical micrographs of the 3rd and 7th test sets of 22NiCrMo2-2 steel taken at 200x magnification, from shell and center regions for stepless and stepped shaft.

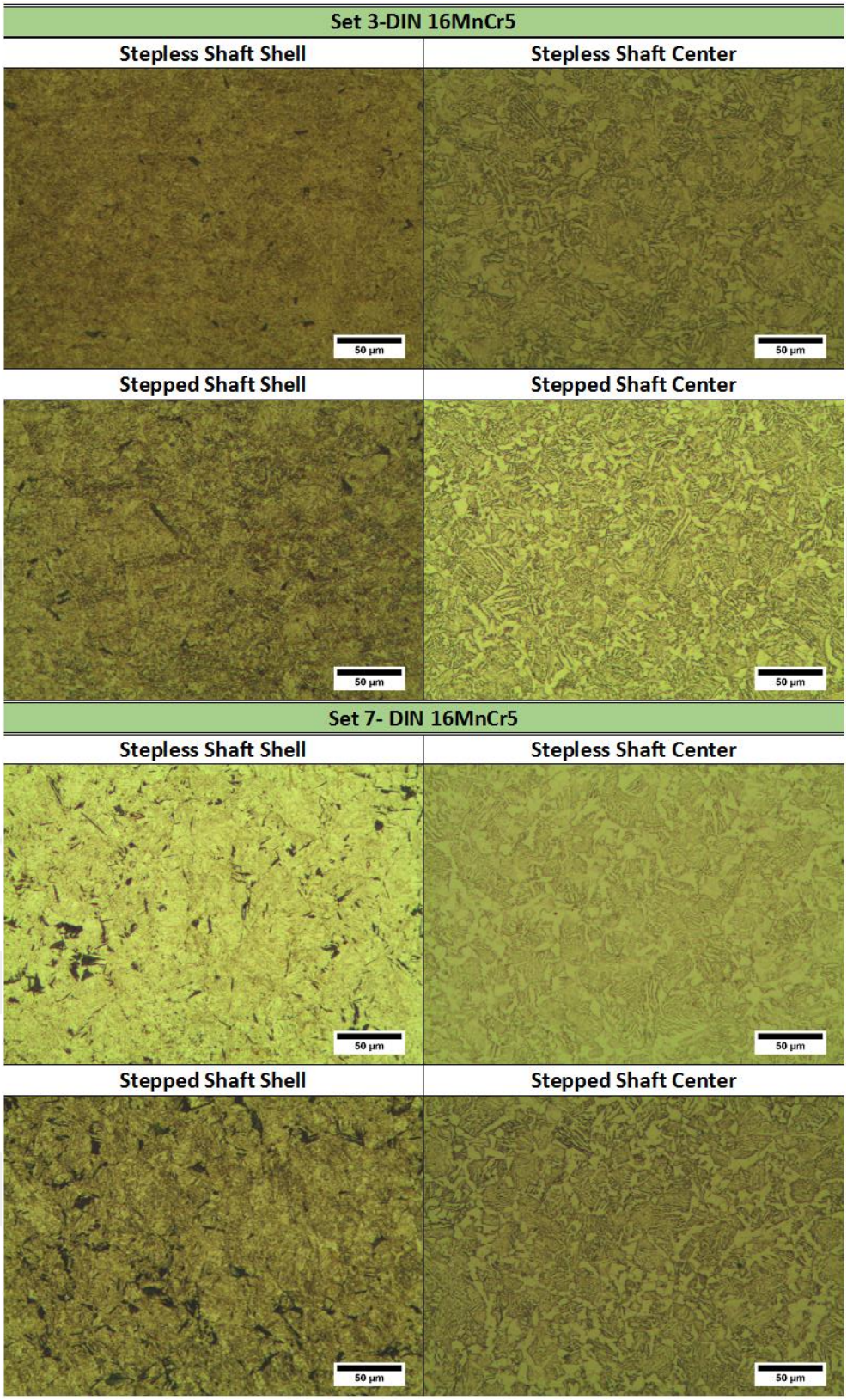

Figure A. 7. Optical micrographs of the 3rd and 7th test sets of 16MnCr5 steel taken at 200x magnification, from shell and center regions for stepless and stepped shaft

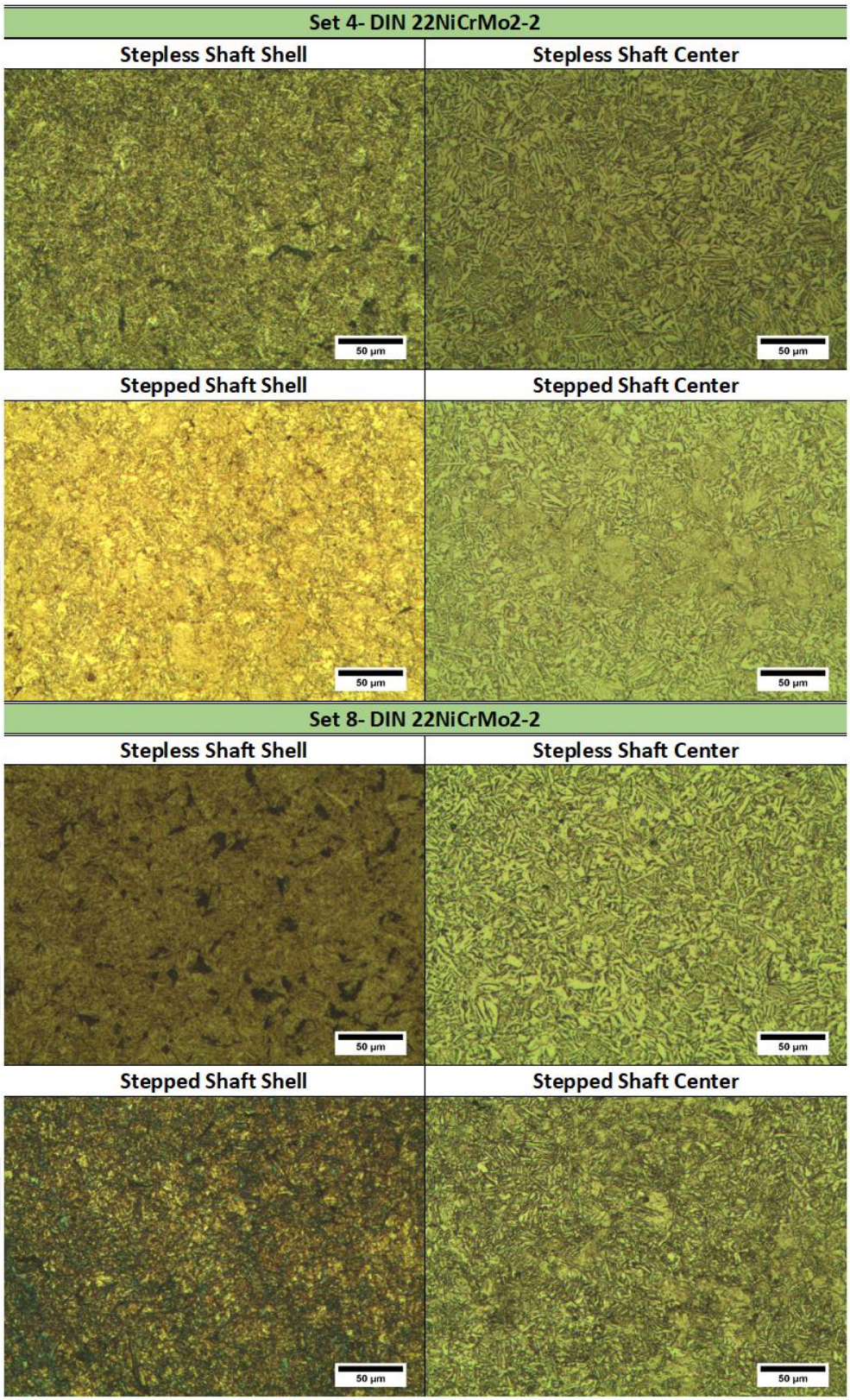

Figure A. 8. Optical micrographs of the 4th and 8th test sets of 22NiCrMo2-2 steel taken at 200x magnification, from shell and center regions for stepless and stepped shaft.

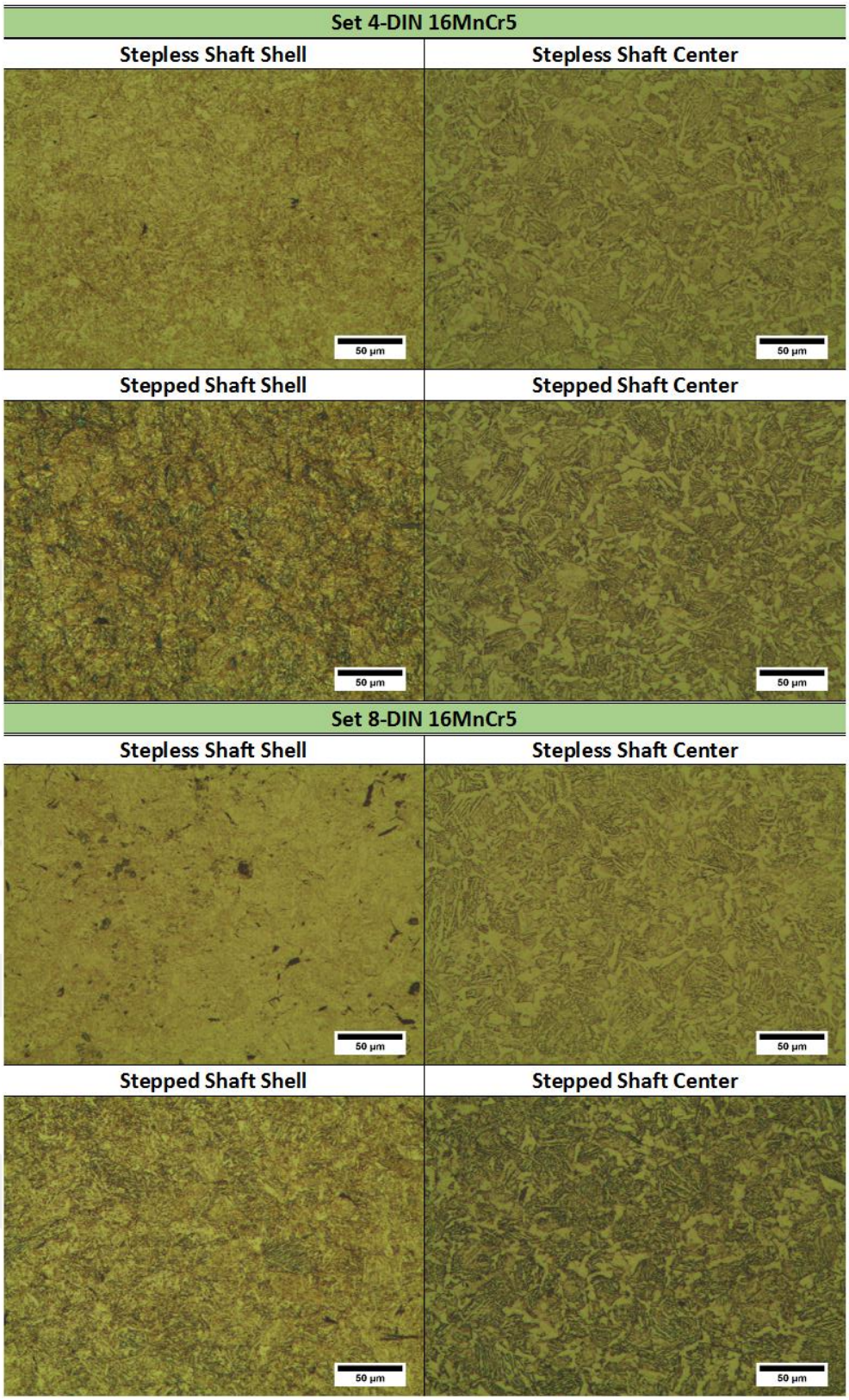

Figure A. 9. Optical micrographs of the 4th and 8th test sets of 16MnCr5 steel taken at 200x magnification from, shell and center regions for stepless and stepped shaft.